Investigation of H atom and free radical behavior in gas hydrates

by

Mina Mozafari

M.Sc., Shahid Beheshti University, 2008
B.Sc., Azad University, North Tehran Branch, 2004

Thesis Submitted in Partial Fulfillment of the
Requirements for the Degree of
Doctor of Philosophy

in the
Department of Chemistry
Faculty of Science

SIMON FRASER UNIVERSITY

Fall 2017

Approval

Name: **Mina Mozafari**

Degree: **Doctor of Philosophy (Chemistry)**

Title: ***Investigation of H atom and free radical behavior in gas hydrates***

Chair: Bingyun Sun
Associate Professor

Examining Committee:

Dr. Paul W. Percival
Senior Supervisor
Professor

Dr. Michael H. Eikerling
Supervisor
Professor

Dr. Khashayar Ghandi
Supervisor
Associate Professor
Department of Chemistry & Biochemistry
Mount Allison University

Dr. Loren Kaake
Internal Examiner
Assistant Professor

Dr. Roderick E. Wasylishen
External Examiner
Professor Emeritus
Department of Chemistry
University of Alberta

Date Defended/Approved: December 15, 2017

Abstract

Gas hydrates (or clathrate hydrates) are solid crystalline materials composed of a framework of hydrogen-bonded water molecules arranged to form cages which can contain small guest molecules. They have been a subject of research in the oil and gas industry, for carbon dioxide sequestration, gas storage and separation. In order to better understand the applications of hydrates, there is a need to study them at the molecular scale, but there has been relatively little investigation of chemical reactions of the guest molecules.

In this thesis project, muon spin spectroscopy was used for the first time to investigate the behavior of muonium (a light isotope of hydrogen) and free radicals in hydrates. Muonium (Mu) and muoniated free radicals were observed in the hydrates of cyclopentene, furan, 2,5- and 2,3-dihydrofuran, pyrrole, thiophene, isoxazole, benzene and acetone. In order to confirm that hydrates were formed, they were characterized by PXRD and solid state ^{129}Xe-NMR and ^{13}C-NMR. The free radicals were formed by addition of Mu to unsaturated organic compounds that reside as isolated guests in the hydrates. Muon and other nuclear hyperfine coupling constants (hfcs) were extracted from μSR spectra of the radicals and compared to liquid-phase data. DFT calculations of hfcs were used to guide the spectral assignments and distinguish between competing radical products where applicable. An extra μ-LCR resonance was seen in the spectra of radicals in the hydrate, indicating that they have restricted motion compared to the liquid state.

Muonium and muoniated free radicals were observed simultaneously in the hydrates of acetone and benzene. This was previously only observed in C_{60} powder and shows that Mu and the radical are in physically separated environments in the hydrates. The Mu amplitude decreases while the radical amplitude increases with temperature. This is consistent with Mu diffusion from the small cage to the large cage in the hydrates, where it can react with the guest. The diffusion occurs at a lower temperature in the acetone hydrate compared to the benzene hydrate.

Keywords: Muonium; Muoniated free radicals; Gas hydrates; DFT calculation; NMR of hydrates

Acknowledgements

I would like to start by thanking my senior supervisor, Dr. Percival for his guidance, leadership, support and patience throughout this project.

Appreciation also goes to Dr. Brodovitch for help in detailed set up of μSR experiments in TRIUMF, as well as his guidance on μ-LCR fits and field calibration. Dr. McKenzie's assistance in Jomu fits along with Dr. West and Dr. Samedov in taking shifts at TRIUMF during the experiments is appreciated. I would like to extend my thanks to all TRIUMF staff for their support during the μSR experiments. The advice of my committee members, Dr. Ghandi and Dr. Eikerling is greatly acknowledged.

A special thanks goes to the graduate students in UBC chemical engineering group who welcomed me to the world of hydrates and introduced me to Dr. Ripmeester whom not only I found a valuable scientist, but I always admired his professional personality. I would like to thank Jim Shoults from SFU machine shop who made the μSR cells on time for the beamtime at TRIUMF. Dr. Lewis was most valuable in helping with the NMR experiments of hydrates.

And a special thanks to a visiting cat at home who was my best friend during the course of this study and I appreciate the support of my family without which it was impossible to do this work.

Table of Contents

List of Tables

List of Figures

List of Acronyms

μ-LCR	muon avoided level crossing resonance
DFT	density functional theory
EPR	electron paramagnetic resonance
ESR	electron-spin resonance
HF	Hartree–Fock
hfc	hyperfine coupling constant
HFC-134a	a hydrofluorocarbon
ISAC	Isotope Separator and Accelerator
LNG	liquefied natural gas
MAS	Magic angle spinning
NMR	nuclear magnetic resonance
PXRD	Powder X-Ray Diffraction
SF_6	sulfur hexafluoride
SFU	Simon Fraser University
TBAB	Tetra-n-butyl ammonium bromide
TF-μSR	Transverse field muon spin rotation
TRIUMF	Tri University Meson Facility
UBC	University of British Columbia
μSR	muon spin rotation, resonance, and relaxation

Chapter 1.

Introduction

1.1. General concepts of muon spin spectroscopy

Radicals have an important role in chemistry but are difficult to study with most conventional spectroscopic techniques. Radicals are often short-lived intermediates in chemical reactions and it is necessary to determine their structure, reaction mechanisms, and rates in order to fully understand the reactions in which they are involved. The main method for studying radicals has been electron paramagnetic resonance (EPR), but there are alternative magnetic resonance techniques for studying radicals that are based on using the positive muon, a short-lived radioactive particle, as a spin probe. These techniques are collectively known as μSR, which stands for muon spin rotation, resonance, and relaxation.[1,2] One important difference between μSR and nuclear magnetic resonance (NMR) and electron-spin resonance (ESR) is that the muon beams can be produced with 100% polarization. NMR or ESR works based on the Boltzman population of energy levels and a radiofrequency or microwave frequency is needed to perturb the system. In μSR, no such photon is needed.[3] μSR has been used to study muoniated free radicals and muonium (analog to H atom) chemistry in various environments such as zeolites,[4,5] supercritical water,[6,7] organic liquids,[8] liquid crystals[9] and polymers.[10]

Two different techniques of μSR have been used in this work: Transverse field muon spin rotation (TF-μSR) and avoided muon level crossing resonance (μ-LCR) to measure the muon hyperfine coupling constant and other magnetic nuclei hyperfine coupling constants in muoniated radicals respectively. The details of the techniques will be given in the following sections.

1.1.1. Muon production

Muon exists in two charge states: positive and negative muons. We are only interested in positive muons. The positive muon is antimatter and was first detected by Neddermeyer and Anderson as a cosmic ray particle in 1938.[11] There are a few facilities in the world with high energy accelerators which produce muons artificially: TRIUMF in Canada, PSI in Switzerland, ISIS in the UK, J-PARC in Japan. The muon is an unstable particle with a mean lifetime of 2.2 μs. It has one-ninth mass of the proton. Table 1.1 shows positive muon properties.[12]

Table 1.1: Properties of the positive muon

Charge	+e
Mass[13,14]	0.1126095262(25) m_p = 206.7682826(46) m_e
Mean lifetime[15]	2.1969811(22) μs
Spin	1/2
Magnetic moment[16]	3.183345142(71) μ_p
Larmor precession frequency[16,17]	13.55388107(31) kHz/ G

Muons are produced by decay of pions. The positive pion decays with a mean lifetime of 26 ns into a positive muon and a neutrino:

$$\pi^+ \rightarrow \mu^+ + \upsilon_\mu \tag{1.1}$$

The pion is a spin-zero particle but the neutrino has spin 1/2 with negative helicity, i.e. with its spin pointing in the direction opposite to its momentum. In order to conserve angular momentum, the muon must also have spin 1/2 and negative helicity.[12]

When muons enter the sample (solid, liquid or gas) it loses its kinetic energy via ionization and excitation of the medium. It can then exist in three different magnetic states: a muon in diamagnetic environment (no unpaired electron), a muoniated radical and muonium.

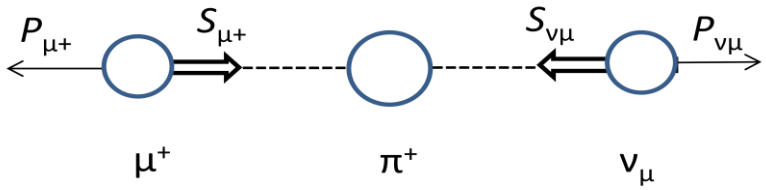

Figure 1.1: Decay of the positive pion. $P_{\mu+}$ is the momentum and $S_{\mu+}$ is the spin vector of the muon, $P_{\nu\mu}$ is the momentum and $S_{\nu\mu}$ is the spin vector of the muon neutrino.

Muons decay with an average lifetime of 2.2 μs. The muon decay is a three-body decay that gives positron, muon antineutrino and electron neutrino:

$$\mu^+ \rightarrow e^+ + \bar{\upsilon}_\mu + \upsilon_e \tag{1.2}$$

We are only interested in the probability with which a positron is emitted in a certain direction. Positrons from muon decay have a range of kinetic energies between zero and 52.3 keV.[18] As a consequence of the conservation of energy, momentum and angular momentum in this three body decay, the positron is emitted in a direction with an angle θ to the muon spin direction with a probability proportional to $1 + a.\cos\theta$, i.e., preferentially along the muon spin direction. The asymmetry a should equal 0.33 for a fully polarized muon beam but due to a number of experimental limitations it is usually 0.2-0.3.[12,19]

1.1.2. Muonium

The positive muon can form a bound state with a negative electron. This one-electron atom was dubbed muonium (Mu).[20] Chemically Mu is a light isotope of hydrogen with a mass equal to one ninth the mass of H.[21] Its ionization potential and its Bohr radius are to within 0.5% the same as those of H. Table 1.2 shows physical properties of muonium compared with the hydrogen atom.[12]

Table 1.2: Properties of muonium compared with hydrogen atom

Property	Mu	H
Mass (/m_H)	0.1131	1.0000
Reduced mass (/m_e)	0.9952	0.9995
Ionization potential (/eV)	13.539	13.598
Bohr radius (/pm)	53.17	52.94
Hyperfine coupling constant in vacuum (/MHz)	4463	1420

In muonium, the electronic spin and the muon spin are coupled by a hyperfine interaction which leads to two energy levels at zero field, a lower singlet state and a higher triplet state. In a magnetic field, the triplet levels split and the energy levels move as shown in the Breit-Rabi diagram in Figure 1.2.

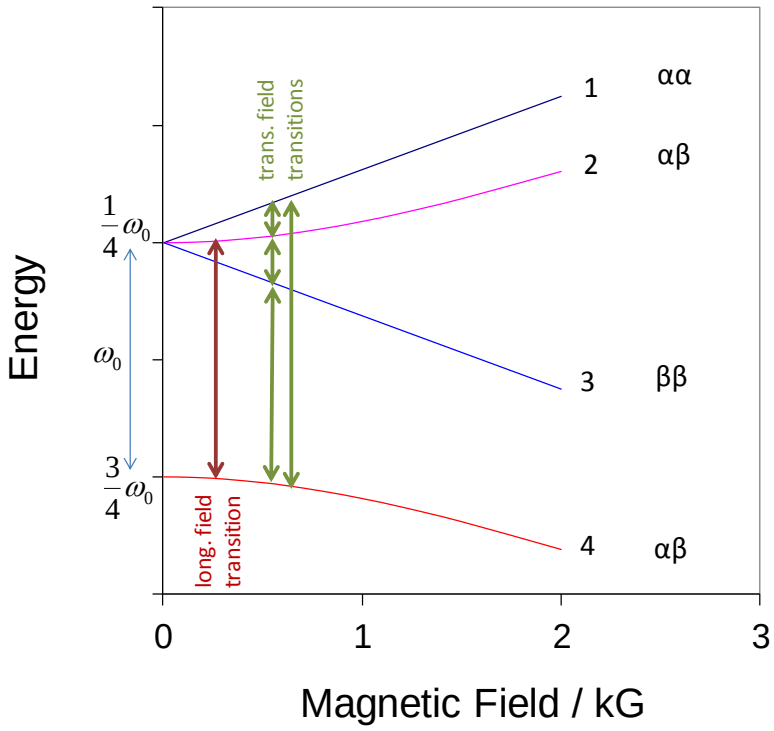

Figure 1.2: Breit-Rabi diagram for muonium. Figure from TRIUMF summer school lecture series, Percival, 2011.

The spin Hamiltonian (in units of $\hbar$) of Mu is as follows:[12]

$$\hat{H} = \omega_e \hat{S}_z - \omega_\mu \hat{I}_z^\mu + \omega_0 \hat{S} \cdot \hat{I}^\mu \tag{1.3}$$

where *S* and *I* are the electron and muon spin operators respectively. ω_e and ω_μ are Zeeman angular frequencies and ω_0 is the muon hyperfine coupling constant in angular frequency units. The eigenstates and energies of this Hamiltonian are as follows:[12]

$$|1\rangle = |\alpha_\mu \alpha_e\rangle \qquad E_1 = \tfrac{1}{4}\omega_0 + \omega_- \tag{1.4}$$

$$|2\rangle = s|\alpha_\mu \beta_e\rangle + c|\beta_\mu \alpha_e\rangle \qquad E_2 = -\tfrac{1}{4}\omega_0 + \left[\omega_+^{\,2} + \tfrac{1}{4}\omega_0^{\,2}\right]^{1/2} \tag{1.5}$$

$$|3\rangle = |\beta_\mu \beta_e\rangle \qquad E_3 = \tfrac{1}{4}\omega_0 - \omega_- \tag{1.6}$$

$$|4\rangle = c|\alpha_\mu \beta_e\rangle - s|\beta_\mu \alpha_e\rangle \qquad E_4 = -\tfrac{1}{4}\omega_0 - \left[\omega_+^{\,2} + \tfrac{1}{4}\omega_0^{\,2}\right]^{1/2} \tag{1.7}$$

where *c*, *s*, ω_+ and ω_- are as follows:

$$c = \frac{1}{\sqrt{2}}\left(1 + \frac{x}{\sqrt{1+x^2}}\right)^{\frac{1}{2}} \tag{1.8}$$

$$s = \frac{1}{\sqrt{2}}\left(1 - \frac{x}{\sqrt{1+x^2}}\right)^{\frac{1}{2}} \tag{1.9}$$

$$\omega_\pm = \frac{\omega_e \pm \omega_\mu}{2} \tag{1.10}$$

Four spectroscopic transitions are magnetic dipole allowed in transverse field ($\Delta m_e = 0$, $\Delta m_\mu = 1$):

$$\omega_{12} = \omega_- - \Omega \tag{1.11}$$

$$\omega_{23} = \omega_- + \Omega \tag{1.12}$$

$$\omega_{14} = \omega_- + \Omega + \omega_0 \tag{1.13}$$

$$\omega_{43} = \omega_- - \Omega - \omega_0 \tag{1.14}$$

where Ω is defined as:

$$\Omega = \frac{1}{2}\omega_0\left[\left(1+x^2\right)^{1/2}-1\right] \tag{1.15}$$

$$x = \frac{\omega_e + \omega_\mu}{\omega_0} \tag{1.16}$$

Of the four allowed transitions, ω_{14} and ω_{43} are too large to be resolved by conventional μSR techniques (In some systems they can be resolved depending on the hyperfine frequency). It is therefore common to observe Mu by means of its triplet precession, 1.4 MHz/G, in low fields (< 20 Gauss) where ω_{12} and ω_{23} are degenerate frequencies. At intermediate fields the degeneracy will be lifted and the two frequencies are observed by Fourier transforming the time spectrum. Figure 1.3 is an example of Mu precession frequencies in a field of 100 G in cyclopentane hydrate.

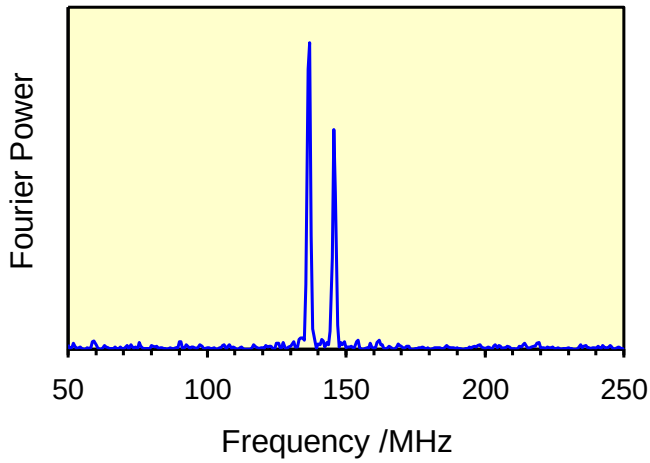

Figure 1.3: Fourier power spectrum of split Mu precession frequencies in a field of 100 G in cyclopentane hydrate at -10ºC. Adapted with permission.[22] Copyright 2014, American Chemical Society.

In longitudinal field there is only one allowed transition: ω_{24} as shown in Figure 1.2.

1.1.3. Muoniated radicals

Isotopically enriched samples are used to obtain more detailed information on the electron spin density distribution in structural studies. Measurements of the coupling constants of deuterated methyl and ethyl radicals showed that the ratio of proton to deuteron couplings exceeds the ratio of magnetic moments. This has been explained in

terms of vibrational averaging.[23,24] The vibrational wave functions are mass dependent. This leads to isotope effects in vibrationally averaged coupling constants. Corresponding changes are expected to be much larger in muoniated radicals.[12] Muoniated radicals are typically formed by addition of muonium to unsaturated molecules. They are paramagnetic species in which the unpaired electron spin couples to the muon and any other magnetic nuclei.

The spin Hamiltonian for such a system is given by:

$$\hat{H} = \omega_e \hat{S}_z - \omega_\mu \hat{I}_z^\mu + \omega_0^\mu \hat{S} \cdot \hat{I}^\mu - \sum_k \omega_k \hat{I}_z^k + \sum_k \omega_0^k \hat{S} \cdot \hat{I}^k \qquad (1.17)$$

ω_0^μ and ω_0^k are the Fermi contact hyperfine coupling constants for muon and the nucleus k respectively. ω_e, ω_μ and ω_k are Zeeman angular frequencies. For *N* nuclei with spin quantum numbers I_k this Hamiltonian leads to $4\prod_k(2I_k+1)$ eigenstates and the system generally oscillates between many of these states. Consequently, the muon polarization is distributed over many frequencies. For low fields, in particular, this makes the detection of muonium substituted radicals difficult or even impossible. However in higher fields satisfying the condition ω_e >> ω_0^μ, ω_0^k for all k, the frequency spectrum is considerably simplified.[25] The radical frequencies ($\omega = 2\pi\nu$) form two degenerate groups, independent of the number of coupled nuclei. These frequencies are

$$\nu_{R1} = \nu_m - \tfrac{1}{2} A_\mu$$

$$\nu_{R2} = \nu_m + \tfrac{1}{2} A_\mu$$

where the mid-point

$$\nu_m = \frac{1}{2}\left[\left[A_\mu^2 + (\nu_e + \nu_\mu)^2\right]^{1/2} - \nu_e + \nu_\mu\right] \qquad (1.18)$$

is shifted from the muon Larmor frequency by a small amount that depends on the relative magnitudes of the isotropic muon hyperfine constant A_μ (in frequency unit) and the electron Larmor frequency ν_e.[8] For example, in Figure 1.4 ν_{R1} and ν_{R2} appear at -30 and +346 MHz respectively. The difference between the two frequencies gives the muon hyperfine constant, A_μ, which is 376 MHz in this case.[22]

1.1.4. Transverse field muon spin rotation

Transverse field muon spin rotation or TF-μSR is used to measure the muon hyperfine coupling constant (hfc). The muon is injected into the sample with its spin perpendicular to the external magnetic field. Each incoming muon passes through a muon counter which starts a fast electronic clock. The muon spin precesses in the magnetic field and will decay to give a positron. The clock is stopped by the detection of the corresponding decay positron in one of the positron detectors. After collecting several million events, the data are displayed as a histogram of the number of decay positrons detected in a given direction as a function of the lifetime of the muons, and resemble the free induction decay that follows a π/2 pulse in nuclear magnetic resonance (NMR).[26]

The histogram has the following form:

$$N(t) = N_0 \, \mathrm{e}^{-t/\tau}[1 + A(t)] + C \tag{1.19}$$

where N_0 is a normalization factor, τ is the mean muon lifetime (2.2 μs) and C is a small constant background. $A(t)$ is the muon asymmetry function, which incorporates the precession signals.

$$A(t) = aP(t) = \sum_i A_i e^{-\lambda_i t} \cos(2\pi \upsilon_i t + \phi_i) \tag{1.20}$$

$A(t)$ is related to the time dependence of the muon spin polarization $P(t)$ by a simple scale factor, a, which depends on various instrumental parameters. Individual precession frequencies υ_i can be identified by Fourier transformation of $A(t)$.[12] When the

spectrometer has four positron detectors arranged in phase quadrature, complex Fourier transformation can be used to produce a spectrum which distinguishes negative from positive precession frequencies. Figure 1.4 is an example of radical precession frequencies of muoniated cyclopentyl in liquid cyclopentene at -10°C and 11.6 kG. The truncated peak at 157 MHz is due to muons incorporated in diamagnetic molecules. The peaks at -30 and +346 MHz are due to a muoniated free radical.

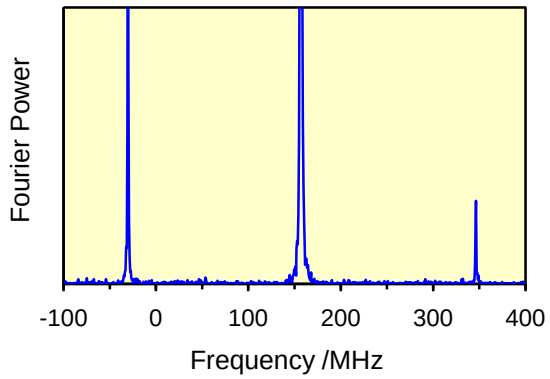

Figure 1.4: Fourier power TF-μSR spectrum of liquid cyclopentene at -10°C and 11.6 kG. The truncated peak at 157 MHz is due to muons incorporated in diamagnetic molecules. The peaks at -30 and +346 MHz are due to a muoniated free radical. Adapted with permission.[27] Copyright 2016, American Chemical Society.

1.1.5. Avoided muon level crossing resonance

Abragam proposed to make use of the effect of avoided level crossing to detect hyperfine splitting of paramagnetic ions in longitudinal field μSR (μ-LCR).[28] In muon avoided level crossing resonance, the muons are injected with their spins parallel to the external magnetic field. The positrons which are emitted preferentially along the muon spin direction are counted in a pair of detectors in the forward (F) and backward (B) directions. The muon asymmetry is given by the normalized difference of the integrated count rates:

$$A = a\overline{P}_z(B) = \frac{(N_F - N_B)}{(N_F + N_B)} \tag{1.21}$$

a is a constant reflecting the initial muon polarization in the beam, the muon decay asymmetry and the geometry of the experimental arrangement. $\overline{P}_z(B)$ is the time averaged normalized *z*-component of the muon polarization.[29] Avoided level crossing resonance occurs at specific magnetic fields where a muon transition frequency is matched with some other nucleus in the coupled spin system. In high magnetic fields, the eigenstates of the spin system are pure products of Zeeman states to a good approximation. However, near avoided crossings eigenstates are mixtures between two Zeeman states, which leads to an oscillation between the levels with frequency corresponding to the energy difference between the levels.[30] At the appropriate magnetic field mixing of a pair of nearly degenerate levels having different spin orientations for the muon and other nucleus can occur due to the hyperfine interactions. The resulting transfer of polarization from the muon to the other nucleus is detected as a resonant-like change in the spectrum as the magnetic field is swept through the LCR position. The general expression for the muon polarization in the high field limit (ω_e >> $\omega_0^{\mu}, \omega_0^{k}$) is given by:

$$P_z(B) = 1 - \frac{2}{N}\sum_{i}^{2I_k} \frac{\omega_{0i}^2}{\lambda^2 + \omega_{0i}^2 + [2\pi(B - B_{0i})(\gamma_\mu - \gamma_k)]^2} \tag{1.22}$$

N is the dimension of the Hamiltonian matrix, γ_μ and γ_k are the gyromagnetic ratios of the muon and other nuclei respectively. λ is the damping rate which describes any process that takes the muon out of the LCR resonance, usually the physical muon decay and chemical reactions. ω_{0i} is the energy gap or LCR transition frequency and B_{0i} is the resonance field, which is given by:

$$B_{0i} = \left| \frac{A_\mu - A_k}{2(\gamma_\mu - \gamma_k)} - \frac{A_\mu^2 - 2MA_k^2}{2\gamma_e(A_\mu - A_k)} \right| \tag{1.23}$$

where M is the total of the magnetic quantum numbers of electron, muon and nucleus k: $M = m_e + m_\mu + m_k$. A_μ and A_k are the muon and nuclear hyperfine coupling constants respectively.[29] The resonances are governed by the selection rules: $\Delta M = 0$

resonance (muon-nuclear spin flip-flop transitions) takes place if the hyperfine action is isotropic such as the case for liquids; $\Delta M = 1$ resonance (muon spin flip) arises from the dipolar part of the hyperfine interaction in rigid media.[30] $\Delta M = 0$ resonances are used to calculate hyperfine coupling constants of spin-active nuclei other than the muon in the radical, by using equation 1.23. However, $\Delta M = 1$ resonances are seen in solids or other media where anisotropic interactions are not averaged by rapid tumbling of the molecules (unlike the case of liquid).[31] Muon hyperfine coupling constants are calculated from $\Delta M = 1$ resonances by using the following equation:

$$B_{LCR} = \frac{1}{2} A_{\mu} \left[\frac{1}{\gamma_{\mu}} - \frac{1}{\gamma_e} \right] \tag{1.24}$$

The major advantage of μ-LCR over TF-μSR is that the coupling constants of nuclei other than the muon are obtained. Also, radicals will be observed even when a Mu precursor has a lifetime of a microsecond as long as the transition frequency is high enough to produce a significant LCR signal in the remaining muon lifetime. In contrast, in transverse field experiments the muon polarization is lost when the Mu precursor lifetime exceeds 10^{-10} s.[12]

An example of a μ-LCR resonance is shown in Figure 1.5.

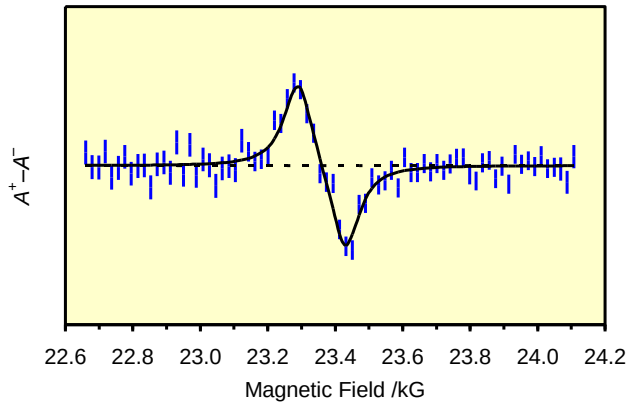

Figure 1.5: Example of a μ-LCR resonance. This one is part of a spectrum obtained from neat liquid cyclopentene at -10°C, and can be assigned to the α-H of the muoniated cyclopentyl radical. Adapted with permission.[22] Copyright 2014, American Chemical Society.

1.2. General concepts on gas hydrates

The term "gas hydrate" is used for the solids which are formed by the combination of gases and volatile liquids with a large excess of water. In 1810, Humphry Davy, in the Bakerian lecture to the Royal Society, reported that an aqueous solution of chlorine froze more readily than water itself.[32] In 1823, Faraday found the composition of the solid formed to be roughly $Cl_2.10H_2O$.[33] However, incomplete drying of the crystals or loss of gas during the analysis could have led to underestimation of the chlorine content. This was indeed the case, so Faraday's work shows the difficulties in direct analysis of gas hydrates. Another question was the nature of the forces uniting the gas and water molecules. It was early recognized that these forces are much weaker than those of primary chemical bonds.[34] Hammerschmidt proposed that hydrates were more likely to block pipelines than ice, and it led to a large number of studies on the phase equilibria of hydrocarbon hydrates and their inhibition in the 1930s by the engineering community.[35] Powell proposed clathrates as a structurally unique class of materials.[36] He observed that one material, the guest, could be trapped within another, the host, without obvious directional bonding between the components. Powell first discovered quinol clathrate

where the guest may be SO_2, H_2S, HCN, HCl, HBr, HCO_2H, CH_3OH or CH_3CN.[37] Claussen, von Stackelberg and coworkers, and Pauling and Marsh had identified the hydrates as clathrates within a few years of Powell's discovery.[38,39,40] As a result of their discovery, we know the families of hydrate structures well-known as cubic structures I and II, and the three constituent cages: dodecahedron-5^{12}, tetrakaidecahedron-$5^{12}6^2$ and hexakaidecahedron-$5^{12}6^4$. The crystal structures of hydrates were explored at great length by Jeffrey, Ripmeester and coworkers in the 1960s and 1970s, who categorized and classified a large number of actual and hypothetical structures.[41,42]

A large amount of natural gas, mainly methane, is formed naturally in the form of hydrates in marine and permafrost environments. Natural gas is the cleanest burning fossil fuel and has been identified as a strong candidate for energy resource compared to oil and coal. Methane gas hydrate is an energy resource for methane that has a carbon quantity twice more than all fossil fuels combined and is distributed evenly around the world.[43] The first assessment of potential resources has recently shown a preliminary estimate of ultimate global recoverable volumes on the order of 3×10^{13} m^3. Other occurrences, such as gas hydrate-filled fractures in clay-dominated reservoirs, may also become potential energy production targets in the future.[44] As a result, many research areas cover gas hydrates from fundamental and application studies[45] to environmental issues[46] and engineering aspects[47,48].

1.2.1. Gas hydrate structures and formation

Gas hydrates are crystalline compounds that form when water (or ice) comes into contact with small molecules (called hydrate guests) under certain pressure and temperature conditions. In practice, these compounds are commonly referred to as gas hydrates, clathrate hydrates, or just hydrates. While specific to the particular hydrate guest, gas hydrates are stable typically at high pressures and low temperatures. A wide range of molecules have been shown to form gas hydrates. When hydrates form, water crystallizes to create a lattice of molecular-sized cages that trap guest molecules without chemical bonding between the host water and the guest molecules. Figure 1.6 shows trapping of gas molecules in the gas hydrate lattice.[49,50]

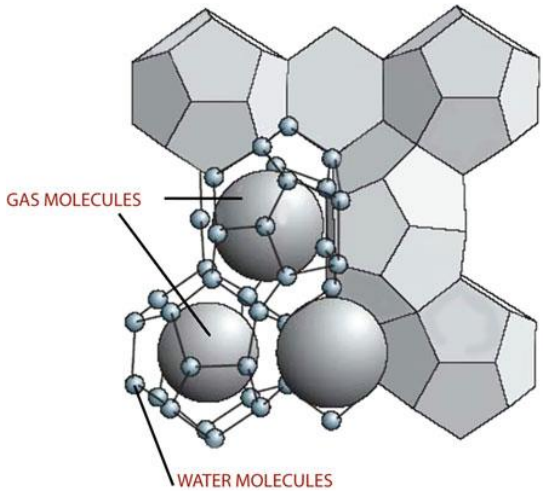

Figure 1.6: The inclusion or trapping of gas molecules in the gas hydrate lattice. The molecular-sized ‘‘cages’’ are composed of hydrogen bonded water molecules (Reproduced from SETARAM). Adapted with permission.[49] Copyright 2011, Springer.

Gas hydrates are made up of water molecules that are connected through hydrogen bonding. Through hydrogen bonds, each water molecule is attached to four others, donating two and accepting two hydrogen bonds. Each proton of the molecule is attracted to the negative pole of a neighboring molecule. Also, the two negative poles on the initial molecule attract the positive poles from two other water molecules. The four surrounding molecules are arranged tetrahedrally around the central molecule. Of more than 130 compounds that are known to form clathrate hydrates with water molecules, the majority form either structure I (sI), structure II (sII), or structure H (sH).[51]

The hydrate structures are composed of five polyhedra formed by hydrogen-bonded water molecules shown in Figure 1.7.[52]

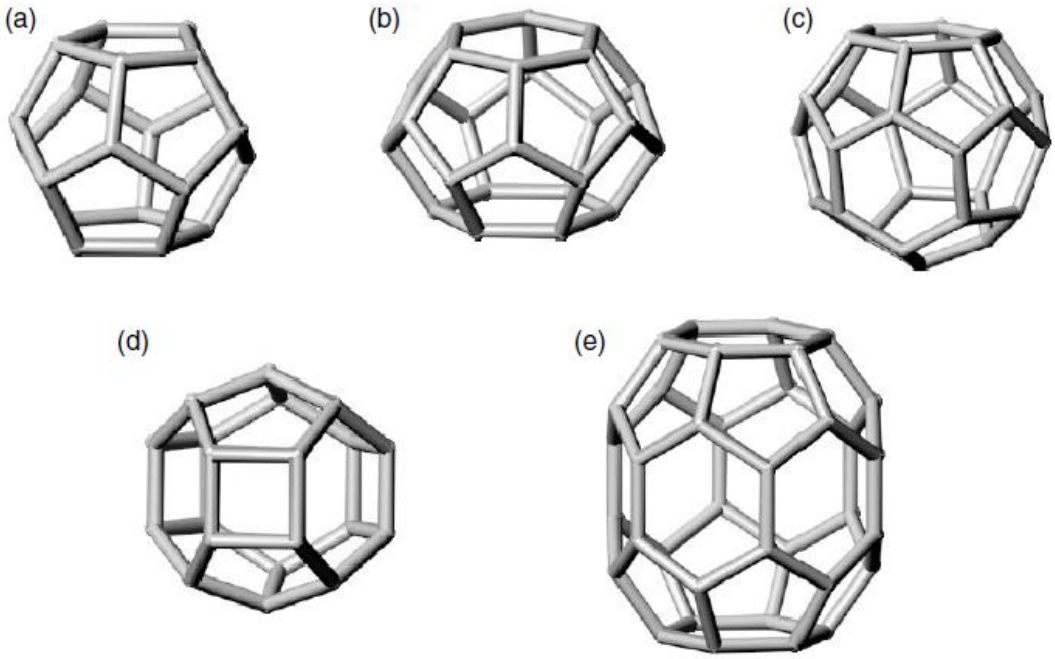

Figure 1.7: Five cavities in gas hydrates: (a) pentagonal dodecahedron (5^{12}), (b) tetrakaidecahedron ($5^{12}6^2$), (c) hexakaidecahedron ($5^{12}6^4$), (d) irregular dodecahedron ($4^35^66^3$), and (e) icosahedron ($5^{12}6^8$). Adapted with permission.[52] Copyright 2009, AIP Publishing LLC.

The pentagonal dodecahedron (12-sided cavity) of Figure 1.7 is labeled 5^{12} because it has 12 pentagonal faces with equal edge lengths and equal angles. The 14-sided cavity (tetrakaidecahedron) is called $5^{12}6^2$ because it has 12 pentagonal and 2 hexagonal faces. The 16-hedron (hexakaidecahedral cavity) is denoted $5^{12}6^4$ because in addition to 12 pentagonal faces, it contains 4 hexagonal faces. The irregular dodecahedron cavity ($4^35^66^3$) has three square faces and six pentagonal faces, in addition to three hexagonal faces. The largest icosahedron cavity ($5^{12}6^8$) has 12 pentagonal faces and 8 hexagonal faces.[51]

Small hydrate guests (diameter, $d \sim 4.0$ Å, *e.g.*, N_2), and larger molecules ($d \sim$ 6–7 Å, *e.g.*, C_3H_8) form sII with lattice constant $a \sim 17$ Å. This structure has two types of cavity: sixteen small (5^{12}) and eight large ($5^{12}6^4$) cavities per unit cell. Molecules in the size range $d \sim 4$–6 Å (*e.g.*, CH_4 and C_2H_6) form sI with lattice constant $a \sim 12$ Å. This structure also has two cavity types: two small (5^{12}) and six large ($5^{12}6^2$) cavities per unit

cell. The structure containing the largest of guest molecules is sH, where two molecules are needed to stabilize a hexagonal lattice (a ~ 12 Å, c ~ 10 Å). To form sH, a large guest (d ~ 7.5–9 Å), such as methylcyclohexane, must occupy the large ($5^{12}6^8$) cavity (one per unit cell) combined with a guest (*e.g.*, CH_4) that will fit inside the smaller cavities ($4^35^66^3$; two per unit cell and 5^{12}; three per unit cell). Fig. 1.8 shows the three common clathrate hydrate structures.[53]

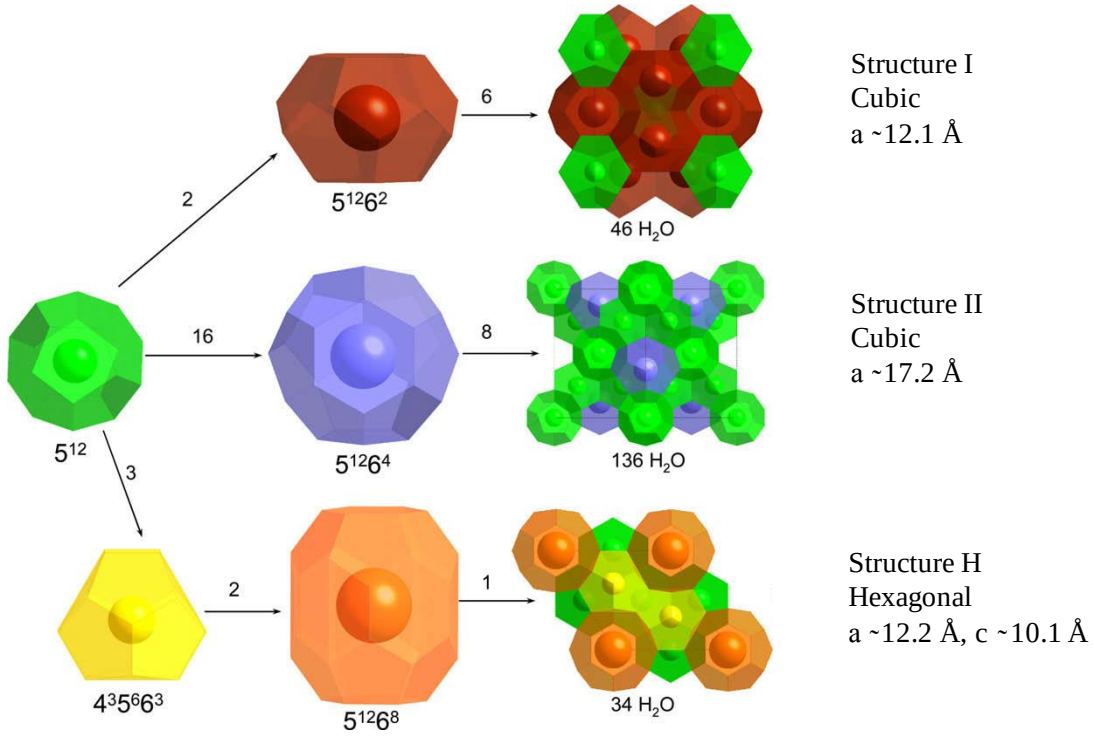

Figure 1.8: Common clathrate hydrate structures. Adapted with permission[53]. Copyright 2009, Elsevier.

Hydrate forms from ice when a new phase forms on the surface of ice. Hydrate nucleation happens when crystal embryos attain a critical size and then growth can occur. Lattice cracks and defects are considered as potential nucleus forming sites. Induction period is the time during which nucleation takes place. Nucleation is assumed to be a stochastic process and the induction time is a function of temperature and pressure for hydrate nucleation from ice.[51] For the case of xenon structure I hydrate

nucleation from ice, induction times of 10-100 s were observed before the formation of surface hydrate which depended on the pressure and temperature of the gas. Also the concentration of occupied small cages was higher at the initial moments after adsorption. This could indicate a special role for the 5^{12} cage in the formation of xenon hydrate precursor.[54]

Figure 1.9 shows a typical phase diagram for a pure hydrocarbon larger than methane.[49] It is important to know about the phase diagrams because they show hydrate stability zone. To the left of the green line in Figure 1.9 is where the hydrate is stable (lower temperatures and high pressures). Q_1 is the lower quadruple point where the four phases of liquid water, ice, hydrate and hydrocarbon vapor exist together. Below Q_1 hydrates form from ice instead of liquid water. Q_2 is the upper quadruple point where liquid water, hydrate, hydrocarbon vapor and liquid coexist. The dashed curve shows hydrocarbon transition from the vapor to the liquid phase. Q_2 gives an upper temperature limit for hydrate formation.[49]

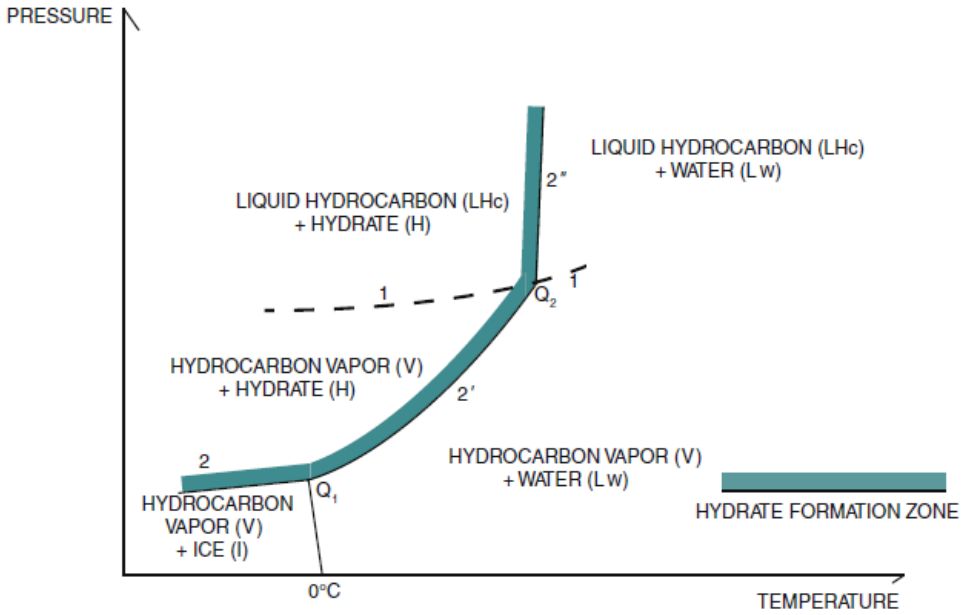

Figure 1.9: A typical P-T diagram for a pure hydrocarbon (larger than methane). Adapted with permission.[49] Copyright 2011, Springer.

1.2.2. Gas hydrate applications

Natural reserves of gas hydrates in the earth can be used as a gas supply to provide the energy need of the world. Gas hydrates found in the earth's crust are considered a source of natural gas that is mostly methane gas and is considered a cleaner source of energy than oil and coal.[55]

Several studies show that the gas hydrate structures have considerable potential as storage media for various gases. For instance, they can be used for hydrogen storage[53] and gas transportation. Detailed economic studies show that the capital cost for natural gas transportation in the form of gas hydrates is lower than that for liquefied natural gas (LNG), mainly because of lower investment in infrastructure and equipment.[56] Another application of gas hydrates is in carbon dioxide sequestration. One novel approach to separate carbon dioxide from combustion flue gas is through gas hydrate crystallization techniques. Due to the difference in affinity between CO_2 and other gases in the hydrate cages when hydrate crystals are formed from a binary mixture of these gases, the hydrate phase is enriched in CO_2 while the concentration of other gases is increased in the gas phase. The hydrate phase can be later dissociated by depressurization and or heating and consequently CO_2 can be recovered.[57]

Gas hydrates are used in gas separation processes. For example, tetra-n-butyl ammonium bromide (TBAB) hydrate has been used to separate H_2S from a mixture of gases in biogas.[58] The small dodecahedral cages have empty spaces so they can capture small gas molecules such as H_2S.[59]

The separation of greenhouse gases such as hydrofluorocarbon (HFC-134a) from air and sulfur hexafluoride (SF_6) from nitrogen have been done using gas hydrates, and the results have been compared with conventional techniques such as liquefaction separation processes. It has been shown that for the case of SF_6, the hydrate process is preferable to liquefaction in terms of energy consumption (removal of heat for the phase transition). However, liquefaction consumes less energy than the hydrate process for hydrofluorocarbon separation.[60]

Another application of gas hydrates is in desalination of sea water which is important for producing fresh water. When hydrates form, salt ions are excluded from entering the structure. For example, methane hydrate can form by injecting methane into sea water at the hydrate stability zone and then the hydrate rises to where it is decomposed into methane and water. The water is recovered and methane is recycled.[61] First commercial application of desalination of water by propane hydrate dates back to 1961 and 1967.[62,63] However, there is still a need for further research in this area for it to be economically and technically available for use.[64]

A relatively new application of gas hydrates is in biotechnology, where gas hydrates may form in animal or plant tissues. Gas hydrates have applications in controlling enzymes in biological systems.[65] Forming gas hydrates is a new technique for the back extraction of amino acids from reverse micelles which requires appropriate thermodynamic conditions of temperature and pressure. For example, CO_2 hydrate was used to recover L-aspartic acid from the reverse micelle solution. Hydrate formation breaks the micelle by reducing the amount of water in it and the amino acid precipitates.[66]

1.3. Importance of this study

Although a wide variety of research has been done on gas hydrates and their multiple applications in industry, there is still a need of research on their fundamental properties. In order to control gas hydrates' behavior, one needs to understand them on the molecular level.[67]

There is little known about the chemistry of radicals in gas hydrates. In 1963, Goldberg studied the radicals of CH_3S and C_2H_5S in the clathrate hydrates of CH_3SH and C_2H_5SH respectively. The radicals that were generated by photo-dissociation of the guest molecules did not recombine at temperatures almost up to the hydrate decomposition point.[68] Methyl and ethyl radicals have been studied by ESR of gamma-ray irradiated methane and ethane hydrates respectively.[69,70] The activation energy of the decay reactions of the radicals matches the hydrate dissociation enthalpies.

It has been shown that when propane hydrate is gamma-ray irradiated, H atom transfers from a propane molecule in a large cage to the n-propyl radical in an adjacent cage. This process generates isopropyl radicals and so the concentration of isopropyl radicals increases and n-propyl radicals decreases while the total amount of radicals is almost constant.[71] Similarly, in a mixed hydrate of methane and propane, methyl radicals can pick up H atoms from the propane molecules in the adjacent cages. H atoms are abstracted from propane, generating n-propyl and isopropyl radicals.[72]

Carboxyl radical, HOCO, which is important in atmospheric chemistry and combustion, was studied in gamma-ray irradiated CO_2 hydrate by ESR. HOCO radical is an intermediate species in the CO + OH $\rightarrow$ CO_2 + H reaction. It was shown that the decay mechanism of HOCO radicals proceeds via second-order decay. CO_2 in one cage withdraws a hydrogen atom from HOCO radical in an adjacent cage. The so-called "hydrogen atom hopping reaction" results in diffusion of HOCO radicals in the hydrate without self diffusion.[73] HOCO radical has been observed in mixed methane and CO_2 hydrate as well. Both methyl and HOCO radicals were observed at 120 K by ESR. The radicals were formed synergistically by reactions between the radiolysis products of water ($H^{\bullet}$, $OH^{\bullet}$, e^{-}) and the hydrate guests: methane and CO_2.[74]

Among the computational research that has been done is the work of Koh et al., who studied CO radical cation transfer through hexagonal faces of large cages in structure I hydrate.[75] Alavi et al. determined energy barriers of hydrogen radical migration in structure II hydrate through pentagonal and hexagonal faces of small and large cages.[76]

Gas hydrates are thought as nano-reactors where target reactions can occur.[75] 3-buten-2-one molecule prefers the trans conformation in the liquid phase but takes the cis conformation in the large cavity of structure II hydrate (with methane in small cages).[77] However, upon gamma-irradiation the trans form of the molecule was observed. The reaction mechanism was described in terms of intracavity conformational change of 3-buten-2-one molecule. This happens because ketyl radicals were formed when the hydrate was gamma irradiated. The radical returns to the trans form of 3-buten-2-one molecule by transferring the electron to the neighboring 3-buten-2-one

molecule in the large cavity. This conformational change increases thermodynamic stability of the hydrate phase.[77]

The motivation of this study comes from the fact that it is important to study radicals since they are intermediates in many reaction mechanisms. The unique structure of hydrates (each radical trapped in one cage) makes it possible to study radical behavior up to the temperature at which the hydrate is stable. Also, little is known about the chemistry of radicals in gas hydrates. ESR, a common technique to study radicals, has been used to detect radicals formed in the hydrates of methane, ethane, propane and carbon dioxide as mentioned in the earlier paragraphs. An alternative approach to ESR is to study the radical species with μSR. The advantage of the latter is that the spectrum is not as complex as ESR, i.e. there is one pair of precession frequencies for each radical formed. Also, by gamma irradiating the hydrates there will be other active species in the environment, e^-, $H^\bullet$ and $OH^\bullet$ (coming from dissociation of the water cages), which may react with the hydrate guests and cause ambiguity. However, in μSR the radicals are formed from guest molecules only.

In this thesis project, muon spin spectroscopy was used for the first time to investigate the behavior of muonium (a light isotope of hydrogen) and free radicals in hydrates. Cyclopentene, furan, 2,5- and 2,3-dihydrofuran hydrates were chosen to study first since they are easy to make and are stable at room pressure. Hydrates of ethene and propene couldn't be studied since they need to be kept under high pressure and the necessary beamline in TRIUMF which produced high energy beam, M9B was not operational.

Chapter 2.

Experimental and theoretical methods

2.1. μSR experiments at TRIUMF

TRIUMF is Canada's national laboratory for particle and nuclear physics and accelerator-based science. The acronym is an abbreviation for TRI University Meson Facility. TRIUMF was founded in 1968 by Simon Fraser University, the University of British Columbia (UBC), and the University of Victoria. More universities across Canada joined TRIUMF since then as it provides research tools that are too complicated for a single university to operate.[78] All the μSR experiments that are reported in this thesis were performed at TRIUMF.

TRIUMF has a 500 MeV cyclotron that accelerates negatively charged hydrogen ions, H^-. These ions lose their electrons by passing through a stripping foil. The positively charged protons are thus extracted to the proton beam lines. There are four proton beam lines: 1A, 2A, 2C and 4. Beam line 1A delivers protons with energies between 180 and 500 MeV to the two targets in the Meson Hall. The first target T1, serves three experimental channels: M11, M13 and M15. The second target T2, serves M9 and M20 channels. All μSR experiments were performed at M15 and M20 channels where surface muons are generated. Beam line 2A delivers protons to the ISAC (Isotope Separator and Accelerator) facility. Beam line 2C is used for proton therapy and medical imaging. Beam line 4 provides beam for the experiments in the Proton Hall.[79]

Our research group took one or two weeks of beam time in the Fall and Summer (November 2012 to July 2016). The beam ran for 24 hours per day during those weeks. Everyone in the group took shifts to collect data. Also our collaborators, Dr. Kerim Samedov and Dr. Iain McKenzie took shifts. So collecting data for this thesis was a

collaborative work. However, I made the samples and did the data analysis, including all the fits and calculations.

2.1.1. Surface muons

Surface muons are generated from low energy pions which stop at the target surface and decay at rest. The surface muons are monoenergetic with the energy of 4.12 MeV and momentum of 29.8 MeV/c. The idea of surface muons came from the university of Arizona research group working at Lawrence Berkeley Laboratory.[80] They identified low energy positive muons and used them for experiments on samples like gases with low density. The advantage of surface muons is that they have a beam of almost 100% spin polarization. However, the beam may be contaminated with positrons that come from muon decay inside the target and muons which decay in flight. In order to remove the contamination, a DC separator is used. The separator has a vertical electric field and a horizontal magnetic field that are used to remove the contamination from the muon beam and rotate the muon spin polarization (for TF-μSR experiments).[81] The surface muons have a stopping range of about 160 mg/cm^2 which permits μSR experiments on thin targets.[82]

2.1.2. μSR apparatus

The μSR spectrometer involves a magnet and detectors to detect muons and decay positrons. Two types of magnets were used for this work: Helios for high field and Lampf for low field experiments. Helios is a superconducting magnet capable of producing fields as high as 60 kG. Most of the studies of muoniated radicals were done using Helios. On the other hand, Lampf is a Helmholtz type of magnet producing maximum 4 kG. Lampf is suitable for muonium studies where there is a need of low magnetic fields.[83]

To change the magnitude of the magnetic field during the experiment, one sets the magnetic field by adjusting the current in the magnet coils. The magnets generate about 4 G/A in Lampf and 962 G/A in Helios. In order to determine the accurate magnitude of magnetic field, there is a need to do a field calibration during every beam

time. The field calibration is done by measuring the diamagnetic frequency in a series of short TF-μSR runs. The frequency is then converted to the magnetic field using the following equation:

$$\nu_D = \gamma_\mu \times B \tag{2.1}$$

Detectors are plastic scintillation counters that emit light when an ionizing particle passes through. In this case incoming muons and decay positrons cause ionization and generate a flash of light. The light is transmitted via a light guide to a photomultiplier tube where amplification and conversion to an electrical signal occurs. The light guide is about one meter long so that it extends outside the high magnetic field area so that the photomultiplier tube won't be negatively affected. This in turn limits the time resolution of μSR experiments to 1 ns.[84]

To control the temperature of the samples two types of equipment were used: for liquid samples, a Thermo Haake circulator with a temperature range of -15 to 25°C; and for hydrate samples, a helium gas flow cryostat from 50 to 280 K.[85]

2.1.3. TF-μSR experiment

Figure 2.1 shows a schematic diagram for a TF-μSR experiment. The Sample, S, is located in a magnetic field which is parallel to the muon momentum but is perpendicular to the muon spin. When the incoming muons go through the muon detector, a start pulse in a time digitizer (clock) is generated. The muons then enter the sample and decay to positrons.[86] The positron detectors are arranged up-right, up-left, down-right and down-left of the sample. Only the up and down detectors are shown in the figure for simplicity. This arrangement allows complex Fourier transforms, and consequently to distinguish between positive and negative frequencies. When a positron is detected, a stop pulse is recorded in the clock. The time interval between the start and stop is registered as an event and the corresponding bin in a time histogram is increased by one. Each positron must be correlated with a particular muon unambiguously. If a second muon or positron is detected during the first time interval or data gate, the event will be rejected. Such events are called pile-up events and they are all rejected.[84]

Usually there are about 10^7 events in a histogram and a typical TF-μSR experiment takes about an hour and a half.

The histogram shown in Figure 2.1 is a simulation of a raw μSR spectrum which shows the number of positrons as a function of time (μs). The decay of the average counts shows the finite muon lifetime and the anisotropy of the muon decay appears as oscillations in the actual counts.[86]

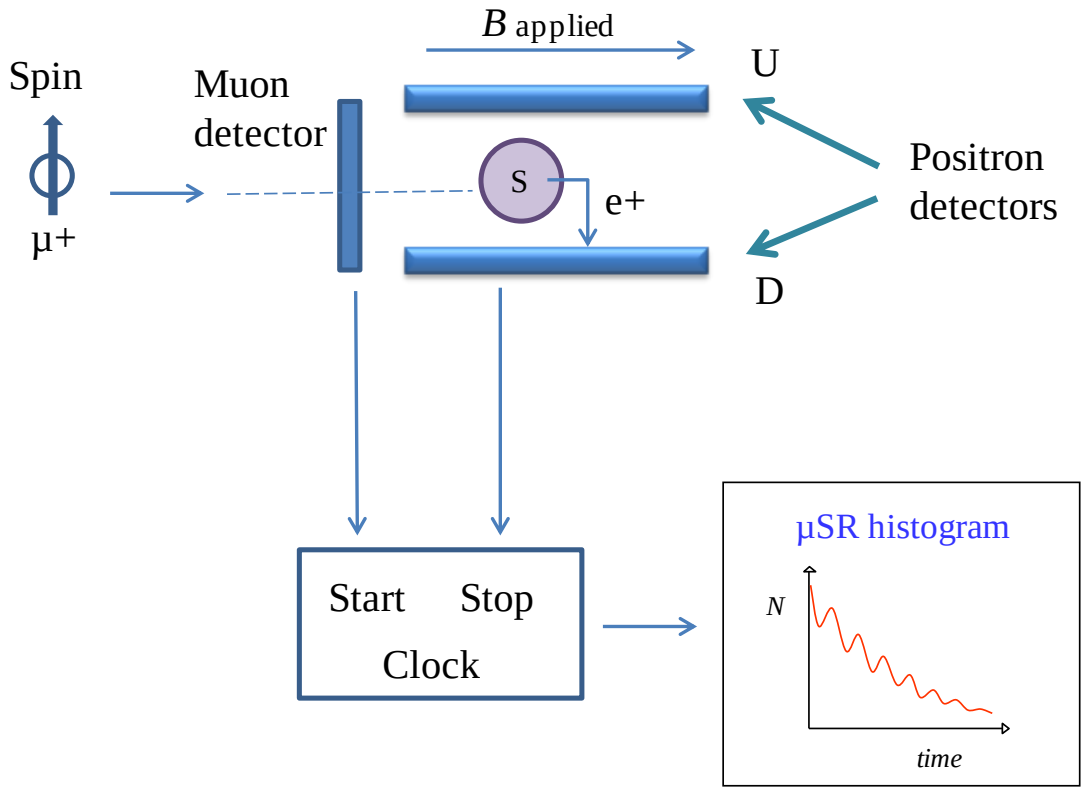

Figure 2.1: Schematic for TF-μSR experiment.

2.1.4. μ-LCR experiment

A schematic diagram of a μ-LCR experiment is shown in Figure 2.2. In avoided muon level crossing resonance, the muon enters the magnetic field with spin and momentum parallel to the field. The detectors are located backward and forward to the sample. The time-integrated muon decay asymmetry is measured as a function of magnetic field. The asymmetry is defined as the normalized difference between forward and backward detector counts. There is no requirement of having only one muon in the

sample at a time so the muon beam intensity is usually high. The raw integrated asymmetry is sensitive to systematic effects such as fluctuations in the rate of incoming muons. In order to minimize such effects a small square-wave field modulation is used and the results are displayed as the difference between signal accumulated with the opposite modulation phases: A^+-A^- as shown in the μ-LCR spectrum in Figure 2.2. A^+ and A^- refer to muon asymmetries when modulation is applied parallel and anti-parallel to the magnetic field.[87] When the field modulation width is smaller than the resonance linewidth the lineshape appears to have a differential shape similar to conventional ESR signals.[88] μ-LCR experiments usually take longer time than TF-μSR experiments. If the signal is small, it needs more scans with smaller step size and so takes more time.

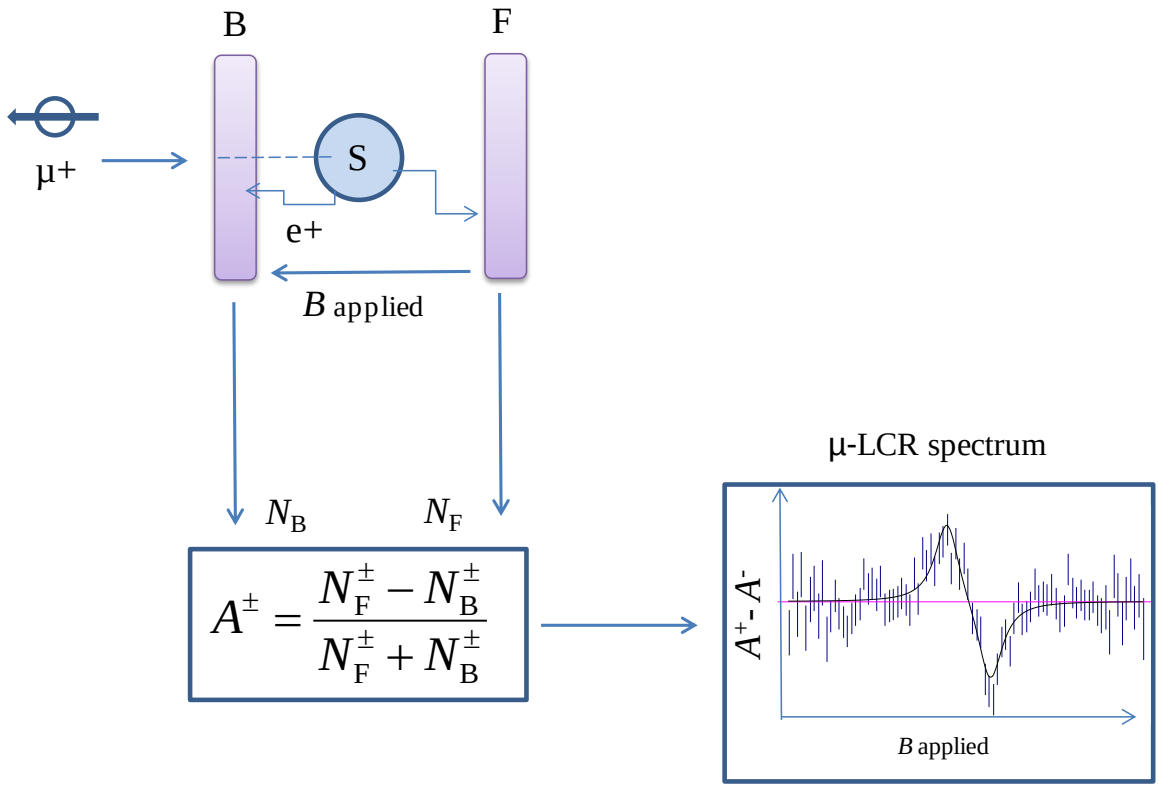

Figure 2.2: Schematic for μ-LCR experiment.

2.1.5. Data analysis

TF-μSR spectra were fitted using a program called JOMU. This program was written by Dr. Schüth who was a previous group member. This program processes the raw data in a form that can be Fourier transformed. It is used to get approximate frequencies for the strongest signals. These signals are fit in time space by a least-squares minimization procedure. The fits give amplitude, frequency, relaxation and phase for every signal. Each histogram was fitted separately. The fit data were then transferred to EXCEL to take the weighted average of the four (or in some cases 2) histograms. Muon hyperfine coupling constants were either calculated from the difference of the two radical frequencies ν_{R1} and ν_{R2} or by using the following formula:

$$A_{\mu} = 2\frac{\left(\nu_{\mu} - \nu_{R1}\right)\left(\nu_{e} + \nu_{R1}\right)}{\nu_{e} - \nu_{\mu} + 2\nu_{R1}} \tag{2.2}$$

where ν_{μ} is the diamagnetic frequency of the muon, ν_{R1} is the lower radical frequency and ν_{e} is the electron Larmor frequency. The Fourier power TF-μSR plots were generated by using the msrfft program which can be accessed by logging into one of the TRIUMF computers. Complex Fourier Transforms were taken of appropriate combinations of histograms to generate spectra corresponding to both positive and negative frequencies and stored as text files. These files can be downloaded to a computer using WinSCP program and manipulated in EXCEL to plot the data.

μ-LCR resonance data were first generated by remote operation of the lcrplot program on a TRIUMF computer. Using lcrplot, text files containing the signal, signal error and magnetic field were created. The text files were transferred to an EXCEL template designed by Dr. Jean-Claude Brodovitch. The EXCEL template uses the solver function in EXCEL to fit μ-LCR resonances to differential Lorentzian shapes (difference between two Lorentzians) by performing a chi-square minimization. The fitting parameters are magnetic field position, amplitude and width of the resonance. The errors on the fitting parameters were generated using the limits option provided by the solver function in EXCEL.[89]

2.2. Gas hydrate preparation

Furan, 2,5-dihydrofuran, 2,3-dihydrofuran, acetone, isoxazole, cyclopentane and cyclopentene are all known to form structure II hydrates.[34] The organic liquids were obtained from Sigma-Aldrich. The freeze, pump, thaw method was used to remove oxygen from the liquids. Muonium is known to undergo spin exchange with oxygen's electrons so it is important to remove oxygen from the samples.[90] Both liquid and hydrate samples were prepared for comparison. The liquid cells were stainless steel cells with a thin stainless steel foil window (diameter of 25 mm) to permit passage of low momentum surface muons. The cells had a glass neck that could be flame sealed while keeping the cell frozen in liquid nitrogen and connected to vacuum.

Hydrates were prepared by mixing a 1:17 molar ratio of organic material to distilled water. Oxygen was removed by successive cycles of purging water with N_2 and evacuation. The water was then frozen by dripping into a cold bath of liquid nitrogen in a nitrogen bag. The ice was crushed into small pieces using a metal mortar and pestle. The organic liquids were added to the oxygen-free ice in the nitrogen bag and kept in vials. The vials were kept in a cooling bath below hydrate decomposition temperatures for a few days, and later in the freezer at -30°C.

Hydrate cells that were used for μSR at the beginning of this project were small cylindrical shape brass cells with a height of about 1.5 cm and an opening of 9 mm to fill the cells. The cap was a brass hollow hex plug of 1/8 inch NPT. The window was a thin foil with a diameter of 25 mm. This design is similar to the liquid cells frequently used in our group (designed by Dr. Brodovitch) when a small amount of liquid is available for μSR, and it worked fine for the liquid. However, it wasn't practical for the hydrates. They leaked at the back where they were closed, and the thin brass window cracked quite easily. The hydrate cells had to be kept cold in liquid nitrogen inside a nitrogen bag with a cold nitrogen stream flowing inside the bag. So there was a need of a cell with a longer height and wider opening so that it can be filled more conveniently. Also, working with thick gloves (to handle the cold) in the nitrogen bag doesn't give one a good grip to tighten the cap properly. So I thought of using a stainless steel Swagelok tube fitting, male connector, 3/4 inch tube OD x 3/4 inch male pipe weld[91] that can be welded to the

stainless steel small cylindrical shape cell. The cells were made by Jim Shoults in the SFU machine shop.[92] Figure 2.3 shows pictures of the cell. The cell length is 5.5 cm and the window diameter is 25 mm. After the cell was filled in the nitrogen bag, a stainless steel plug was used to close the cell. The plug was hand tightened in the bag and then the cell could be held in the vise on the lab bench outside the bag (while still cold) and the plug was tightened with a wrench. The sample cells were then packed in dry ice or kept in a MVE Cryoshipper dewar[93] to be carried to TRIUMF.

Benzene-xenon, thiophene-xenon, isobutene-xenon and pyrrole-methane hydrates were prepared using the pressure set-up in the lab. They are known to be double structure II hydrates, with benzene, thiophene, isobutene and pyrrole occupying the large cages and xenon or methane occupying the small cages.[94,95,96] Molar ratio of 1:17 for large guest (benzene, thiophene, isobutene) to water and 1:8.5 for small guest (xenon, methane) to water was used, assuming one guest occupies each cage. Figure 2.4 shows the pressure set-up in the lab for hydrate preparation. The procedure for making these hydrates is as follows:

First, powdered ice was loaded into the pre-cooled reactor in the nitrogen bag. Oxygen-free organic liquid was then added to the reactor. The reactor was taken outside the bag and held in a vise to tighten the bolts. Then it was attached to the pressure set-up through the open side of V1 valve (V1 was located on the reactor lid) and kept in a dry ice basket. The system was flushed with argon and evacuated a few times to make sure no oxygen was present. The secondary cell was attached to the system to measure the exact amount of gas needed for the sample. The Ideal Gas Law was used to calculate the pressure needed to provide the desired moles of the gas. If the moles of gas needed to make the hydrate was more than one fill of the secondary cell, the reactor was kept in liquid nitrogen to condense the gas in order to do the subsequent fills. The reactor was kept in dry ice for a few days, and later in the freezer at -30°C, until the pressure dropped significantly which is consistent with hydrate formation.

Figure 2.3: Side view (left) and front of the cell showing the window (right).

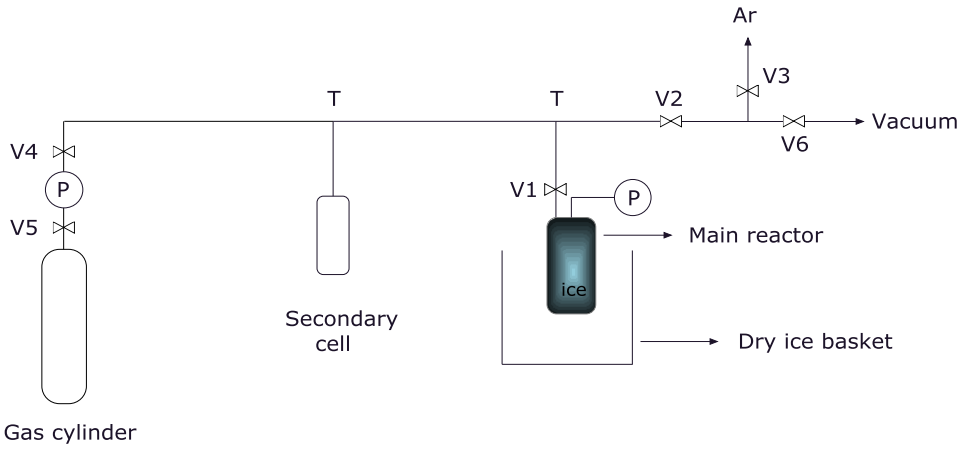

Figure 2.4: Pressure set-up for hydrate preparation.

2.3. Gas hydrate characterization

Powder X-ray diffraction (PXRD) and solid state NMR were used to characterize the hydrate samples. Jeffery Ovens and Didier Savard helped me to collect data with the single-crystal instrument in Dr. Leznoff's Laboratory in the SFU Chemistry Department. This was the only X-ray diffraction instrument at SFU with a cryoprobe attachment that used liquid nitrogen to cool the sample. This instrument was used because the samples had to be kept cold to be stable.

Dr. John Ripmeester from National Research Council Canada in Ottawa gave advice on how to perform NMR on hydrates and also provided the xenon-β-

hydroquinone clathrate (stable at room temperature) which was used to find NMR optimum conditions for hydrates. Dr. Andrew Lewis from SFU NMR Facility helped with collecting all the NMR spectra.

2.3.1. PXRD of hydrates

Powder X-ray diffraction has been used traditionally for qualitative identification of polymorph phases. In order to get a diffraction pattern the Bragg condition should be satisfied: $n\lambda = 2d\sin\theta$, where λ is the wavelength of the X-ray radiation, d is the particular spacing between individual parallel planes and θ is the angle between the incident radiation and the set of planes. If the path difference between the incident and reflected beams is an integer number of wavelength, the Bragg condition is fulfilled. The X-ray powder diffraction pattern is a plot of diffraction intensity versus 2θ values and may be considered a fingerprint of the solid. The intensities are dependent upon the contents of the unit cell, and the 2θ values (or d spacings) show the dimensions of the unit cell.[97]

The instrument at SFU is a Bruker SMART ApexII Duo CCD diffractometer with a Cu Kα (λ = 1.54184 Å) radiation source using ω and ϕ scans for powder data collection. The instrument has a cryoprobe attachment that uses liquid nitrogen to cool the sample. Hydrate PXRD spectra mostly were taken at -173°C. Only the spectra of furan and 2,5-dihydrofuran hydrates were taken at -124°C and these spectra were taken from the samples before and after the experiments at TRIUMF. Figure 2.5 shows the spectrum of THF (tetrahydrofuran) hydrate, taken at SFU after it was exposed to the muon beam at TRIUMF. The black line shows the sample and the blue line shows the reference.[98] The sample may contain a small amount of ice. The intensity of the sample was scaled to be comparable with the reference. Figures 2.6-2.9 show the PXRD spectra of furan hydrate, furan hydrate after TRIUMF, 2,5-dihydrofuran hydrate, 2,5-dihydrofuran hydrate after TRIUMF respectively. The PXRD spectra of acetone and isoxazole hydrates are in Appendix A.

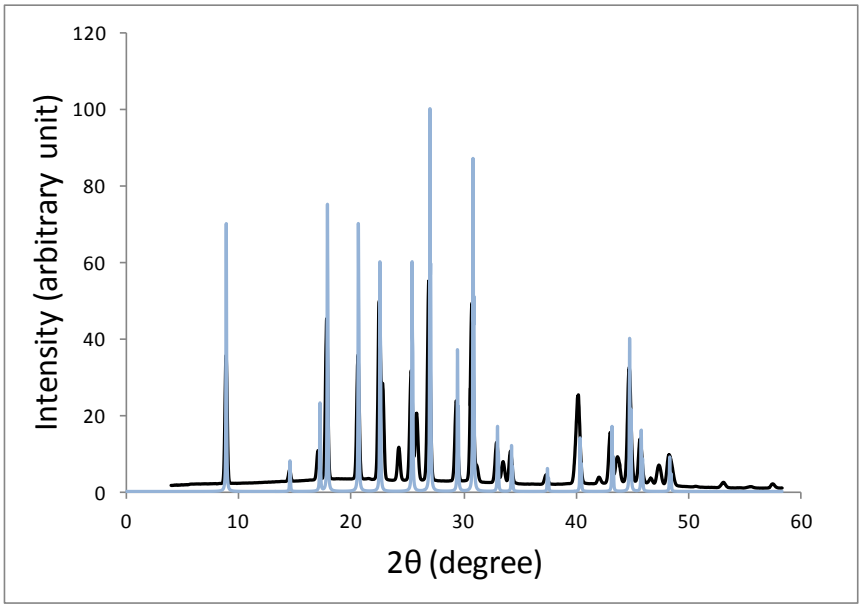

Figure 2.5: PXRD spectra of THF hydrate after it was exposed to the beam at TRIUMF (black line) compared to the literature data on THF hydrate[98] (blue line). The sample may contain a small amount of ice.

The result showed the 2θ positions were the same but the peak intensities varied. This is because all hydrates that were characterized with PXRD are structure II so they have similar 2θ values. The hydrate samples were ground to a fine powder in a mortar and pestle while kept cold in liquid nitrogen. This grinding action could have affected the peak intensities.[97] Also, the spectra show that there was no damage to the sample after it had been exposed to the muon beam at TRIUMF.

PXRD is a useful technique to characterize hydrates. In this work all the spectra show that the hydrates have structure II as expected.

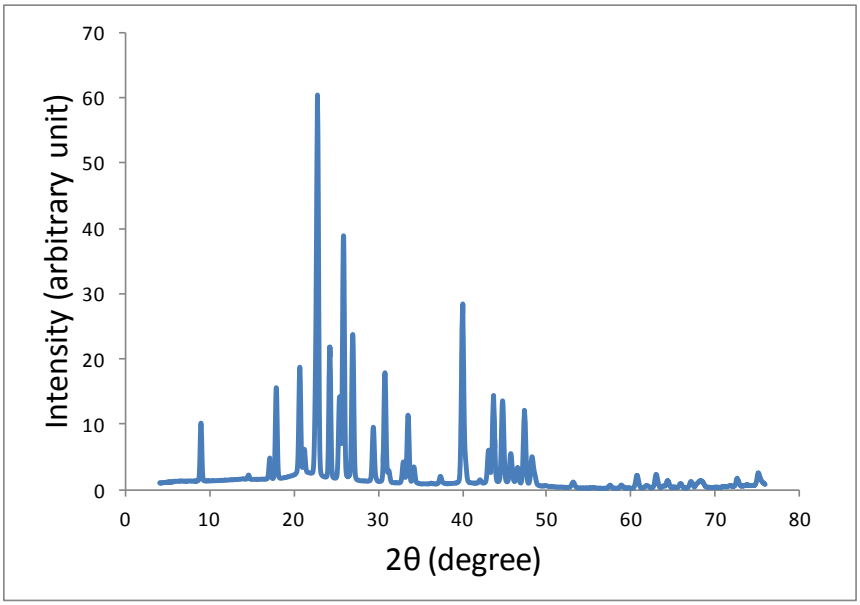

Figure 2.6: PXRD spectrum of furan hydrate

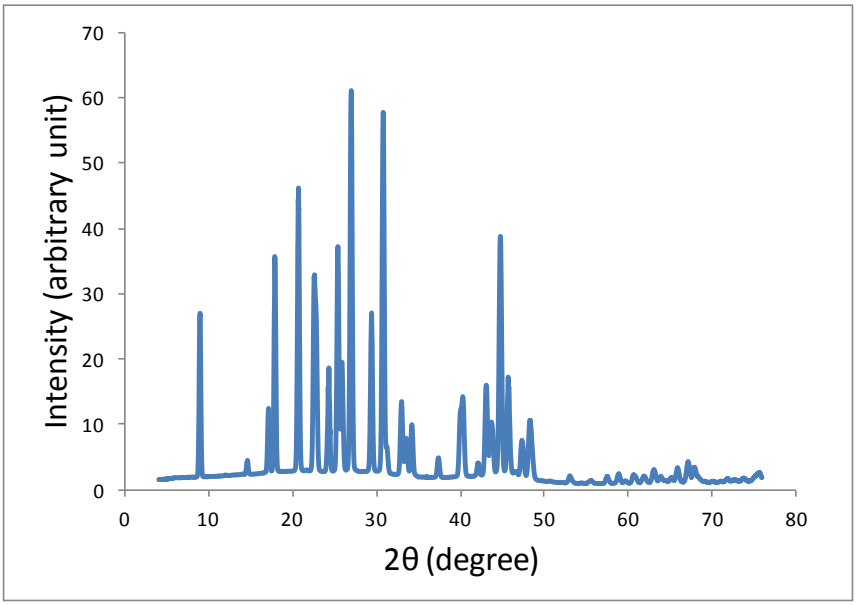

Figure 2.7: PXRD spectrum of furan hydrate after it was exposed to the beam at TRIUMF

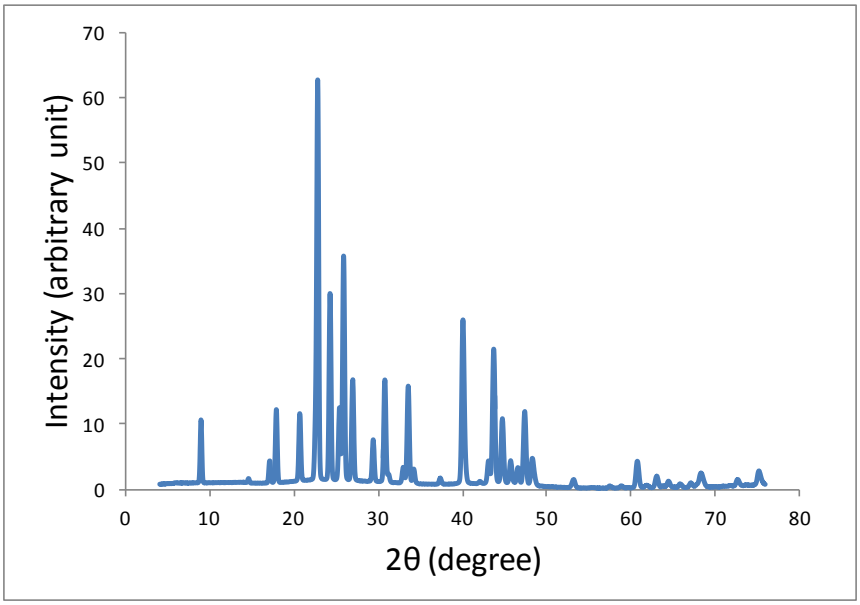

Figure 2.8: PXRD spectrum of 2,5-dihydrofuran hydrate

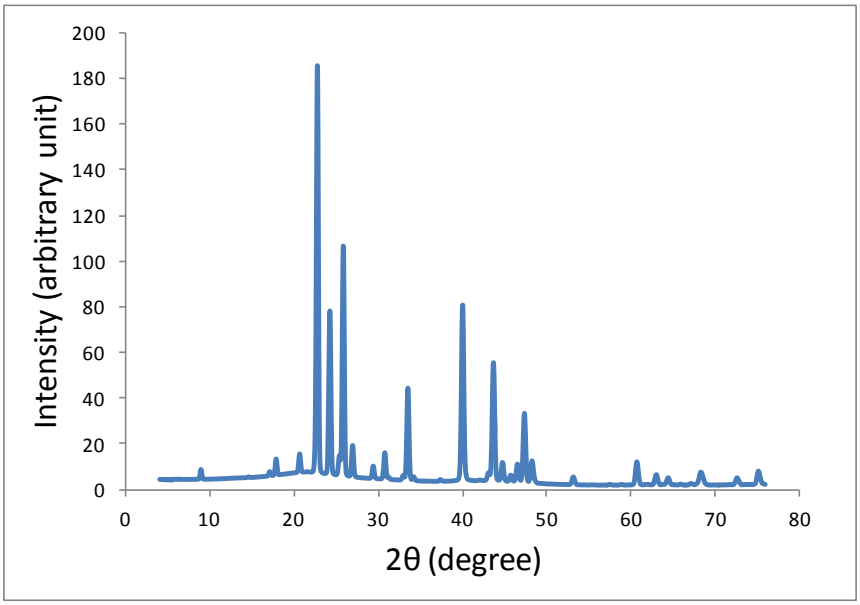

Figure 2.9: PXRD spectrum of 2,5-dihydrofuran hydrate after it was exposed to the beam at TRIUMF

2.3.2. NMR of hydrates

^{129}Xe NMR has been used to distinguish void spaces in solids. The isotropic chemical shift of the trapped xenon atoms is sensitive to the void size and the anisotropic shift is an indication of the void symmetry.[99,100] In this work, isotropic chemical shifts of xenon atoms trapped in hydrate cages were used to characterize the hydrate samples. Benzene-xenon, thiophene-xenon and isobutene-xenon hydrates that were characterized by ^{129}Xe NMR are all structure II hydrates. The resonances for ^{129}Xe trapped in the small (5^{12}) cages and large ($5^{12}6^4$) cages appear at ~220-240 ppm and ~80 ppm respectively. The exact chemical shifts depend on the temperature, and minor shift differences occur for the same resonance in different samples.[94]

To observe the signal of ^{129}Xe gas for the first time, I prepared a sample of about 5 atm xenon gas adsorbed on Linde 13X zeolite in a heavy walled J. Young tubing from Wilmad-LabGlass[101] company. A few miligrams of the zeolite was crushed in a mortar and pestle to become a fine powder. The powder was dehydrated in a vacuum oven for two days at 250°C and kept under argon. Then I transferred the powder to the J. Young tubing, put a piece of cotton at the inlet (to avoid loss of powder to vacuum) and closed the cap. The tube was then connected to the vacuum/pressure system to condense xenon in the tube. Figure 2.10 shows the ^{129}Xe NMR spectrum at room temperature. The xenon adsorbed on zeolite appears at 177 ppm and the excess xenon gas at 0 ppm.[99] The spectrum was taken using the Bruker AVANCE III 400 MHz spectrometer with 120 scans and recycle delay of 4 s. The experiment took 8 minutes.

In order to know the NMR parameters (duration of pulses, contact times, spinning frequencies, etc.) required for collecting the hydrate spectra and also as a reference standard, it was necessary to acquire xenon-β-hydroquinone clathrate spectrum first.[99] Dr. Ripmeester provided this sample. This clathrate is made of benzene-1,4-diol (hydroquinone) molecules that are connected through hydrogen bonding. Xenon atoms are trapped in cavities with about 4.8 Å diameter. Cage walls are made of six C_6H_4 moieties and the top and bottom ends of the cages are two hydrogen bonded $[OH]_6$ hexagonal rings.[102] This organic clathrate is stable at room temperature and it has only one type of cage. The formula is $3C_6H_4(OH)_2.xG$ where G is the enclathrated guest

molecule (xenon in this case) and *x* is the site-occupancy factor of the guest, which is one ideally (1 guest molecule per 3 hydroquinone molecules).[103]

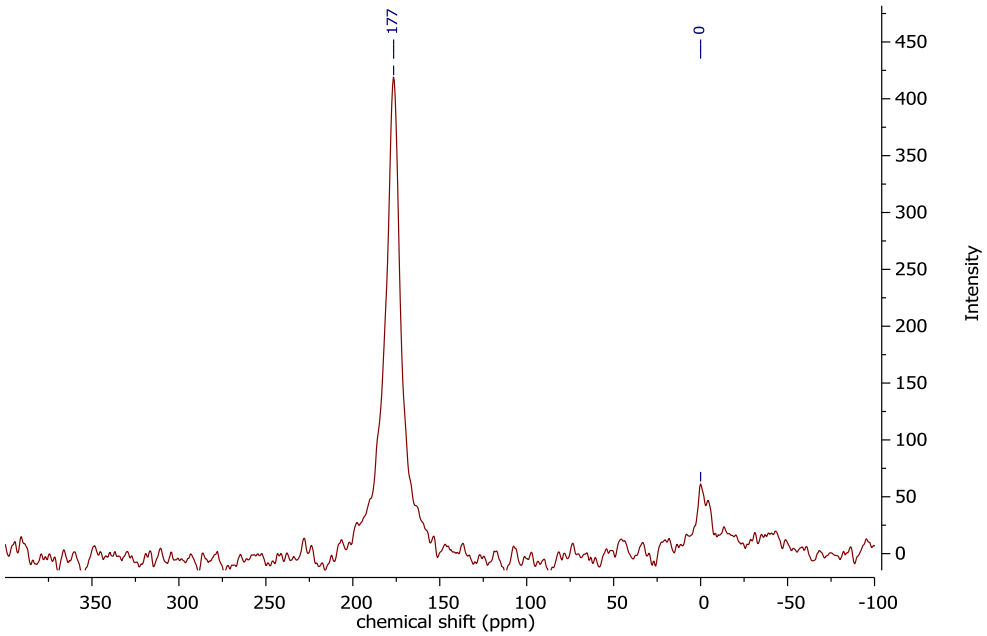

Figure 2.10: ^{129}Xe NMR spectrum of 5 atm of xenon gas adsorbed on Linde 13X zeolite at 300 K. Xenon gas signal set to 0 ppm.

The Bruker AVANCE III 400 MHz spectrometer for solids was used to collect the spectra for xenon-β-hydroquinone, benzene-xenon, thiophene-xenon and isobutene-xenon clathrates. All the NMR experiments of the hydrates were performed by using the 7 mm MAS probe. Figure 2.11 shows the spectrum of xenon-β-hydroquinone clathrate at 243 K. The peak at 219 ppm (referenced to dilute xenon gas at zero) is the main resonance and the rest of the peaks marked with * are spinning side bands. The spectrum was obtained by using ^{129}Xe-^{1}H cross polarization, ^{1}H decoupling and magic angle spinning (MAS) of 5 kHz. The NMR acquisition parameters were ^{1}H 90° pulse of 3.5 μs, ^{129}Xe 90° pulse of 4.6 μs, 5.5 μs for decoupling, contact time of 10 ms, recycle delay of 10 s and 16 scans. The experiment took 2.5 minutes.

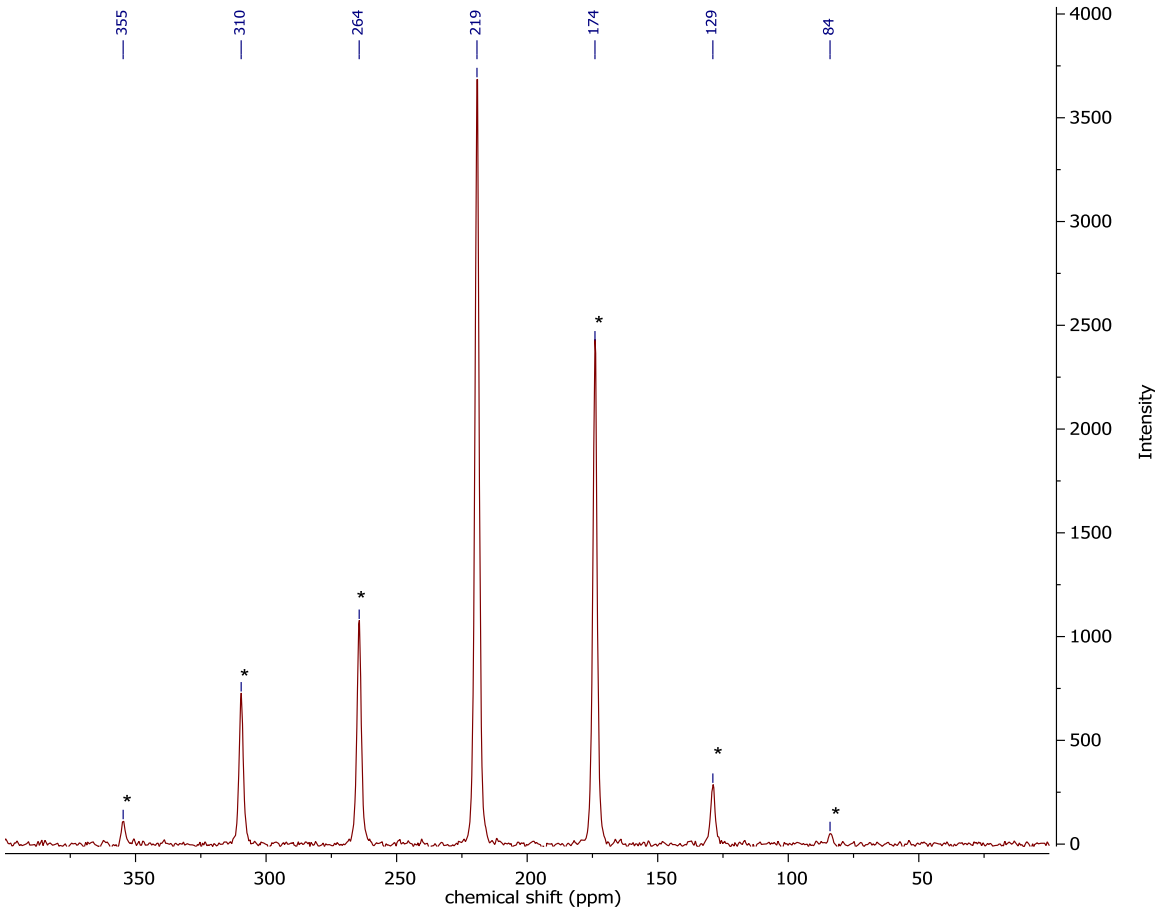

Figure 2.11: ^{129}Xe NMR spectrum of xenon trapped in xenon-β-hydroquinone clathrate at 243 K. Peaks marked with * are spinning side bands.

Figure 2.12 shows the spectrum of benzene-xenon clathrate at 233 K. The most intense peak at 229 ppm is due to xenon in the small cages of structure II hydrate. The peak at 90 ppm is due to xenon in the large cages of structure II hydrate. Peaks at 150 and 243 ppm represent xenon in the large and small cages of structure I xenon hydrate respectively.[104] The residue of structure I xenon hydrate is because ice and xenon make structure I xenon hydrate first and if there is another guest material such as benzene molecule also available, structure I xenon hydrate will react with the guest to form benzene-xenon structure II double hydrate. This reaction takes place only if the double hydrate is more stable than the structure I xenon hydrate.[94]

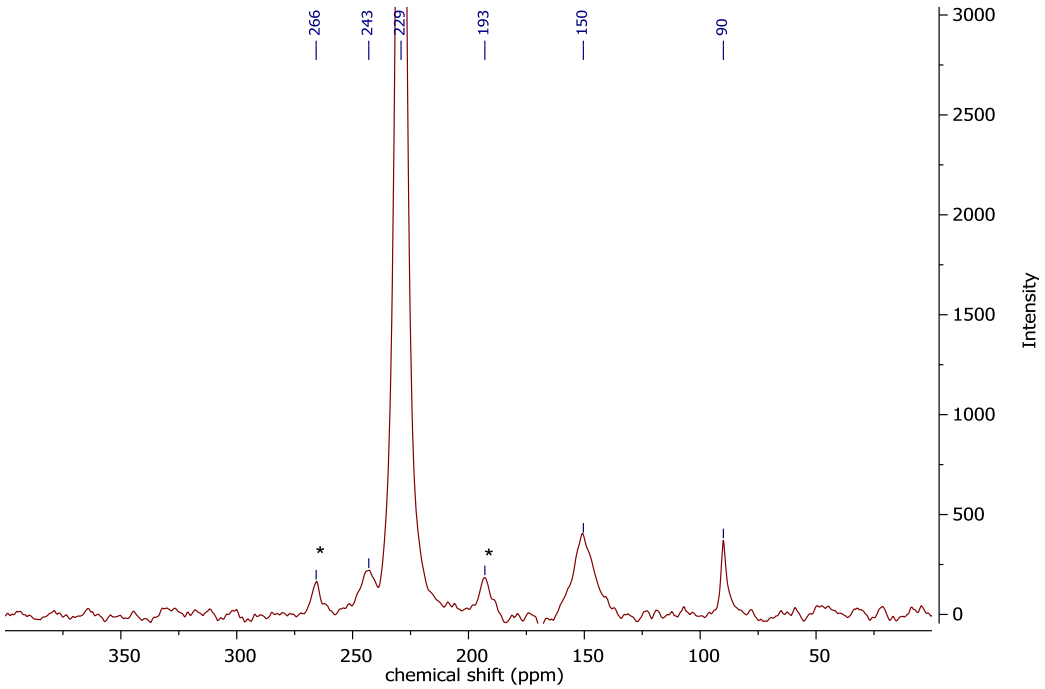

Figure 2.12: ^{129}Xe NMR spectrum of benzene-xenon hydrate at 233 K. Peaks marked with * are spinning side bands.

The spectrum was obtained by using ^{129}Xe-^{1}H cross polarization, ^{1}H decoupling and magic angle spinning (MAS) of 4 kHz. The NMR acquisition parameters were ^{1}H 90° pulse of 3.5 μs, ^{129}Xe 90° pulse of 4.6 μs, 5.5 μs for decoupling, contact time of 2 ms, recycle delay of 1 s and 1000 scans. The experiment took 17.5 minutes.

Figure 2.13 shows the superimposed spectra of isobutene-xenon clathrate with rotation of 5 kHz and 4 kHz at 233 K. The peaks at 91 and 232 ppm are due to xenon in large and small cages of structure II hydrate. The rest of the peaks marked with * and + signs are due to the spinning side bands for the magic angle spinning of 5 kHz and 4 kHz respectively. Both spectra were collected by using ^{129}Xe-^{1}H cross polarization and ^{1}H decoupling. The NMR acquisition parameters were ^{1}H 90° pulse of 3.5 μs, ^{129}Xe 90° pulse of 4.6 μs, 5.5 μs for decoupling, contact time of 2 ms and recycle delay of 1 s. For the 5 kHz rotation, 1000 scans were taken and the experiment took 17.5 minutes. However, the experiment for 4 kHz rotation only took 2 minutes with 100 scans. The latter was done to check for the spinning side bands.

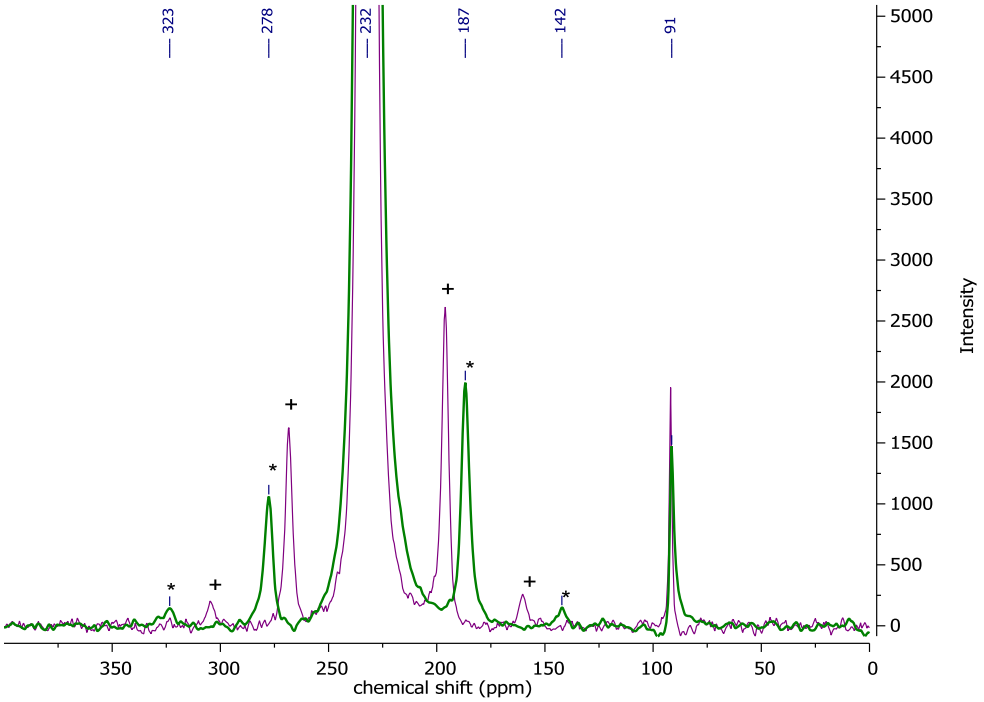

Figure 2.13: ^{129}Xe NMR spectrum of isobutene-xenon hydrate with rotation of 5000 Hz (green) and 4000 Hz (purple) and their spinning side bands are marked with * and + signs respectively.

Figure 2.14 shows the spectrum of thiophene-xenon clathrate at 233 K. The peaks at 92 and 234 ppm are due to xenon in large and small cages of structure II hydrate. The very small peak at 92 ppm shows almost all xenon atoms are trapped in small cages. The spectrum was obtained by using ^{129}Xe-^{1}H cross polarization, ^{1}H decoupling and magic angle spinning (MAS) of 5 kHz. The NMR acquisition parameters were ^{1}H 90° pulse of 3.5 μs, ^{129}Xe 90° pulse of 4.6 μs, 5.5 μs for decoupling, contact time of 2 ms, recycle delay of 1 s and 1000 scans. The experiment took 17.5 minutes.

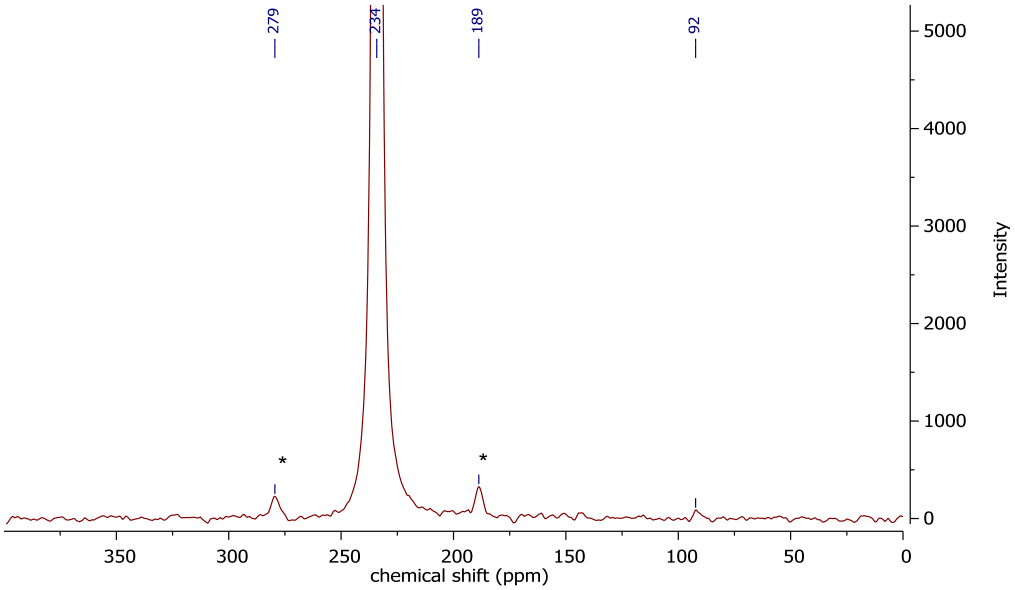

Figure 2.14: ^{129}Xe NMR spectrum of thiophene-xenon hydrate at 233 K. Peaks marked with * are spinning side bands.

The resonances appear at places that are expected from literature data in all samples, confirming the type of the hydrates made. So ^{129}Xe NMR is a valuable tool to characterize hydrates that contain xenon gas.

^{13}C NMR of pyrrole-methane hydrate is shown in Figure 2.15. The spectrum was obtained at 220 K with cross polarization, ^{1}H decoupling and magic angle spinning (MAS) of 1 kHz. The NMR acquisition parameters were 90° pulse of 5.3 µs, contact time of 6 ms, recycle delay of 10 s and 250 scans. Adamantane was used as an external reference.[105,106] The peaks at -4 and -8 ppm are due to methane in small and large cages of the structure II pyrrole-methane hydrate.[107,108] The peaks of pyrrole appear at 107 and 117 ppm.[109] The signals are small because the sample wasn't ^{13}C-enriched.

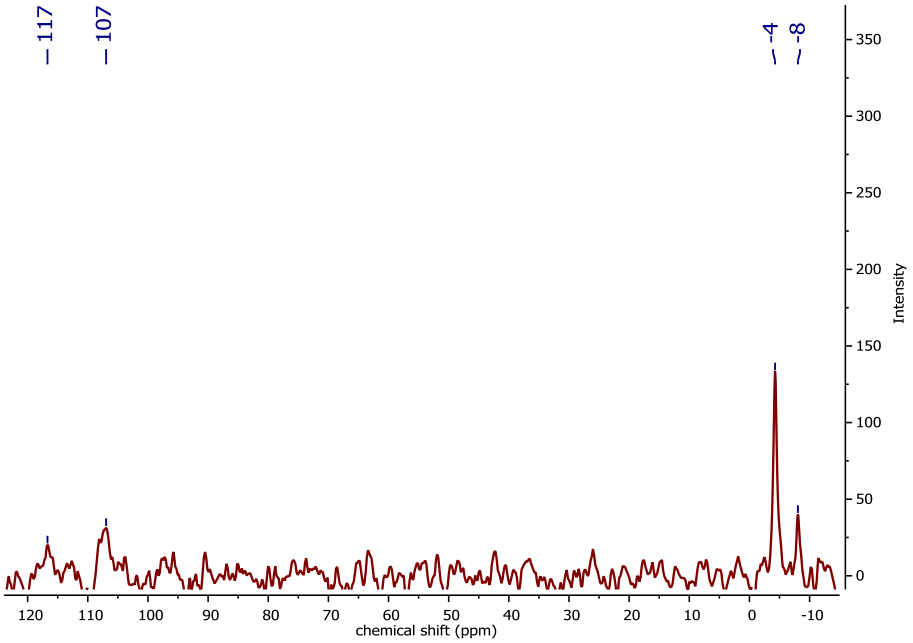

Figure 2.15: ^{13}C NMR spectrum of pyrrole-methane hydrate at 220 K.

2.4. Density functional theory method

In order to compare experimental results of hyperfine coupling constants with theoretical results and to get the optimized geometries of the muoniated free radicals, density functional theory (DFT) calculations were used. The DFT method has been widely used for modeling of chemical systems.[110] It is based on the Schrödinger equation.[111] The time-independent, non-relativistic Schrödinger equation is:

$$\hat{H}\Psi = E\Psi \tag{2.3}$$

where $\hat{H}$ is the Hamiltonian of the system, E is the total energy and Ψ is the N-particle wavefunction. Within the Born–Oppenheimer approximation, the Hamiltonian is as follows:

$$\hat{H} = \hat{T}_{\mathrm{e}} + \hat{V}_{\mathrm{ee}} + \hat{V}_{\mathrm{ne}} + \hat{V}_{\mathrm{nn}} \tag{2.4}$$

where $\hat{T}_e, \hat{V}_{ee}, \hat{V}_{ne}, \hat{V}_{nn}$ are the kinetic energy, electron-electron repulsion, electron–nucleus attraction, and nucleus–nucleus repulsion operators, respectively. The

fundamental principles of most ab initio methods are based on the Hartree–Fock (HF) approximation which uses the Slater determinant of one-electron wavefunctions, ψ_i, to define Ψ. The HF equation is:

$$\left(-\frac{1}{2}\nabla^2 + v_{\text{eff},i}^{\text{HF}}(r)\right)\psi_i(r) = \varepsilon_i\psi_i(r) \tag{2.5}$$

where ∇^2 is the Laplacian operator, ε_i is the eigenvalue of electron *i*, and $v_{\text{eff},i}^{\text{HF}}$ is the effective HF operator:

$$v_{\text{eff},i}^{\text{HF}}(r) = v_{\text{ext}}(r) + v_{\text{H}}(r) + v_{\text{X},i}^{\text{HF}}(r) \tag{2.6}$$

v_{ext}, v_{H} and $v_{\text{X},i}^{\text{HF}}$ are the external, Hartree and non-local exchange potentials respectively. The HF approximation doesn't account for the electron correlation and assumes that each electron interacts with the average potential generated by the other electrons. To take this correlation into account, it is necessary to consider post-HF methods but these models are computationally expensive. DFT is an alternative that includes the correlation without using the wavefunction method. It is based on the electron density function, ρ and calculates all the properties of atoms and molecules from the electron density. According to Hohenberg and Kohn any property of a molecule in a ground electronic state is determined by the ground state electron density function. However, they didn't provide the exact ground state functional form.[112] To solve this problem, Kohn and Sham introduced equations (Kohn-Sham equations) which are similar to HF equations, except that the effective potential has an expression that includes an additional exchange-correlation potential:[113]

$$\left(-\frac{1}{2}\nabla^2 + v_{\text{eff}}^{\text{KS}}(r)\right)\psi_i(r) = \varepsilon_i\psi_i(r) \tag{2.7}$$

$$v_{\text{eff}}^{\text{KS}}(r) = v_{\text{ext}}(r) + v_{\text{H}}(r) + v_{\text{XC}}^{\text{KS}}(r) \tag{2.8}$$

v_{ext}, v_H and v_{XC}^{KS} are the external, Hartree and exchange-correlation potentials respectively. The exchange-correlation potential is defined as the functional derivative of the exchange-correlation energy, E_{XC} with respect to $\rho(r)$:

$$v_{XC}(r) = \frac{\partial E_{XC}[\rho(r)]}{\partial \rho(r)} \tag{2.9}$$

and the electron density of the system is given by:

$$\rho(r) = \sum_{i=1}^{N} |\psi_i(r)|^2 \tag{2.10}$$

The form of the exchange-correlation energy functional is unknown and various approximations are used for it, such as hybrid functionals. The most popular hybrid functional is known as the B3LYP functional which has been used in many chemical applications.[114]

A set of mathematical functions or basis functions are used as approximations for describing molecular orbitals. Linear combination of atomic orbitals (LCAO) is an approach that uses atomic orbitals as basis sets to represent molecular orbitals:

$$\psi_i = \sum_{s=1}^{m} c_{si}\phi_s \tag{2.11}$$

where $i = 1, 2, 3, ..., m$ is the number of molecular orbitals, ϕ_s is the *s*th basis function, *c* is the coefficient of the *s*th basis function of the *i*th molecular orbital.[111] Basis functions (contracted functions) are composed of a linear combination of Gaussian functions (primitives). In this study, the B3LYP functional with 6-31G(d) basis set was used. 6-31G(d) is a split valence basis set which has six Gaussian functions for the inner shell atomic orbitals, two sizes of basis functions for the valence atomic orbitals (three and one Gaussian functions) and a d function for the polarization (to allow the orbitals to change shapes). In some calculations, the EPR-II basis set was used which is optimized for the computation of hyperfine coupling constants by DFT methods.[115,116]

The isotropic hfc or the Fermi contact interaction was calculated in this work. The isotropic hfc is directly proportional to the unpaired spin density at the nucleus, $\left|\psi_{(0)}\right|^2$, and the nuclear gyromagnetic ratio. The hfc (in MHz) is given by:[1]

$$A_x = \frac{2\mu_0}{3h} g_e \beta_e g_x \beta_x \left|\psi_{(0)}\right|^2 \tag{2.12}$$

where g_e is the free electron g factor, β_e is the Bohr magneton, g_x is the nuclear g factor, and β_x is the nuclear magneton. The anisotropic part of the hyperfine interaction comes from a direct dipolar interaction between the electron and nuclear magnetic moments. The dipolar energy is proportional to a $\frac{1-3\cos^2\theta}{r^3}$ term where r is the electron-nucleus distance. Averaging over the spherical distribution of an electron in an s-orbital gives zero dipolar energy. Taking an orientational average to obtain the mean interaction energy for rapidly tumbling molecules in solution also leads to zero dipolar energy.[117]

The origin of the isotope effect comes from anharmonicity in the potential for vibrational energies. Mu has a larger zero-point energy than H which leads to the C-Mu bond being longer than the C-H bond by 4.9% and the hyperfine coupling constants become positive with increasing bond length.[118]

Muonium was considered as a light isotope of H with mass 0.113429 u and magnetic moment of 8.890597 μ_N.[119,120] The hyperfine coupling constants and equilibrium geometry do not change with isotope substitution except that the magnetic moment of the muon is 3.183345 times larger than the proton.[16] However, vibrational averaging affects both the geometry and the hyperfine coupling constants. The keyword Freq=Anharmonic was used so that in addition to the equilibrium geometry, the anharmonic vibrationally averaged structure at 0 K and other specified temperatures were generated.[121] The keyword Fermi was used to perform vibrational averaging of isotropic hyperfine coupling constants.

2.4.1. Software package used

All calculations were performed using the Gaussian 09 package and Westgrid Computing Facilities.[122,123]

Chapter 3.

Organic free radicals of cyclopentene and 2,5-dihydrofuran in clathrate hydrates investigated by muon spin spectroscopy

3.1. Introduction

The contents of this chapter have been published in the Journal of Physical Chemistry A, 2014, 118, 1162−1167.[17]

Clathrate hydrates of cyclopentene, 2,5-dihydrofuran and their saturated forms, cyclopentane and tetrahydrofuran were prepared as mentioned in section 2.2. The hydrates were irradiated with muons at TRIUMF, and the muoniated products were investigated by muon spin rotation and muon avoided level-crossing spectroscopy for the first time. There is little known about the chemistry of radicals in gas hydrates. Until recently, the literature on clathrate hydrates was almost exclusively concerned with structures, thermodynamic properties, and other data of geophysical and engineering relevance. Studies of chemical reactivity are rare; notable exceptions are the series of papers by Ohgaki et al. who used ESR to study radicals in γ-irradiated hydrates.[124,70,125,72,126] The ESR detection of H atoms at low temperature in γ- irradiated H_2 hydrates and the work of Bini et al. who employed two-photon irradiation to induce radical reactions in gas hydrates.[127,128,129]

Molecular geometries and hyperfine coupling constants of muoniated free radicals were calculated using the B3LYP hybrid functional and 6-31G(d,p) basis set. Optimized geometries of muoniated cyclopentyl and hydrofuranyl radicals (supporting information data) are in Appendix B.

3.2. Results and discussion

Transverse-field μSR experiments revealed characteristic spin precession signals of muonium from hydrate samples of cyclopentane and tetrahydrofuran. At an applied magnetic field of 6.8 G a single Mu frequency was evident at 9.5 MHz, consistent with the near degeneracy of ω_{12} and ω_{23} (eqs. 1.11 and 1.12, $\omega = 2\pi\nu$). At higher fields the expected splitting of the precession frequencies is clear, as shown in Figure 3.1, and this was used to estimate the isotropic hyperfine frequency: 4480 ± 20 MHz for Mu in cyclopentane hydrate, and 4400 ± 10 MHz for Mu in tetrahydrofuran hydrate. These values are very close to the vacuum value (4463 MHz), indicating unbound atoms, and very similar to what has been determined for Mu in ice-Ih (4510 ± 50 MHz)[130] and in liquid water over a wide range of density (4410-4470 MHz).[131] The polycrystalline nature of the hydrate samples precluded a detailed study of hyperfine anisotropy, such as that carried out for single-crystal ice.[132] However the narrow "powder-pattern" line-shapes show that any anisotropy must be small (≤ 1 MHz).[133]

Clear μSR signals of muoniated radicals were detected from the hydrates containing unsaturated guest molecules. Examples of the spectra are shown in Figure 3.2. The large, truncated peak is due to muons incorporated in diamagnetic molecules, whereas the pair roughly equally placed about the diamagnetic signal is characteristic of a muoniated radical, as described by eq. (1.18).

Pure liquid samples of cyclopentene and 2,5-dihydrofuran were studied at the same temperature for comparison with the hydrates. Muon hyperfine constants were determined from the separation of each pair of radical precession signals and are compiled in Table 3.1. The results show a clear difference between radicals in the liquid phase and in the clathrate, and in both environments the hyperfine constant decreases with temperature. This is an expected behavior which was seen for other alkyl radicals in the past where C-Mu bond prefers an eclipsed conformation with the p-orbital containing the unpaired electron at low temperature and it rotates as the temperature is raised.[134,8] There is little doubt that the radicals detected are the cyclopentyl radical and the analogous hydrofuranyl radical, as indicated in Scheme 3.1. Our results for the

muoniated cyclopentyl radical in liquid cyclopentene are in excellent agreement with the literature value (374.7 MHz at 274 K).[134]

Table 3.1: Muon hyperfine constants determined from transverse-field μSR spectra

Sample and conditions	Muon hyperfine constant /MHz
cyclopentene liquid, –10°C, 2.0 kG	376.30 ± 0.13
cyclopentene liquid, +10°C, 2.0 kG	373.64 ± 0.13
cyclopentene hydrate, –10°C, 11.6 kG	380.75 ± 0.14
2,5-dihydrofuran liquid, –10°C, 2.0 kG	367.28 ± 0.04
2,5-dihydrofuran hydrate, –12°C, 14.5 kG	365.99 ± 0.05
2,5-dihydrofuran hydrate, –12°C, 11.6 kG	365.98 ± 0.05
2,5-dihydrofuran hydrate, –3°C, 11.6 kG	365.09 ± 0.04

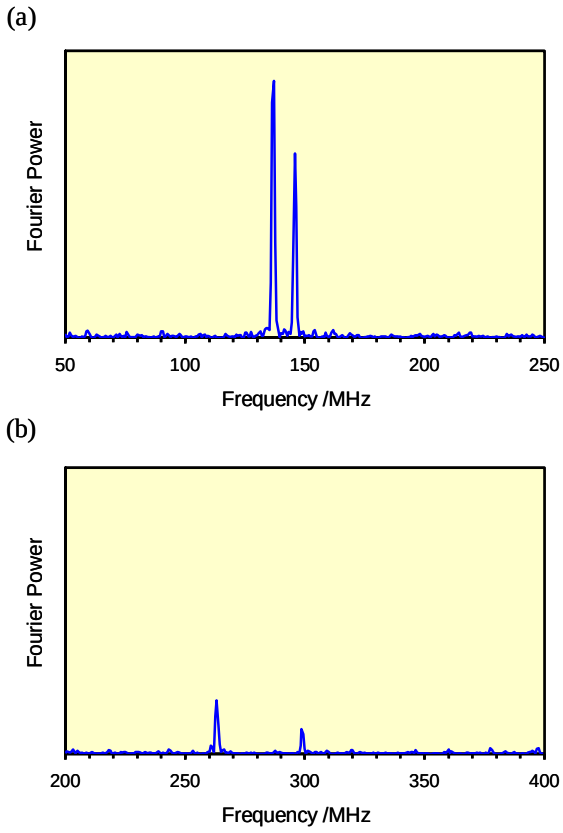

Figure 3.1: **Fourier power μSR spectra displaying the precession frequencies of muonium in cyclopentane hydrate at -10°C, in transverse magnetic fields of (a) 100 G (frequencies 136.6 MHz and 145.7 MHz); (b) 200 G (frequencies 263.1 MHz and 298.9 MHz). In both cases the diamagnetic signal at the muon Larmor frequency is off-scale below the lower bound of the x-axis. The y-axis scales are the same in the two spectra. Adapted with permission.[22] Copyright 2014, American Chemical Society.**

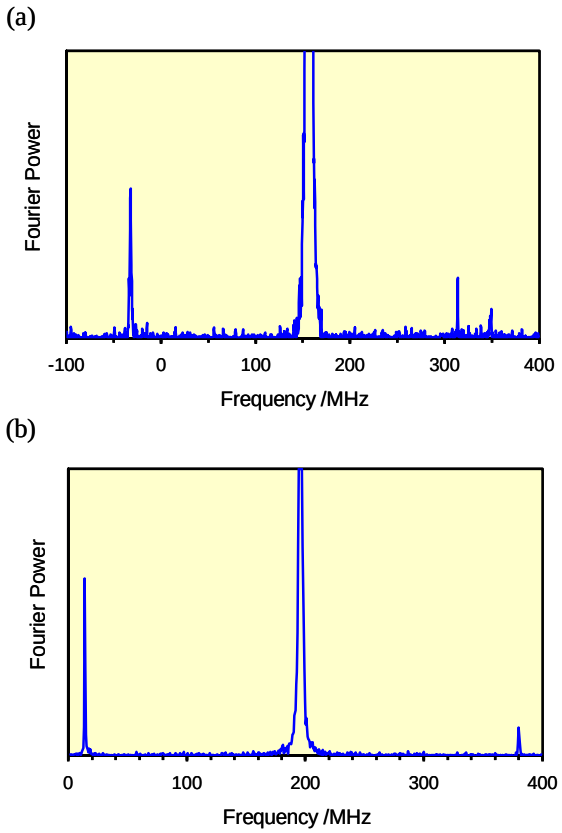

Figure 3.2: **Fourier power μSR spectra obtained from (a) cyclopentene hydrate at -10°C, in a transverse magnetic field of 11.57 kG; (b) 2,5-dihydrofuran hydrate at -12°C, in a transverse magnetic field of 14.46 kG. The peaks at (a) -32.3 MHz and 348.3 MHz; and (b) 14.0 MHz and 365.8 MHz are due to muoniated free radicals. The sharp signal at 314 MHz in (a) is an artifact corresponding to the overtone of the strong diamagnetic signal at 157 MHz. Adapted with permission.[22] Copyright 2014, American Chemical Society.**

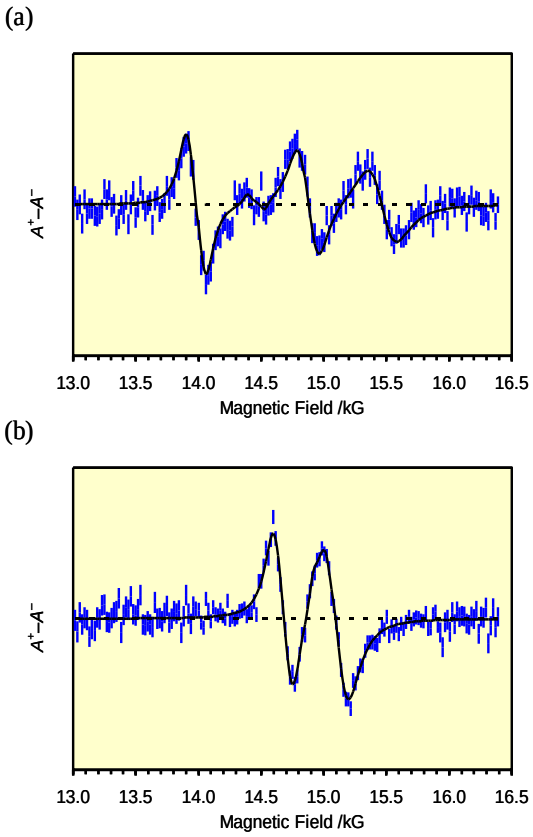

Figure 3.3: **Comparison of muon avoided level-crossing spectra obtained from (a) cyclopentene hydrate at -10°C; (b) pure liquid cyclopentene at -10°C. The α-H resonance occurs at higher field. Adapted with permission.[22] Copyright 2014, American Chemical Society.**

Scheme 3.1: **Muonium addition to cyclopentene and 2,5-dihydrofuran**

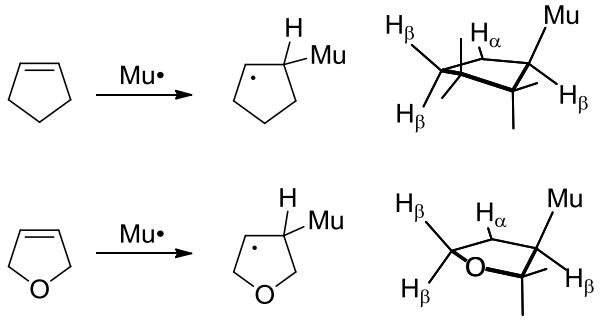

We have also examined the muoniated radicals by μ-LCR spectroscopy. Rapidly tumbling radicals exhibit ΔM=0 resonances due to muon-proton "flip-flop" spin mixing.[26] Three resonances were expected for each of these radicals, corresponding to the differing hyperfine constants of inequivalent protons: the α-H at the radical centre, the two β-H of the neighbouring CH_2, and the β-H of the CHMu on the other side of the radical centre. These signals were all observed for the muoniated radicals in liquid samples. However, an extra resonance was detected in the case of enclathrated radicals, as shown in Figure 3.3 for muoniated cyclopentyl.

The extra signal is consistent with a ΔM = 1 resonance, which occurs at the avoided crossing of energy levels corresponding to opposite muon spin orientations. Its position depends only on the muon hyperfine constant, and from eq. (1.24) we deduce that A_μ = 380.9 ± 0.1 MHz, in agreement with the value determined from transverse-field μSR. Similarly, the lowest-field μ-LCR signal detected for the hydrofuranyl (Figure 3.4) is also consistent with a ΔM=1 resonance, and yields A_μ = 366.0 ± 0.1 MHz for that radical, again in good agreement with the value determined from transverse-field μSR. Such ΔM = 1 resonances are observed only when there is significant anisotropy in the hyperfine interaction.[26] The implication here is that the cyclopentyl and hydrofuranyl radicals detected in clathrate hydrates are not freely tumbling.

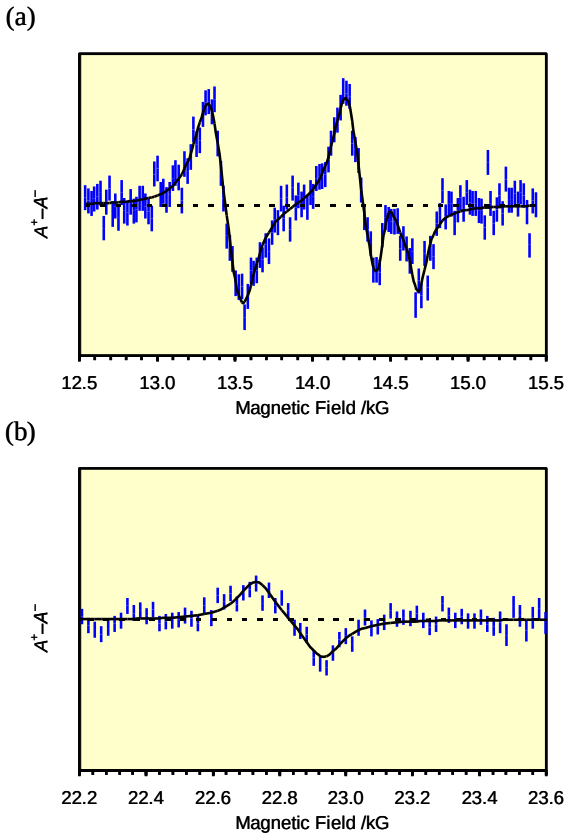

Figure 3.4: Muon avoided level-crossing spectrum due to muoniated radicals in 2,5-dihydrofuran hydrate at -12°C. (a) The ΔM=1 resonance and the overlapping ΔM=0 resonances for β-H; (b) the α-H resonance. Adapted with permission.[22] Copyright 2014, American Chemical Society.

The remaining μ-LCR signals were assigned to ΔM=0 resonances and the field positions were converted to hyperfine constants using eq. (1.23). The results are listed in Tables 3.2 and 3.3. Because α-protons have negative hyperfine constants, their resonances are well separated from those due to β-protons, as shown in Figure 3.4. In each radical there are three β protons to be assigned, one from the CHMu group and two from CH_2. It is tempting to assign the two β resonances to these two groups but, as pointed out by Roduner and Reid, the latter pair are not equivalent, one H taking a more axial conformation than the other.[134] Because Mu is known to take the axial conformation in CHMu groups we assign the lower-field resonance of Figure 3.3(b) to the axial proton

in CH_2 and the broader resonance to the equatorial CHMu and CH_2 protons. The spectrum of the same radical in cyclopentene hydrate was assigned in similar manner, except for the additional $\Delta M = 1$ resonance. It is interesting to note that the difference between hyperfine constants for axial and equatorial H atoms varies between muoniated cyclopentyl in the liquid state and the hydrate, and for the hydrofuranyl, perhaps indicating differences in the degree of vibrational averaging of the conformers. One possibility is that the weighting of the conformers is affected by the weak interactions of the radical with the hydrate lattice.

Table 3.2: Muon and proton hyperfine constants determined from the μ-LCR spectrum of the muoniated cyclopentyl radical at -10°C, in liquid cyclopentene and in cyclopentene hydrate

sample	B_{LCR} /kG[a]	ΔM	hfc /MHz[b]	assignment
liquid	14.677	0	101.8	proton, axial β-H in CH_2
"	15.093	0	94.1	2 × proton, equatorial β-H
"	23.360	0	-59.1	proton, α-H
hydrate	13.982	1	380.9	muon in CHMu
"	14.875	0	102.6	proton, axial β-H in CH_2
"	15.467	0	91.6	2 × proton, equatorial β-H
"	23.632	0	-59.7[c]	proton, α-H

[a] Resonance field. [b] Except where noted, the uncertainty in hyperfine constants is close to 0.1 MHz, dominated by the uncertainty in B_{LCR}. [c] ± 0.3 MHz.

Table 3.3: Muon and proton hyperfine constants determined from the μ-LCR spectrum of the muoniated hydrofuranyl radical in 2,5-dihydrofuran hydrate at -12°C

B_{LCR} /kG[a]	ΔM	hfc /MHz[b]	assignment
13.436	1	366.0	muon in CHMu
14.319	0	98.2	proton, axial β-H
14.579	0	93.4	2 × proton, equatorial β-H
22.830	0	-59.5	proton, α-H

[a] Resonance field. [b] ± 0.1 MHz, dominated by the uncertainty in B_{LCR}.

To explore the issue of distinct conformations, we computed optimized radical geometries and the corresponding hyperfine constants. No attempt was made to account for medium effects, i.e. the results correspond to isolated molecules. In addition

to the trivial isotope effect arising from the different magnetic moments, muon hyperfine constants are generally larger than the equivalent proton couplings by 10-40%.[26,135] This is explained by the enhanced zero-point energy of vibrations involving Mu and the effect of vibrational averaging over anharmonic potentials.[134,118,136] Our calculations, reported in Table 3.4, refer to vibrationally averaged hyperfine constants at 0 K. In the absence of isotope effects the different conformers of the cyclopentyl radical have the same energy. However, when zero-point energy is included the conformer with C-Mu in the more axial orientation is predicted to be more stable by 0.88 kJ mol^{-1}. This small difference is sufficient to weight the conformers 60% axial, 40% equatorial C-Mu at -10°C. Assuming that interconversion of the conformers is fast compared with the μSR experiment, we predict a weighted average muon hyperfine constant of 383 MHz for muoniated cyclopentyl, in reasonable agreement with experiment (376 MHz for the radical in liquid phase). The result is even closer if we take the weighted average of hyperfine constants vibrationally averaged at 263 K, but we believe that this may be fortuitous given the modest basis set and that medium effects were ignored.

Table 3.4: Muon and proton hyperfine constants[a] calculated for different ring conformations, and comparison of their Boltzmann-averaged values with experimental values determined for the radicals in clathrate hydrates

nucleus[b]	axial Mu	equatorial Mu	<*A*>[c]	expt.
	Muoniated cyclopentyl ΔE = 0.883 kJ mol^{-1}			
muon	460	269	383	381
β_1	74	129	96	92
β_2	75	129	96	92
β_3	127	71	105	103
α	-61	-61	-61	-60
	Muoniated hydrofuranyl ΔE = 0.759 kJ mol^{-1}			
muon	464	247	374	366
β_1	69	131	95	93
β_2	93	113	101	93
β_3	111	91	103	98
α	-59	-59	-59	-60

[a] MHz [b] β_1 refers to the proton in CHMu; β_2 and β_3 refer to protons in the β CH_2 [c] Average hyperfine constant weighted according to the relative energies of the conformers.

Our finding that the hyperfine constant of Mu in hydrates is similar to that of ice and vacuum is consistent with minimal interaction of Mu with the clathrate lattice. This is in contrast to Mu interactions in solids such as Silicon and Germanium where Mu interacts strongly with the medium.[137]

3.3. Conclusions

Natural gas hydrates constitute a valuable energy resource in nature, but a significant explosion hazard in their extraction, transport and industrial processing. Fundamental data on the behaviour of H atoms and free radicals in these materials could be valuable, but little is known. Radicals are intermediates in combustion reactions and learning about their reactivity could help with defining conditions that avoid explosion. We have demonstrated the ability to detect and characterize muonium and muoniated free radicals in clathrate hydrates formed from small organic guest molecules. Muonium was detected in the hydrates of cyclopentane and tetrahydrofuran; its hyperfine constant is close to the vacuum value, consistent with a non-bonded atom. Muoniated radicals were detected in the hydrates of related unsaturated guest molecules: cyclopentene and 2,5-dihydrofuran. Their muon spin spectra differ from those in the liquid state at the same temperature, providing clear evidence of restricted motion of the radicals in the clathrate cavities. Comparison of experimental and computed hyperfine constants supports the notion that the radicals exist in inequivalent non-planar conformations which rapidly interconvert at -10°C.

Chapter 4.

Characterization of free radicals in clathrate hydrates of furan, 2,3-dihydrofuran and 2,5-dihydrofuran by muon spin spectroscopy

4.1. Introduction

The contents of this chapter have been published in the Journal of Physical Chemistry A, 2016, 120, 8521-8528.[27]

Muon and proton hyperfine coupling constants for the muoniated radicals formed in the clathrates of furan and two isomeric dihydrofurans were determined. Samples were studied in neat liquid form as well as clathrate hydrates, in order to investigate the potential influence of the local environment on the reactivity of the molecules. Samples were prepared as mentioned in section 2.2.

DFT calculations were used to guide the spectral assignments and distinguish between competing radical products for Mu addition to furan and 2,3-dihydrofuran. Relative signal amplitudes provide yields and thus the relative reactivities of the C4 and C5 addition sites in these molecules. The expected reactions are depicted in Scheme 4.1. Radical **3** is an isotopomer of radical **1**, i.e. they differ only in the site of Mu substitution. The structures include explicit hydrogens only for those atoms which are expected to have significant hyperfine interaction with the unpaired electron. Similarly, to aid subsequent discussion, some H atoms are labeled α (H attached to C with the unpaired electron) or β (H attached to one C away from C-α) to denote their relation to the radical centre. Isotropic muon and proton hyperfine constants were used to identify the individual radical signals and thence determine the branching ratio of the reactions.

Optimized geometries and hyperfine coupling constants of muoniated free radicals were calculated using the B3LYP hybrid functional and the 6-31G(d) basis set. Similar calculations were performed with the EPR-II basis set for comparison purposes. These data (supporting information) are in Appendix C.

Scheme 4.1: Muonium addition to 2,5-dihydrofuran, 2,3-dihydrofuran, and furan

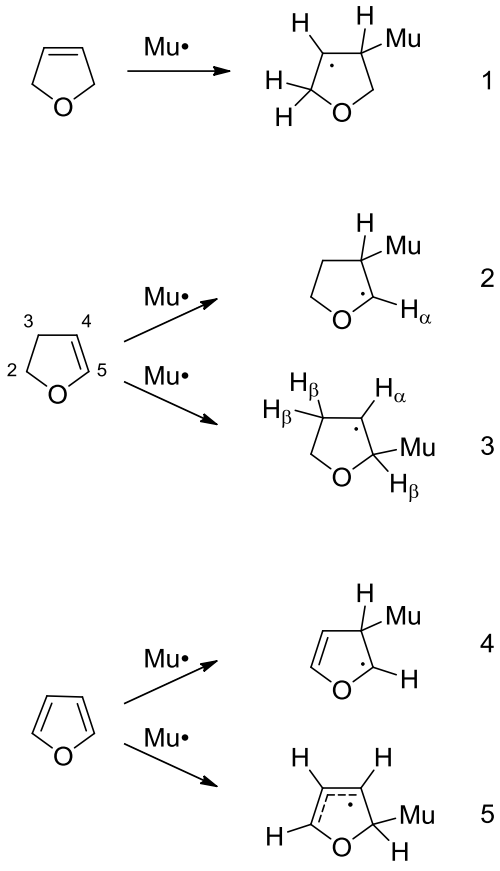

4.2. Results and discussion

A single muoniated radical (**1**) was detected in the clathrate hydrate of 2,5-dihydrofuran, and was characterized by TF-μSR and μ-LCR. Small but significant differences were found between the hyperfine constants of the radical in the liquid phase

and in the clathrate hydrate. In addition, the existence of a $\Delta M = 1$ avoided level-crossing resonance indicates that the radical is not tumbling freely in the clathrate structure as mentioned in the previous chapter. This implies that there is some host–guest interaction, and indeed, hydrogen-bonding is known to occur for a variety of guest molecules in clathrate hydrates, including small ethers.[138,139,140]

To explore the possibility of strong radical-host interactions, a DFT calculation on tetrahydrofuran-3-yl (the H isotopomer of **1**) at the center of a single cage of 28 water molecules arranged to mimic the $5^{12}6^4$ cavity[141] of structure II clathrate was performed. A very shallow, non-bonding potential was found, and the radical's geometry and hyperfine constants were similar to results for the isolated molecule. This does not exclude the likelihood of hydrogen bonding, however, because the B3LYP functional and 6-31G(d) basis set used are not adequate to describe dispersion interactions. DFT calculation showed that inside of the clathrate cages have a relatively uniform and low electrostatic potential in comparison with the outside oxygen and hydrogen atoms.[141] In general, guest–host interactions in clathrate hydrates are dominated by van der Waals interactions.[141] To address this point some test calculations were made with dispersion included, specifically the D3 version of Grimme's dispersion with Becke-Johnson damping[142] as implemented by the EmpiricalDispersion=GD3BJ command in Gaussian 09. The results suggest an off-centre location of the radical with preferential orientation of the guest with the oxygen atom pointing at a pentagon window of the cage. The hyperfine constants varied with orientation by a few percent, but were not investigated further. (An in-depth computational study would have to consider averaging over multiple orientations varying in energy by a few kJ mol^{-1}.) The focus of the study was on the identification of guest radicals.

It was noted in the previous chapter that the muon hfc of 1 decreases with temperature, and that two conformers exist. In one of them Mu takes a quasi-axial orientation with respect to the ring, and the other quasi-equatorial. The observation of a single radical implies that the two conformers rapidly interconvert, presumably as a result of non-planar ring fluctuations as suggested by ESR studies of similar 5-membered alicyclic radicals.[143] The observed muon hfc can then be expressed as a weighted average of the values for the axial (X) and equatorial (Q) structures:

$$A_{\mu}(\text{obs}) = w_{\text{X}} A_{\mu}(\text{X}) + w_{\text{Q}} A_{\mu}(\text{Q}) \qquad (4.1)$$

where w_X and w_Q are determined by the Boltzmann populations of the two conformers separated in energy by ΔE. The extended temperature range of the TF-μSR studies including the muon hfcs are presented in Figure 4.1. The line through the points corresponds to a fit to eq 4.1, which has three adjustable parameters (ΔE and the two hfcs). This shows that the model is consistent with the observed temperature dependence, but other vibrational modes are also likely to contribute (e.g. C-Mu bond stretching and wagging), so little emphasis is placed on the precise values of the optimized parameters.

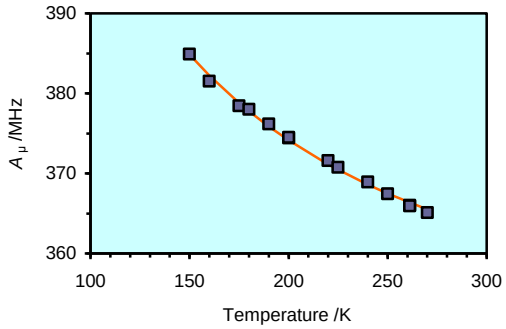

Figure 4.1: Isotropic muon hyperfine constants of guest radical 1 in 2,5-dihydrofuran hydrate. The errors on A_μ are within the size of the data symbols. The line through the data points depicts a fit to a model which assumes a Boltzmann-weighted average of two conformers. Adapted with permission.[27] Copyright 2016, American Chemical Society.

As shown in Scheme 4.1, addition of Mu to 2,3-dihydrofuran is expected to produce two distinct product radicals, **2** and **3**. That this indeed happens is evident from Figure 4.2, which displays the TF-μSR spectrum recorded for a hydrate sample of this compound. The muon hfcs for the radicals are listed in Table 4.1. The larger of the two values is similar to the muon hfc of radical **1** and is assigned to structure **3**. The unpaired electron in radical **2** is nominally on C5 but is partially delocalized onto the neighbouring O atom. The reduction in unpaired spin density on C5 compared to C4 results in lower

values for both the α and β proton hfcs of the equivalent radicals studied by ESR (tetrahydrofuran-5-yl and tetrahydrofuran-4-yl).[143]

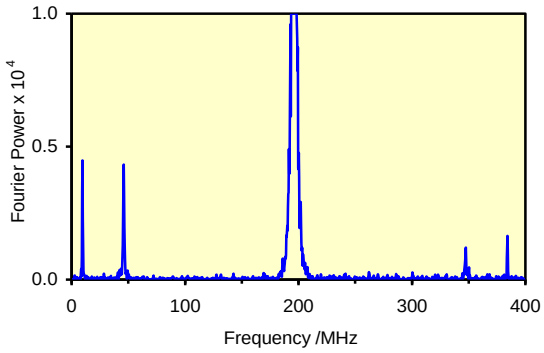

Figure 4.2: **Fourier power TF-μSR spectrum from 2,3-dihydrofuran hydrate at -10°C and 14.5 kG. The outer pair of peaks (those furthest from the diamagnetic signal at 196 MHz) corresponds to a radical with muon hyperfine constant 374 MHz. The inner pair of peaks arise from a radical with muon hyperfine constant 301 MHz. Adapted with permission.[27] Copyright 2016, American Chemical Society.**

Table 4.1: **Muon hyperfine constants A_μ determined from TF-μSR spectra**

sample	temperature /°C	A_μ /MHz [a]	assignment
2,5-dihydrofuran liquid	–10	367.28(4)[b]	1
2,5-dihydrofuran hydrate	–12	365.99(5)[b]	1
2,3-dihydrofuran liquid	–10	299.85(3)	2
2,3-dihydrofuran liquid	–10	371.21(4)	3
2,3-dihydrofuran hydrate	–10	301.43(10)	2
2,3-dihydrofuran hydrate	–10	374.52(4)	3
furan liquid	–10	499.93(15)	4
furan liquid	–10	379.97(2)	5
furan hydrate	–13	499.34(11)	4
furan hydrate	–13	382.19(5)	5

[a] Statistical uncertainty denoted by decimal digits in parentheses. [b] Values previously reported.[22]

A more detailed comparison of hyperfine constants can be made after analysis of the μ-LCR spectra obtained from the liquid and clathrate hydrate samples. Figure 4.3 displays a series of field scans that show the full series of resonances obtained from the 2,3-dihydrofuran hydrate sample. The signals at about 11.1 kG and 13.7 kG are readily identified as due to the $\Delta M = 1$ resonances of **2** and **3**, respectively, because they match the field values calculated with eq 1.24 using the muon hyperfine constants already determined by TF-μSR. Furthermore, these signals are absent for the liquid phase sample. All the other signals arise from $\Delta M = 0$ resonances due to protons. Individual proton hfcs were calculated from resonance fields by means of eq 1.23. In principle there is ambiguity caused by the two different values of A_μ which arise from the two radicals. Sometimes the choice is obvious. For example, the two highest-field resonances correspond to negative hfcs and are assigned to α C-H protons in the same order as the two A_μ values. A complete list of resonances and hfcs is given in Table 4.2. The assignment to individual radicals and nuclei was made with the aid of DFT calculations whose results are summarized in Table 4.3. As explained earlier for the muon hfcs and expressed in eq 4.1, the observable hfcs are Boltzmann-weighted averages of values for the two conformers corresponding to Mu in pseudo-axial and pseudo-equatorial positions. Switching between the two conformations requires a ring twist which results in exchange of the β-CH_2 protons and the "flip" of the β-CHMu group.

As a further check on the analysis, the calculated and experimental hfc values can be compared with ESR results for tetrahydrofuran-5-yl and tetrahydrofuran-4-yl (i.e. **2** and **3** with H replacing Mu). Gilbert and Trenwith reported α-proton coupling constants of (–)34.4 MHz and (–)59.4 MHz, respectively, and β-proton constants of 80.1 MHz and 99.5 MHz for the radicals in aqueous solution at 8°C.[143] (The negative signs are assumed, since first-order ESR splittings do not distinguish sign.) Tetrahydrofuran-5-yl has also been identified in a γ-irradiated clathrate at 123 K, with ESR splittings of (–)38.4 MHz and 78.2 MHz.[127] The results and analysis are fully consistent with these literature data.

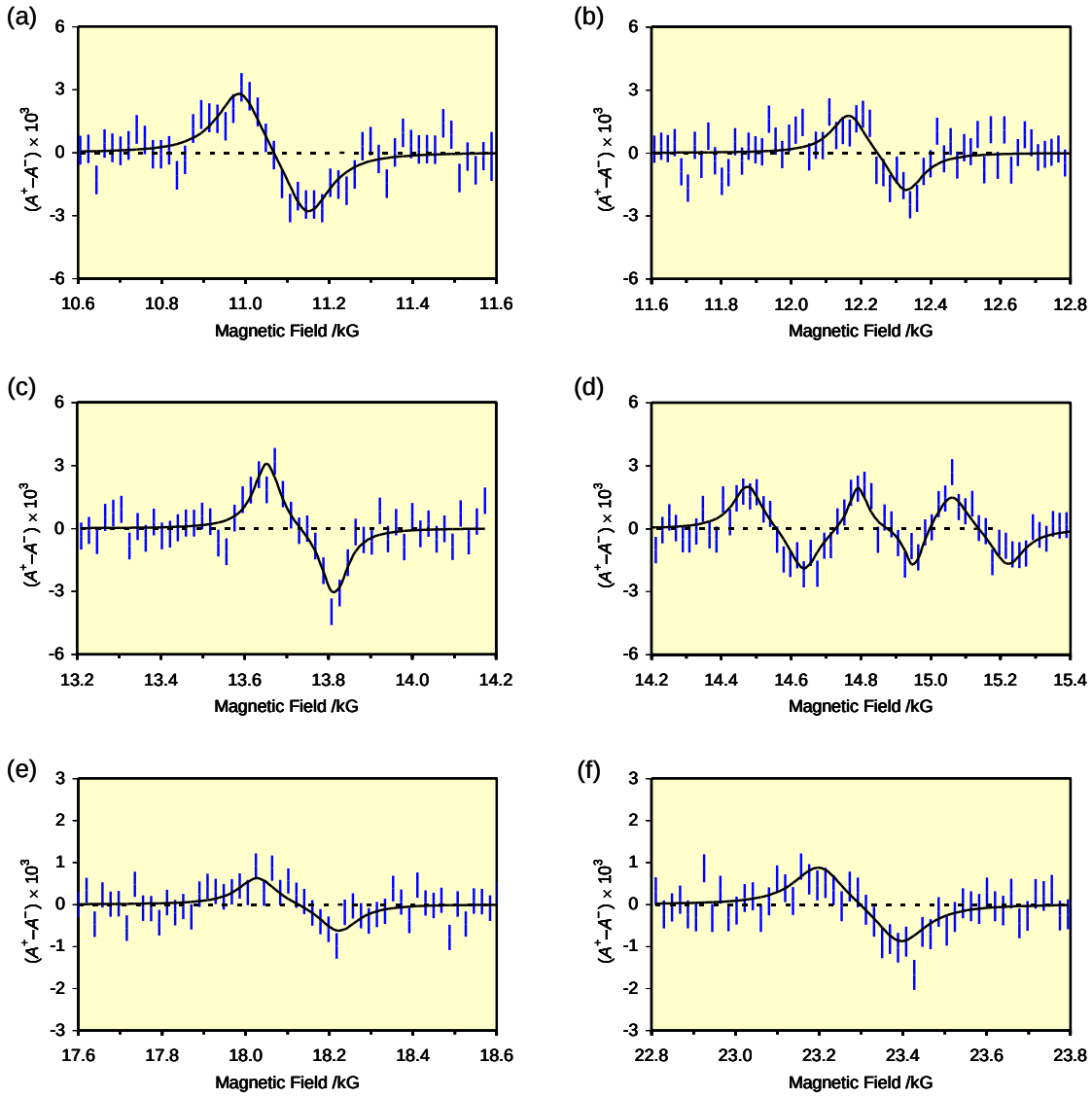

Figure 4.3: **Segments of the muon avoided level-crossing spectrum obtained from the clathrate hydrate of 2,3-dihydrofuran. Most resonances were recorded at –10°C but e and f were scanned at –13°C. Also, these two segments have an expanded y-scale, to show the weak signals. Overall, the signals arise from two different radicals and include both Δ*M*=1 and Δ*M*=0 resonances. Their eventual assignments are given in Table 4.2. Adapted with permission.[27] Copyright 2016, American Chemical Society.**

Table 4.2: Muon and proton hyperfine constants determined from the μ-LCR spectra of radicals detected in liquid 2,3-dihydrofuran and its clathrate hydrate at −10°C

sample	B_{LCR} /kG	Δ*M*	hfc /MHz	radical	assignment
liquid	12.031(5)	0	75.0(1)	**2**	β-C**H**Mu
liquid	14.403(6)	0	101.8(1)	**3**	β-C**H**Mu
liquid	14.623(6)	0	97.8(1)	**3**	β-C**H** axial
liquid	14.835(8)	0	93.8(2)	**3**	β-C**H** equat.
liquid	18.056(4)	0	-36.7(1)	**2**	α-C**H**
liquid	23.072(4)	0	-58.8(1)	**3**	α-C**H**
hydrate	11.068(6)	1	301.5(2)	**2**	muon
hydrate	12.247(9)	0	72.5(2)	**2**	β-C**H**Mu
hydrate	13.733(4)	1	374.1(1)	**3**	muon
hydrate	14.556(7)	0	101.9(2)	**3**	β-C**H**Mu
hydrate	14.872(6)	0	96.0(2)	**3**	β-C**H** axial
hydrate	15.140(8)	0	91.1(2)	**3**	β-C**H** equat.
hydrate	18.125(11)[a]	0	-36.4(2)	**2**	α-C**H**
hydrate	23.298(10)[a]	0	-60.1(2)	**3**	α-C**H**

[a] scanned at -13°C

Table 4.3: Computed[a] hyperfine constants for radicals 2 and 3 compared with those determined by μ-LCR spectroscopy on liquid and clathrate hydrate samples of 2,3-dihydrofuran at −10°C

nucleus	*A*(Mu-ax)	*A*(Mu-eq)	$A_{calc.}$[b]	A_{exp}(liq)	A_{exp}(hydr.)
radical **2**					
muon	403.4	172.2	318.6	(299.9)[c]	301.5
β-C**H**Mu	50.1	112.9	73.2	74.9	72.5
α-C**H**	-38.2	-38.8	-38.4	-36.7	-36.4[a]
radical **3**					
muon	393.0	333.1	370.3	(371.2)[c]	374.1
β-C**H**Mu	90.5	108.6	97.3	101.8	101.9
α-C**H**	-54.5.1	-54.1	-54.3	-58.8	-60.1[a]
β-**H** axial	122.5	64.6	100.6	97.8	96.0
β-**H** equatorial	67.7	123.8	88.9	93.8	91.1

[a] UB3LYP/6-31G(d). [b] Weighted average of two conformations. [c] Value obtained by TF-μSR.

Muonium addition to furan also gives rise to two radicals, but with very different yields, as evident from the TF-μSR spectrum shown in Figure 4.4. The neat liquid sample gave similar results for A_μ (Table 4.1). Comparison with ESR data[144,145,146,147] and an earlier muon spectroscopic study[148] indicates that the stronger signal (smaller muon hfc) is due to radical **5** and the weaker signal is from **4**. This assignment is supported by the DFT calculations, which show that **5** is more stable than **4**, as might be expected from the enhanced spin delocalization over the allylic structure. There is weak temperature dependence for the muon hfc of **4** in the neat liquid, but a negligible effect for **5** (Table 4.4). This is probably because 5 has a planar ring due to the bond conjugation and is therefore insensitive to the axial–equatorial conformational averaging discussed above for the other radicals.

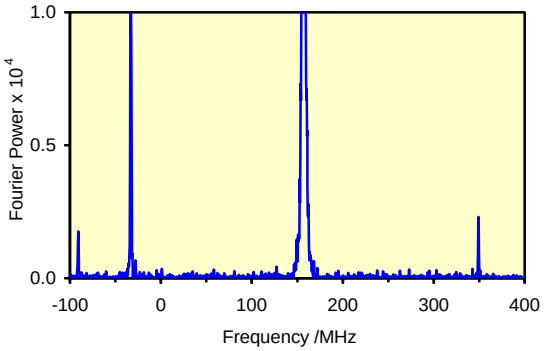

Figure 4.4: **Fourier power TF-μSR spectrum obtained from furan hydrate at -13°C and 11.6 kG. Two radicals are evident, with muon hyperfine constants of 382 MHz and 499 MHz, but the upper precession frequency from the latter radical (expected at 409 MHz) is not discernible among the noise. Adapted with permission.[27] Copyright 2016, American Chemical Society.**

Table 4.4: **Muon hyperfine constants for radicals 4 and 5 in liquid furan determined by TF-μSR**

temperature/ °C	A_μ /MHz for 4	A_μ /MHz for 5
10	498.61(13)	379.32(1)
-10	499.93(15)	379.97(2)
-15	500.17(13)	379.97(1)

Figure 4.5 displays a collection of μ-LCR scans obtained from the furan hydrate sample. As was the case for 2,3-dihydrofuran, the $\Delta M = 1$ resonances are readily identified by matching the predictions of eq 1.24. Thus, the signals at 14.0 kG and 18.4 kG correspond to A_μ values of 382.2 MHz and 500.1 MHz and are assigned to **5** and **4**, respectively. The other signals are interpreted as $\Delta M = 0$ resonances (eq 1.23) and assigned (Table 4.5) with the aid of DFT calculations. These predictions (Table 4.6) are particularly important because the spectrum contains overlapping signals. It is obvious that there are two resonances near 19.7 kG but our assignment is not unique. By switching the assignments of the two resonances we instead determine A_p values of 12.5 MHz for **5** and 131.3 MHz for **4**. The signal near 22.5 kG (Figure 4.5 d) has also been interpreted as two almost degenerate resonances, although the quality of the fit with the current data does not allow clear discrimination between single or double resonances. ESR studies[144-147]report only a single value for the allylic protons, but calculations predict slightly different values, and an early μ-LCR study of the radical in liquid furan included a high resolution scan that shows clear splitting.[148]

Having identified the muoniated radicals formed from furan and 2,3-dihydrofuran we are now able to deduce the relative reactivities of the C4 and C5 sites in these molecules. As is evident from Figure 4.4, for furan one radical (**5**) is formed in greater abundance than the other (**4**). The ratio of TF-μSR signal amplitudes is 4.9 ± 0.8 for furan hydrate and 3.2 ± 0.7 for liquid furan. Similar values (5.4 and 4.2 respectively) were found from the amplitudes of $\Delta M = 0$ μ-LCR signals. The computed energy of **5** is 49 kJ mol^{-1} lower than **4**, so the fivefold greater yield must be due to kinetic control (lower activation energy), not thermodynamic. Thus we deduce that the C5 site of furan is more reactive than the C4 site to Mu (and hence H-atom) attack. In the case of 2,3-dihydrofuran, the ratio (radical **3** to radical **2**) of TF-μSR signal amplitudes is 0.38 ± 0.6 for the hydrate and 0.44 ± 0.5 for the liquid sample. This implies that C4 is more reactive than C5 for this molecule. The switch in reactivity parallels the relative stability of the ensuing radical products, which is dominated by the facile formation of the planar allylic system in **5**. The small changes in selectivity with phase (pure liquid or crystalline hydrate) may be related to the weak interaction between the guest and the clathrate lattice, but detailed modeling will be necessary to explore this possibility.

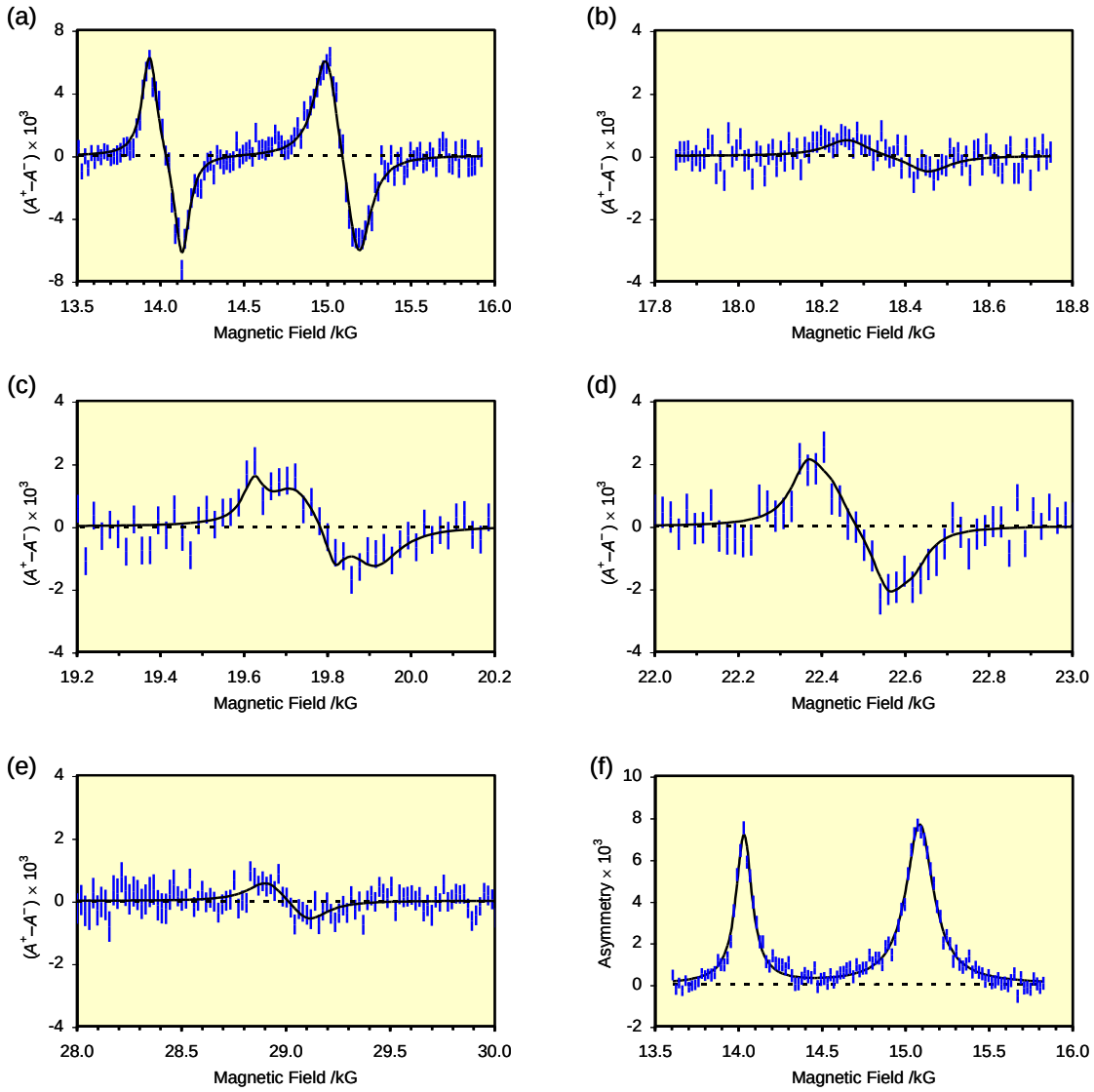

Figure 4.5: **Segments of the muon avoided level-crossing spectrum obtained from the clathrate hydrate of furan at -13°C. Note that segment** a **has a different y-scale compared to b-e. The resonances arise from two different radicals, 4 and 5, and are assigned as shown in Table 4.5. Segment f contains the same data and fit as a but displayed in integral form to demonstrate the symmetrical Lorentzian lineshapes. Adapted with permission.[27] Copyright 2016, American Chemical Society.**

Table 4.5: Muon and proton hyperfine constants determined from the μ-LCR spectrum of radicals detected in furan clathrate hydrate at −13°C

B_{LCR} /kG	Δ*M*	hfc /MHz	radical	assignment
14.031(2)	1	382.2(1)	**5**	muon
15.088(3)	0	100.1(1)	**5**	β-C**H**Mu
18.358(11)	1	500.1(3)	**4**	muon
19.720(7)	0	14.3(1) [a]	**5**	C(3)**H** [a]
19.816(11)	0	129.5(4) [a]	**4**	β-C**H**Mu [a]
22.463(6)	0	-36.6(1)	**5**	α-C(2)**H**
22.522(12)	0	-37.7(2)	**5**	α-C(4)**H**
29.010(13)	0	-40.8(4)	**4**	α-C**H**

[a] Alternative assignment possible. See text.

Table 4.6: Computed[a] hyperfine constants for radicals 4 and 5 compared with those determined by μ-LCR spectroscopy on liquid and clathrate hydrate samples of furan at −13°C

nucleus	*A*(Mu-ax)	*A*(Mu-eq)	$A_{calc.}$ [b]	A_{exp}(liq) [c]	A_{exp}(hydr.) [d]
radical **4**					
muon	542.9	504.5	526.7	(497) [e]	500.1
β-C**H**Mu	138.0	147.8	142.1	130	129.5
α-C**H**	-49.6	-51.8	-50.5		-40.8
radical **5**					
muon	–	–	405.5	(378.8) [e]	382.2
β-C**H**Mu	–	–	107.2	100.2	100.1
C(3)**H**	–	–	10.5		14.3
C(2)**H**	–	–	-37.9	-36.4	-36.6
C(4)**H**	–	–	-39.9	-37.2	-37.7

[a] UB3LYP/6-31G(d). [b] Weighted average of two conformations. [c] Ref.[148], 25°C. [d] This work. [e] Value obtained by TF-μSR.

4.3. Conclusions

Radicals can be formed by reaction of muonium with unsaturated organic molecules, and the detection of muoniated radicals by transverse-field μSR implies that they are formed very quickly (< 300 ps) after muon implantation in the sample. Isotropic muon hyperfine constants can be determined from TF-μSR spectra, and proton hyperfine constants by muon avoided level-crossing spectroscopy. By these means radicals can be identified and distinguished when there are competing products, such as in the addition of muonium to furan and to 2,3-dihydrofuran. The relative yields of the radicals reflect the reactivities of the different reaction sites. The temperature dependence of hyperfine constants provides information on intramolecular motion. In particular, the various hydrofuranyl radicals studied have non-planar ring structures which can rapidly twist to interconvert pseudo-axial and pseudo-equatorial H and Mu substituents. This occurs both for radicals in liquids and as guests in clathrate cages. In contrast, the overall molecular tumbling that produces isotropic spectra for radicals in liquids is restricted for radicals in clathrates, as evidenced by additional resonances which appear in the μ-LCR spectra of the latter. More generally, this study demonstrates the utility of muonium (and the associated muon spin spectroscopy) as an isotopic substitute of the H atom to probe the behavior of radical species formed in environments difficult to study by more mainstream techniques.

Chapter 5.

Characterization of free radicals in clathrate hydrates of pyrrole, thiophene and isoxazole by muon spin spectroscopy

5.1. Introduction

The contents of this chapter have been published in the Journal of Canadian Chemistry, 2017, doi.org/10.1139/cjc-2017-0313.

Muon spin spectroscopy was used to study muoniated radical products of isoxazole, thiophene and pyrrole in pure liquids and in clathrate hydrates of these materials. Characterization of the muoniated radical products (similar to previous chapter) was done and the results were compared to see how is the unpaired spin distribution affected if O atom in furan is replaced with S (thiophene) or N (pyrrole). How does the reactivity of the molecules change if N atom replaces the C next to O in furan (isoxazole)? How does it affect the guest-host interaction?

Optimized geometries and hyperfine coupling constants of muoniated free radicals were calculated using the UB3LYP hybrid functional and the 6-311G(d,p) basis set. Similar calculations were performed with the EPR-II basis set for comparison purposes except in the case of thiophene where EPR-II basis set couldn't be used. This basis set is only applicable to atoms H and B to F.[115] The cc-pVTZ basis set was used instead.[149,150] DFT calculations were used to guide the spectral assignments and differentiate among competing radical products.

5.2. Results and discussion

Muonium addition to isoxazole, thiophene and pyrrole leads to the formation of the muoniated radicals shown in Scheme 5.1 and 5.2: The radicals are marked with the numbers **1**-**5**. The muon hyperfine constants, A_μ determined from the TF-μSR spectra of all samples are listed in Table 5.1.

Scheme 5.1 shows that there are four possibilities when Mu is added to isoxazole, depending on which double bond will break and where Mu is added. However, only one of these radicals (**1a**) was seen in both liquid and hydrate. Radical **1a** is more stable than the rest of the radicals according to the calculation results. Radical geometries **1a-d** were optimized using the UB3LYP functional and the 6-311G(d,p) basis set and the energies are summarized in Table 5.2.

Scheme 5.1: Muonium addition to isoxazole

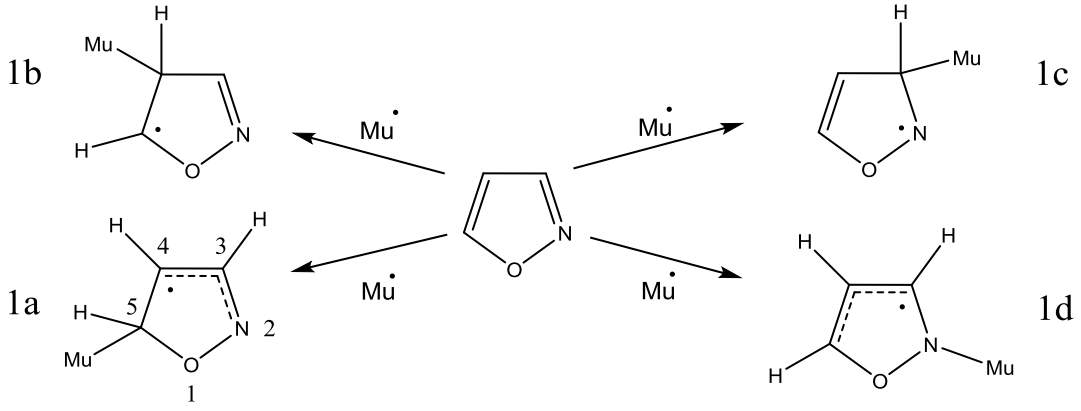

Table 5.1: Muon hyperfine constants A_μ determined from TF-μSR spectra

sample	temperature /°C	A_μ /MHz [a]	assignment
isoxazole liquid	–9	442.12(9)	1a
isoxazole hydrate	–13	442.51(28)	1a
pyrrole liquid	–9	563.06(9)	2
pyrrole liquid	–9	435.40(1)	3
pyrrole-methane hydrate	–73	567.67(9)	2
pyrrole-methane hydrate	–73	446.41(3)	3
thiophene liquid	–9	485.50(4)	4
thiophene liquid	–9	339.76(2)	5
thiophene-xenon hydrate	–30	492.64(35)	4
thiophene-xenon hydrate	–30	343.69(24)	5

[a] Statistical uncertainty denoted by decimal digits in parentheses.

Scheme 5.2: Muonium addition to pyrrole and thiophene

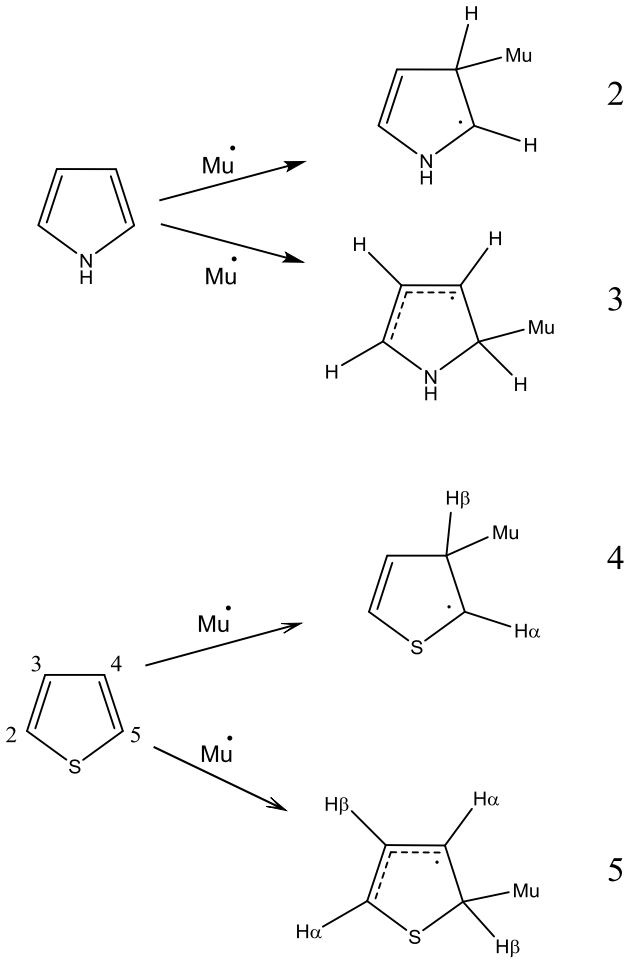

Table 5.2: Energies of the optimized[a] radical structures 1a-d

Radical	Minimized energy / kJ mol^{-1}	Order of stability	$E_{reaction}$[b]/ kJ mol^{-1}
1a	-647603	1	-418
1d	-647563	2	-377
1c	-647556	3	-371
1b	-647553	4	-367

[a] UB3LYP/6-311G(d,p).[b] $E_{reaction} = E_{radical} - (E_{isoxazole} + E_{H(Mu)})$

Table 5.3: Muon, proton and nitrogen hyperfine constants determined from the μ-LCR spectra of radical 1a detected in liquid isoxazole at −9°C and its clathrate hydrate at −13°C

sample	B_{LCR} /kG	ΔM	hfc /MHz	assignment
liquid	17.143(4)	0	121.5(1)	β-C**H**Mu
liquid	22.597(25)	0	20.5(5)	β-C**H**
liquid	25.661(11)[a]	0	-36.3(2)	α-C**H**
liquid	15.667(3)	0	24.9(1)	N
hydrate	16.224(9)	1	441.9(2)	muon
hydrate	17.198(5)	0	120.9(3)	β-C**H**Mu
hydrate	15.702(12)	0	24.3(4)	N

[a] scanned at -10°C.

The TF-μSR spectra of the muoniated radical in isoxazole liquid (top) and hydrate (bottom) are displayed in Figure 5.1. The radical peaks in the liquid are sharper as is obvious from the top figure. The muon hfc is calculated from the difference between the radical frequencies at -62.6 and 379.5 MHz. In the hydrate, bottom figure, only the negative frequency is observed at -62.7 MHz. Higher frequency signals often have reduced amplitude. This is partly due to limited time resolution of the detector system, but can also arise from partial spin dephasing when muonium is transformed to a radical which has a different precession frequency. If the higher frequency signal is weak, it is still possible to calculate A_μ from ν_{R1} and the diamagnetic frequency, ν_μ , using equation 2.2.[27] From the TF-μSR, the muon hfc is 442.51(28) MHz in the hydrate at -13°C which is in agreement with 441.9(2) MHz from the μ-LCR results. The muon, proton and nitrogen hyperfine constants determined from the μ-LCR spectra of the

radicals detected in the hydrate and the liquid isoxazole are listed in Table 5.3. Equation 1.23 was used to obtain the proton and nitrogen hyperfine coupling constants. The computed hfcs are compared with the experimental ones in Table 5.4. Three basis sets: 6-311G(d,p), 6-31g(d) and EPR-II were used to obtain the computed results. In general there is good agreement between the calculated and experimental hfcs. Calculation was done on the isolated molecules without taking into account the effect of the medium. Our previous results for calculating hfcs of tetrahydrofuran-3-yl inside the cage showed that the hfcs for the different orientations of the molecule inside the cage were similar to the hfcs of the isolated molecule.[27] Also DFT calculations with the D3 empirical dispersion correction on the radicals of H• and OH• encapsulated in hydrate cages showed that they have similar structures and properties like atomic charges, spin densities, and electronic configurations such as in their free forms.[151]

Compared with the similar radical in furan, the β-C**H**s have higher hyperfine coupling constants showing the effect of N instead of C next to O (**1a** in Scheme 5.1 vs. **5** in Scheme 4.1 on page 53). The nitrogen atom allows the transfer of a larger fraction of spin density onto the oxygen as compared with the case where C is next to O such as in furan.[152] Radical **1a** has a planar structure and there is an equal probability for Mu in the axial or equatorial position with respect to the ring. The unpaired electron is delocalized over the nitrogen atom, C3 and C4 and it is the most stable radical among **1a-d**. This result is consistent with the electron spin resonance study of OH addition to isoxazole which also occurs at the C5 position of the ring to produce an allylic radical.[153]

Figure 5.2 shows all the μ-LCR spectra for radical **1a** in isoxazole liquid and hydrate. In the case of hydrate, there is an extra resonance, $\Delta M = 1$ which is consistent with our previous results.[22,27] It shows that the radical is not tumbling freely in the hydrate. It is known that host-guest interaction such as hydrogen bonding occurs for some guest molecules in hydrates.[138,140,154] LCR signals from β-C**H** and α-C**H** were not detected in the hydrate. They are expected to be weak and long acquisition times would be necessary to observe them. We had to prioritize the use of limited beam time.

Table 5.4: **Computed hyperfine constants (MHz) for radical 1a vibrationally averaged at −13°C compared with those determined by μ-LCR spectroscopy in liquid isoxazole at −9°C and the hydrate at −13°C**

nucleus	A_{calc}[a]	A_{calc}[b]	A_{calc}[c]	A_{exp}(liq.)	A_{exp}(hydr.)
muon	445.3	456.3	466.1	442.12(9)[d]	441.9(2)
β-C**H**Mu	122.1	124.9	128.4	121.5(1)	120.9(3)
β-C**H**	9.7	11.1	10.1	20.5(5)	
α-C**H**	-34.9	-38.6	-37.0	-36.3(2)	
N	16.2	24.9	20.5	24.9(1)	24.3(4)

[a] UB3LYP/6-311G(d,p).[b] UB3LYP/6-31G(d). [c] UB3LYP/EPR-II [d] Value obtained by TF-μSR.

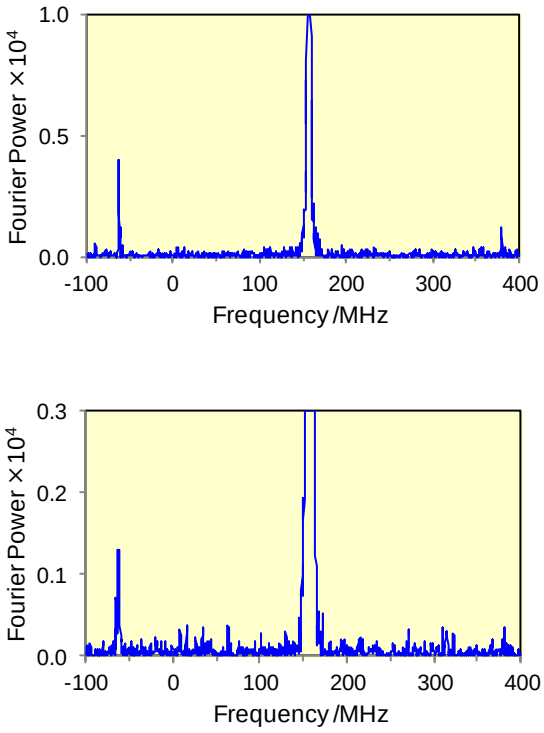

Figure 5.1: **Fourier power TF-μSR spectra obtained from radical 1a in isoxazole liquid at 11.6 kG and -9°C (top), and isoxazole hydrate at -13°C (bottom). The peak at 157 MHz is the diamagnetic signal. The pair of radical frequencies at -62.6 and 379.5 MHz is obvious in the liquid but only the negative frequency is detected in the hydrate.**

When Mu adds to thiophene, two types of radicals (**4** and **5**) are formed as shown in Scheme 5.2. The Fourier power TF-μSR spectra are shown in Figure 5.3; liquid thiophene in the top and thiophene-xenon hydrate in the bottom. The hfcs determined from μ-LCR spectra as well as the calculated hfcs are summarized in Tables 5.5 and 5.6 respectively. The μ-LCR data of liquid thiophene comes from prior, unpublished work by Percival et al. at room temperature (A_μ at room temperature was used to obtain hfcs). Figure 5.4 shows all the μ-LCR spectra for radicals **4** and **5** in the hydrate.

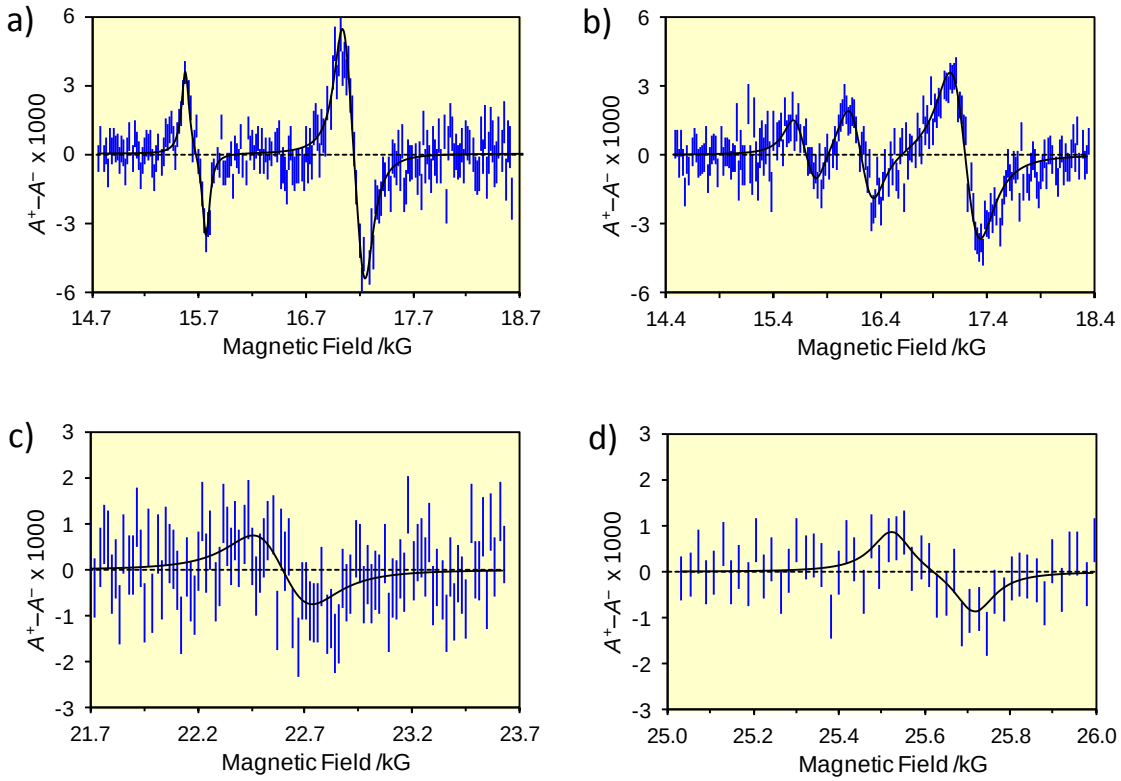

Figure 5.2: **Segments of the muon avoided level-crossing spectra obtained from radical 1a in the liquid [a,c,d] and the clathrate hydrate of isoxazole [b]. The liquid spectra a and c were obtained at -9°C, d at -10°C. The hydrate spectrum, b, was obtained at -13°C.**

According to Table 5.6 results, the 6-311G(d,p) basis set seems to underestimate the muon and β-C**H**Mu hfcs in radical **4** unlike the cc-pVTZ basis set

which gives better results but there is good agreement between the experimental and calculated hfcs in radical **5** at -30°C.

The radical amplitude ratios of **5** to **4** are 2.2(2) in the liquid and 2.5(4) in the hydrate showing that the major radical product is **5**. This result is consistent with the calculation (UB3LYP/6-311G(d,p)) which showed that radical **5** is 51 kJ/mol more stable than radical **4**. ESR data of the reaction of H atoms with solid thiophene at 130 K, aqueous thiophene and γ-irradiated single crystals of thiophene all showed that the major radical product of H atom addition to thiophene is 2-hydrothienyl radical formed by the addition of the H atom at the C_2 or C_5 position of the thiophene molecule.[155]

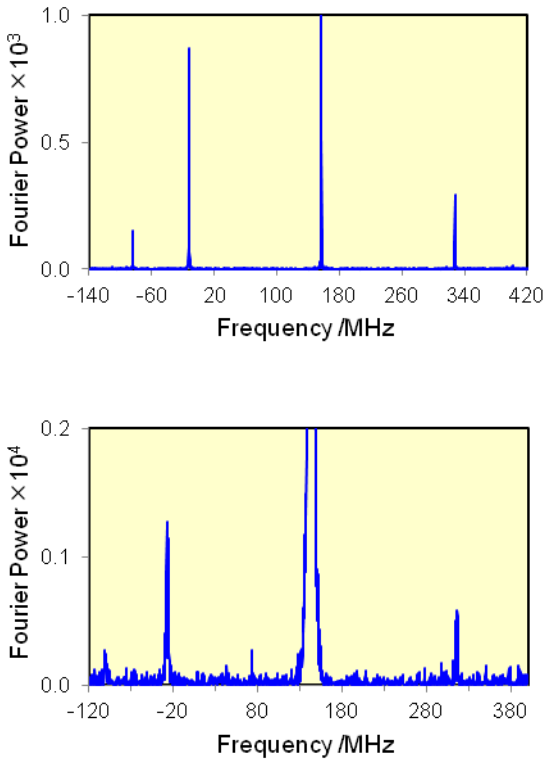

Figure 5.3: Fourier power TF-μSR spectra obtained from radicals 4 and 5 in thiophene liquid at 11.6 kG and -9°C (top), thiophene-xenon hydrate at 10.6 kG and -30°C (bottom). The peaks at 157 MHz and 143 MHz are the diamagnetic signals in the liquid and hydrate respectively.

Both radicals **4** and **5** have planar geometry and so there is no difference between Mu adding at the axial or equatorial position with respect to the ring. Comparing radical **4** to the same radical in furan, **4** in scheme 4.1 on page 53, the C_α-S bond (1.74 Å) is longer than the C_α-O bond (1.38 Å) and the S-C_α-H_α angle is 120° while the O-C_α-H_α angle is 114°. The muoniated radical **4** in furan, doesn't have a planar ring so puckering of the ring happens after Mu addition and it generates two conformations of the radical which are in rapid equilibrium where the probability of having Mu at the axial position is higher than the equatorial position.[27] It seems replacing O with the larger atom, S leads to the planar ring structure and as a result there is no difference between Mu at the axial and equatorial position in the muoniated thiophene radical **4**. However, radical **5** seems not to be as much affected by S atom replacement as compared to the similar radical in furan (**5** in Scheme 4.1 on page 53). ESR data of the protiated radical **5** produced by γ-irradiation of thiophene in the crystalline and adsorbed states (adsorbed on silica gel) showed similar hfcs with the analogous radical in furan (protiated **5** in Scheme 4.1 on page 53), showing that replacement of an S atom by an O atom has little effect on the spin density distribution in the ring system.[156] The ESR values of isotropic hfcs of β-C**H**Mu and the α-Hs in **5** in crystalline thiophene are 93.9, (-)35, (-)41.8 MHz at 203 K and 90.8, (-)33.1, (-)38.1 MHz for the adsorbed thiophene on silica gel at room temperature respectively. The minus sign is assumed since it wasn’t reported in the ESR studies.[156]

Table 5.5: Muon and proton hyperfine constants determined from the μ-LCR spectra of radicals 4 and 5 detected in liquid thiophene at 1°C [a] and the clathrate hydrate at −30°C

sample	B_{LCR} /kG	Δ*M*	hfc /MHz	radical	assignment
liquid	19.254(2)	0	125.2(1)	**4**	β-C**H**Mu
liquid	28.375(2)	0	-45.3(1)	**4**	α-C**H**
liquid	13.216(1)	0	92.4(1)	**5**	β-C**H**Mu
liquid	19.954(2)	0	-32.5(1)	**5**	α-C**H**
liquid	20.141(2)	0	-35.9(1)	**5**	α-C**H**
hydrate	18.047(5)	1	491.6(1)	**4**	muon
hydrate	19.638(8)	0	125.5(4)	**4**	β-C**H**Mu
hydrate	12.632(4)	1	344.1(1)	**5**	muon
hydrate	13.451(6)	0	92.2(3)	**5**	β-C**H**Mu
hydrate	20.201(11)	0	-32.9(3)	**5**	α-C**H**
hydrate	20.343(10)	0	-35.6(3)	**5**	α-C**H**

[a] unpublished work by Percival et al.

Table 5.6: Computed hyperfine constants (MHz) for radicals 4 and 5 vibrationally averaged at −30°C compared with those determined by μ-LCR spectroscopy in liquid thiophene[c] (at 1°C) and the hydrate at −30°C

nucleus	A_{calc}[a]	A_{calc}[b]	A_{exp}(liq.)	A_{exp}(hydr.)
radical **4**				
muon	460	518	485.50(4) [d]	491.6(1)
β-C**H**Mu	113.4	132.6	125.2(1)	125.5(4)
α-C**H**	-19.3	-32.3	-45.3(1)	
radical **5**				
muon	343.3		339.76(2)[d]	344.1(1)
β-C**H**Mu	93.3		92.4(1)	92.2(3)
α-C**H**	-33.1		-32.5(1)	-32.9(3)
α-C**H**	-35		-35.9(1)	-35.6(3)

[a] UB3LYP/6-311G(d,p). [b] UB3LYP/cc-pVTZ [c] unpublished work by Percival et al.
[d] Obtained by TF-μSR at -9°C.

Mu addition to pyrrole in the pyrrole-methane hydrate and pure liquid produces two types of radicals. These are shown as **2** and **3** in Scheme 5.2. The Fourier power TF-μSR spectra are shown in Figure 5.5; liquid pyrrole in the top and pyrrole-methane hydrate in the bottom. As mentioned in Table 5.2, the muon hyperfine constants are 435.4 and 563.1 MHz for radicals **3** and **2** in the liquid and 446.4 and 567.7 MHz in the hydrate respectively. The hfcs determined from μ-LCR spectra as well as the calculated hfcs are summarized in Tables 5.7 and 5.8. The μ-LCR spectra in the liquid and hydrate are shown in Figures 5.6 and 5.7 respectively.

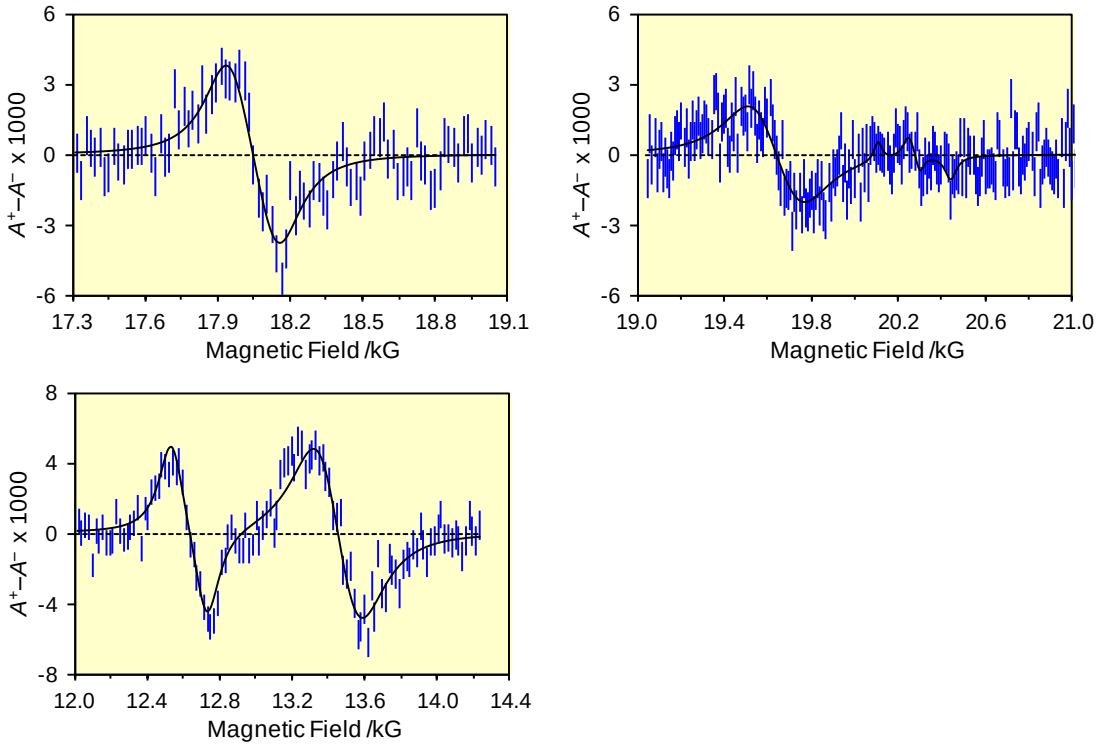

Figure 5.4: μ-LCR spectra obtained from the clathrate hydrate of thiophene-xenon at -30°C. The resonances arise from two different radicals 4 and 5 and are assigned as shown in Table 5.5.

As can be seen from Table 5.7, the β-C**H**Mu resonance was obtained for radical **2**, β-C**H**Mu, α-C**H**s and β-N**H** resonances for radical **3** in liquid pyrrole at -10°C. We haven't seen **N** and β-N**H** resonances for radical **2** because they both have very small

hfcs and small predicted amplitudes. The Boltzmann weighted average calculated hfc of **N** in radical **3** is 13.4 MHz by EPRII basis set and 11.2 MHz by 6-311G(d,p) basis set at 200 K but we haven't scanned the magnetic field low enough to see the signal. The β-N**H** resonance was seen as a small, narrow signal for radical **3** in the liquid with the hfc of 18.4 MHz at 22.3 kG (Figure 5.6 b). However, it wasn't detected in the hydrate. The μ-LCR peaks are generally broader in the hydrate, Figure 5.7, so the β-N**H** resonance may be too small to be seen in the hydrate although it may appear as a tiny signal at a magnetic field of 23 kG that coincides with the β-C**H**Mu resonance of radical **2** in the hydrate (Figure 5.7 e). Except for the β-N**H** resonance, the rest of the resonances which were seen in the liquid were also detected in the hydrate in addition to the extra signals, ΔM=1 resonances from which the muon hfcs were obtained. They are in good agreement with the muon hfcs determined from the TF-μSR spectra in Table 5.1.

The experimental hfcs are compared with the computed ones in Table 5.8. The hfcs were calculated by UB3LYP method and 6-311G(d,p) or EPRII basis sets. The results are similar using the two basis sets, second and third columns in Table 5.8, except for the β-N**H** atom for which the EPRII basis set predicts the hfc of 17.1 MHz that is closer to the experimental hfc of 18.4 MHz in the liquid.

It is obvious from Figure 5.5 that radical **3** has much higher amplitude than **2**. The ratio of radical amplitudes of **3** to **2** are 4.3(6) in the liquid and 4.3(7) in the hydrate which demonstrates that radical **3** is the more stable radical product. This is in agreement with the DFT calculation which showed that radical **3** is 38 kJ/mol more stable than **2** as the radicals were optimized by UB3LYP method and 6-311G(d,p) or EPRII basis sets. The EPR spectrum of irradiated pyrrole in adamantane matrix examined at 260 K mainly produced an allylic radical with H atom addition at the C_2 or C_5 position of the ring (protiated equivalent of radical **3** in Scheme 5.2) which is consistent with our result.[157] Having the same ratio of radical amplitudes in liquid and hydrate may be because of the extra N-H bond in pyrrole which doesn't exist in furan and thiophene. In liquid pyrrole, the N-H bond of one molecule points toward and is perpendicular to the plane of an adjacent molecule so that there is hydrogen bonding between the molecules.[158] Energy dispersive X-ray diffraction as well as molecular dynamics simulation has shown a complex aggregate of dimers oscillating between T-shape and stacked form with an

average population of 50% each in liquid pyrrole at 25°C.[159] In the hydrate, it is possible to have hydrogen bonding between the N-H of pyrrole and the cage water molecules such as the guest-host hydrogen bonds between the amine nitrogen and water H atoms or amine hydrogen and water O atoms in t-butylamine-Xe hydrate.[160]

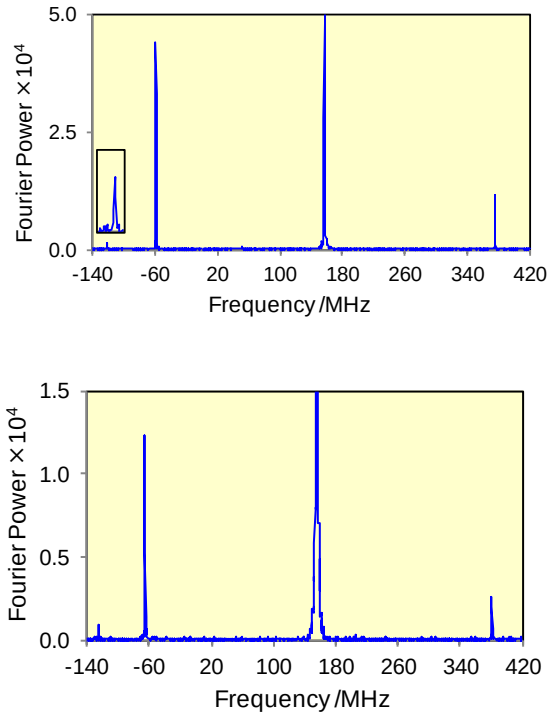

Figure 5.5: Fourier power TF-μSR spectra obtained from radicals 2 and 3 with the muon hfcs of 563 and 435 MHz respectively in pyrrole liquid at 11.6 kG and -9°C (top), pyrrole-methane hydrate at 11.5 kG and -73°C (bottom). The peaks at 157 MHz and 156 MHz are the diamagnetic signals in the liquid and hydrate respectively. The upper precession frequency of radical 2 was not discernible among the noise. The inset at the top figure shows the signal at -122 MHz which has been increased 10 times.

In terms of H-bonding activity, pyrrole hydrate comes first since both N and H of the N-H bond in pyrrole can make H-bonding with the cage water atoms. In the case of t-butylamine-Xe hydrate where the amine is trapped in the large cage of structure II hydrate (such as pyrrole), the amine nitrogen makes strong H-bonding with the water hydrogen of the cage at 90 K and tether the guest to a specific site in the cage. There is

also H-bonding between amine hydrogen and oxygen atoms of the cage water where the H-bonded water molecule is pulled inwards from its ideal lattice position in the structure II large cage.[160] So the N-H bond can act both as a proton donor and proton acceptor (two available sites for H-bonding). In the ammonia hydrate, the ammonia

Table 5.7: Muon and proton hyperfine constants determined from the μ-LCR spectra of radicals 2 and 3 detected in liquid pyrrole at -10°C and its clathrate hydrate at −73°C

sample	B_{LCR} /kG	Δ*M*	hfc /MHz	radical	assignment
liquid	22.670(12)	0	139.2(2)	**2**	β-C**H**Mu
liquid	17.495(3)	0	108.3(1)	**3**	β-C**H**Mu
liquid	25.155(2)	0	-33.6(1)	**3**	α-C**H**
liquid	25.041(4)	0	-31.5(1)	**3**	α-C**H**
liquid	22.346(12)	0	18.4(2)	**3**	β-N**H**
hydrate	20.851(8)	1	568.0(2)	**2**	muon
hydrate	23.028(9)	0	137.2(2)	**2**	β-C**H**Mu
hydrate	16.384(2)	1	446.3(1)	**3**	muon
hydrate	18.185(3)	0	106.5(1)	**3**	β-C**H**Mu
hydrate	25.762(10)	0	-33.9(2)	**3**	α-C**H**
hydrate	25.649(8)	0	-31.8(2)	**3**	α-C**H**

Table 5.8: Computed hyperfine constants (MHz) for radicals 2 and 3 vibrationally averaged at −73°C compared with those determined by μ-LCR spectroscopy in liquid pyrrole at -10°C and the hydrate at −73°C

nucleus	A_{calc}[a]	A_{calc}[b]	A_{exp}(liq.)	A_{exp}(hydr.)
radical **2**				
muon	565.2	569.5	563.1(1)[c]	568.0(2)
β-C**H**Mu	149.2	151.5	139.2(2)	137.2(2)
radical **3**				
muon	439.9	444.1	435.4(0)[c]	446.3(0)
β-C**H**Mu	111.3	112.9	108.3(1)	106.5(1)
α-C**H**	-34.0	-36.5	-33.6(0)	-33.9(2)
α-C**H**	-30.1	-31.9	-31.5(1)	-31.8(2)
β-N**H**	6.4	17.1	18.4(2)	

[a] UB3LYP/6-311G(d,p). [b] UB3LYP/EPR-II [c] Value obtained by TF-μSR at -9°C.

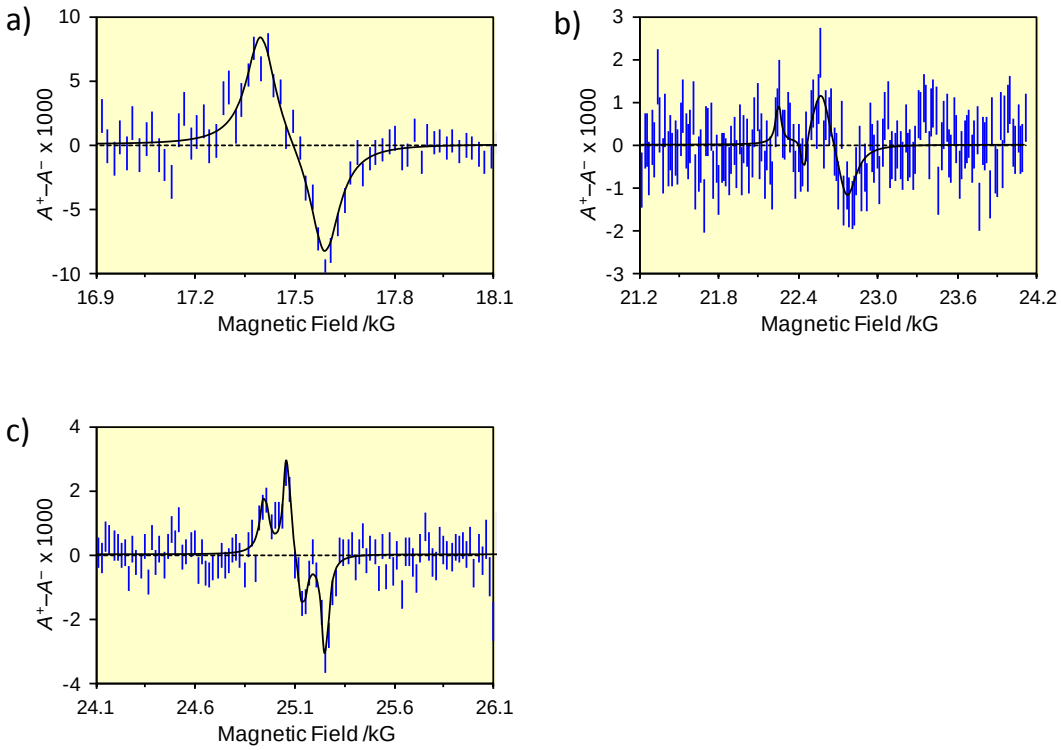

Figure 5.6: μ-LCR spectra obtained from liquid pyrrole at -10°C. The resonances arise from two different radicals 2 and 3 and are assigned as shown in Table 5.7.

molecule can replace the water of the cage and keep the H-bonding with the rest of the cage water molecules without mechanically destroying the cage.[161] In the case of THF hydrate, H-bonding was seen between the oxygen of the ether, guest and the hydrogens of the cage water and molecular dynamic simulation showed that the percentage of hydrogen bonding increased when temperature was raised from 183 to 263 K.[140] So furan and dihydrofuran hydrates can experience the same environment. It seems unlikely for S atom in thiophene to have any H-bonding with the cage water atoms. In the case where H_2S is trapped in the small cage of structure I hydrate, hydrogen bonding was seen between the Hs and the oxygen of the water but not between the S atom and the Hs of the cage water.[162] Even if there is no H-bonding between the guest and the cage, there is still some barrier to guest rotation inside the cage which comes from the Van der Waals interactions between the guest and the host and depends on various

proton configuration of the water molecules that make up the cage, symmetry of the cage and the sizes of the guest and the cage.[163]

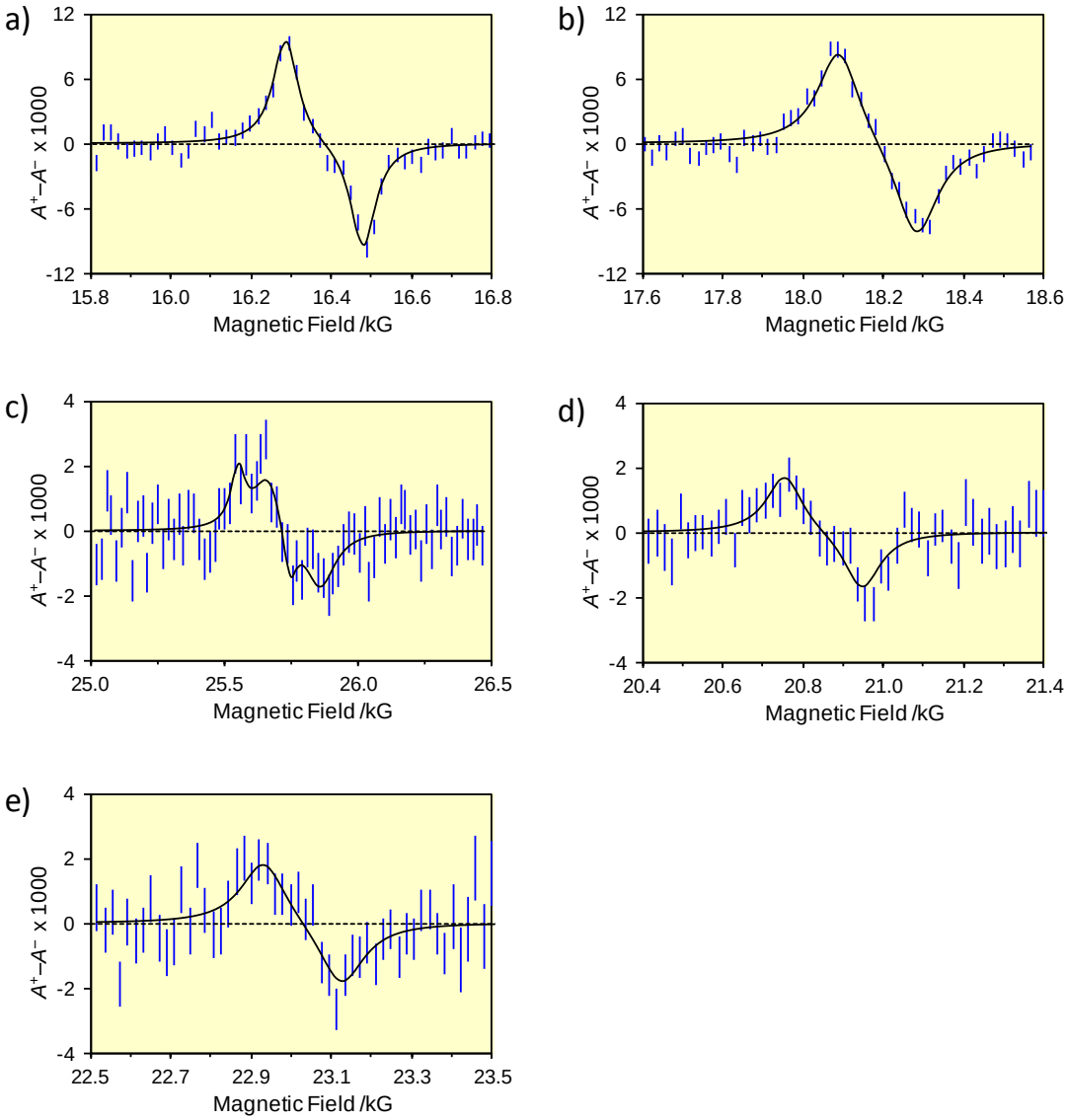

Figure 5.7: **μ-LCR spectra obtained from pyrrole hydrate at -73°C. The resonances arise from two different radicals 2 and 3 and are assigned as shown in Table 5.7.**

5.3. Conclusions

Muoniated radicals of isoxazole, thiophene and pyrrole were characterized by means of muon spin spectroscopy in the liquid and clathrate hydrate. Only one type of radical was seen in the case of isoxazole, radical **1a** among the four possibilities shown in Scheme 5.1, where the unpaired electron is delocalized over C4-C3-N and is the more stable radical according to the calculation results. Muonium addition to thiophene led to radicals **4** and **5**. Radical **5** is the major radical product showing that Mu addition at the C2 or C5 position of the ring is preferred over the C3 position, both in liquid and hydrate. When muonium adds to pyrrole, two types of radicals were formed: radicals **2** and **3** with radical **3** being dominant showing that Mu addition at the C2 or C5 position of the ring is again the preferred side of addition. However, the ratio of radical amplitudes is equal in the liquid and hydrate in this case. This could be because of the H-bonding ability of the extra N-**H** bond that doesn't exist in furan and thiophene. Computed hfcs with 6-311G(d,p) and EPRII basis sets produce values similar to the experimental hfcs except for radical **4** in thiophene where cc-pVTZ basis set gives better results. The extra ΔM=1 resonance seen in the hydrate is consistent with our previous results showing that the radical mobility is hindered in the hydrate compared to the liquid phase which may be attributed to the H-bonding capability of the guest. The H-bonding for guests with N or O atom is evident from literature but there still is a barrier to rotation for the guest inside the cage even in the case that there is no H-bonding.

Chapter 6.

Muonium and the muoniated free radicals in the hydrates of acetone and benzene-xenon

6.1. Introduction

Muonium and muoniated free radicals were observed in the hydrates of acetone, acetone-d6/ D_2O and benzene-xenon. The TF-μSR and the μ-LCR experiments were done at different temperatures and various information can be extracted from the temperature dependence of the data. The reason for choosing acetone hydrate is that acetone is acyclic unlike the cyclic molecules that were studied in previous chapters. The acetone-d6/ D_2O hydrate was chosen because the ΔM=1 and ΔM=0 resonances overlap in the muoniated radical in acetone while in the deuteriated form the two resonances appear at different places. The hfcs of the $(CH_3)_2COMu$ radical studied in the liquid phase showed strong temperature dependence which was attributed to facile rotation about the C-O bond. It is interesting to see how enclathration affects the radical behavior. Also, Mu addition to a C=O bond is much slower than to C=C bond. Does the radical form fast enough to be observed in TF-μSR? A strong TF-μSR signal is not enough to prove Mu addition since ionic mechanisms have been proposed for $(CH_3)_2COMu$ radical formation.[164] μ-LCR experiments are necessary to comment on the mechanism of radical formation.

6.2. Results and discussion

6.2.1. Observations of $(CH_3)_2COMu$ and $(CD_3)_2COMu$ radicals

Mu adds to acetone or acetone-d6 in the hydrates to form the muoniated radicals as shown in Scheme 6.1. The muon hyperfine coupling constant was measured at 180-250 and 120-250 K temperature ranges for the radicals in acetone and acetone-d6 hydrates respectively. Tables 6.1 and 6.2 include the data for $(CH_3)_2COMu$ and $(CD_3)_2COMu$ radicals respectively. A plot of A_μ vs. temperature of the TF-μSR data is in Figure 6.1. It is known from the literature that acetone forms a muoniated radical when Mu adds to the O atom of the carbonyl group in the keto form of acetone.[164,7] In superheated water, above 250°C, Mu will add to the enol form of acetone which makes a radical with a much higher hfc as reported by Ghandi and Brodovitch et al.[165,166] Only the former case is happening in the hydrate in all the temperatures studied, i.e. the **2**-muoxyprop-**2**-yl radical (Scheme 6.1) is formed. Also, the experimental and calculated muon hfc values in the clathrates are compared with the radical in aqueous solutions in Figure 6.1. The red data points refer to 0.69 and 0.29 mole fractions of acetone in water at different pressures and temperatures reported by Ghandi et al.[165] The green points refer to the 20:1 acetone to water mixture (0.8 mole fraction of acetone in water) at various temperatures reported by Buttar et al.[167] The muon hfcs are larger in the clathrate compared to the aqueous solutions. Hill et al. proposed that when the radical is in aqueous solution, it can undergo H-bonding with the water molecules, which is known to reduce the hfc.[164] However, in the hydrate there is less probability of H-bonding with the cage wall. The ^{13}C chemical shift of the carbonyl group of acetone in the hydrate decreases compared to the molecule in the solution showing that hydrate formation reduces the interaction between the acetone and the water according to the experimental data of Takebayashi et al.[168] Optimizing the radical inside the cage using the UB3LYP method, 6-31g(d) basis set and GD3BJ keyword (to take dispersion interactions into account) and anharmonic frequency calculation, gave the muon hfcs shown in Figure 6.1. According to Oba et al., the calculated muon hfc at 150 K in vacuum is 91.6 MHz by density functional path integral molecular dynamics simulation.[169] They have commented that because of the large zero- point vibrational fluctuation of the Mu-O stretching coordinate, Mu can partially dissociate from acetone in

vacuum and the hfc increases since the spin density on Mu increases. On the other hand when a water molecule approaches the muoniated acetone radical, the configuration becomes an ionic dissociation instead of a neutral dissociation, which decreases the spin density on Mu and so the hfc decreases in solution.[169] It looks as if the situation in the hydrate is intermediate between vacuum and solution.

Rhodes et al. studied the $(CH_3)_2COMu$ radical in the NaX zeolite at room temperature, and showed that it has a strong interaction with the zeolite surface. The TF-μSR radical signals are quite broad indicating that the radicals are immobilized in the zeolite.[170] That is not the case for the radical in the hydrate (Figure 6.2). In general, the hfc increases as the temperature is raised for the $(CH_3)_2COMu$ radical in the hydrate and aqueous solutions. It is known that two factors contribute to the magnitude of the hyperfine coupling constant: the σ-π exchange polarization of the O-Mu σ-bonding electrons, which leads to negative spin density on the muon; secondly the hyperconjugation between the s orbital of muonium and the π orbital of the carbon that increases the spin density on the muon.[171]

Scheme 6.1: Muonium addition to acetone

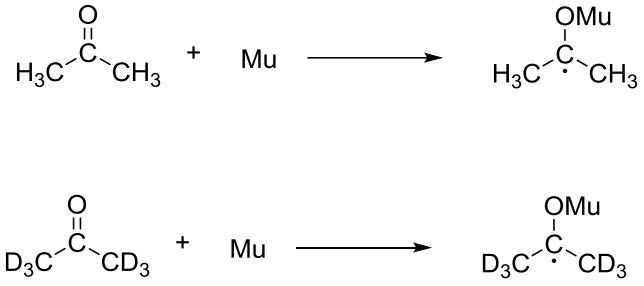

Table 6.1: A_μ for $(CH_3)_2COMu$ radical determined from TF-μSR and μ-LCR and calculation[a]

Temperature /K	A_μ /MHz from TF-μSR	A_μ /MHz from μ-LCR	A_μ /MHz from calculation
120			19.4
160			23.6
180	29.9(2)	30.0(1)	25.7
200	31.2(3)	31.0(1)	27.9
220	32.9(4)	32.2(1)	30.1
225	33.4(1)		
230	33.0(5)		
250	34.5(2)		33.3

[a] The radical was optimized inside the cage by UB3LYP method, 6-31g(d) basis set and GD3BJ keyword and anharmonic frequencies were calculated by Freq=anharmonic,Readanharm at various temperatures

Table 6.2: A_μ for $(CD_3)_2COMu$ radical determined from TF-μSR and μ-LCR

Temperature /K	A_μ /MHz from TF-μSR	A_μ /MHz from μ-LCR
120		25.9(2)
160	28.4(3)	28.7(1)
180	29.6(3)	29.7(1)
200	30.9(2)	30.8(1)
220	32.4(1)	32.1(1)
230	33.7(2)	
250	34.7(1)	34.3(1)

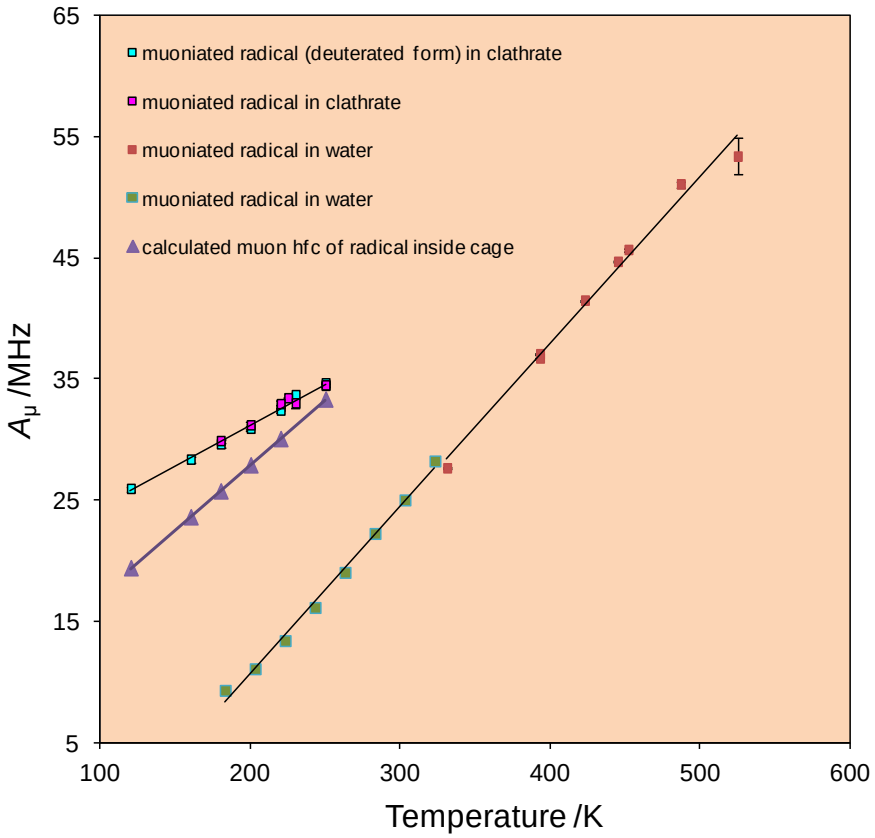

Figure 6.1: **Muon hfcs from TF-μSR (except at 120 K) versus temperature for $(CH_3)_2COMu$ and $(CD_3)_2COMu$ radicals in the clathrates compared with literature data[165,167] of the $(CH_3)_2COMu$ radical in various aqueous solutions and calculation. The error bars are smaller than the size of data points in the clathrates.**

Figure 6.2 shows the TF-μSR spectra of the radical in acetone hydrate at 250 and 220 K. The radical signals become broader at lower temperatures while they are sharper for the radical in acetone-d6 hydrate at the same temperature. The latter is shown in Figure 6.3. When D is replaced with H (as in the case acetone-d6 hydrate), the relaxation rate is reduced and hence the narrower line width is observed which leads to the longer lived signals and as a result a more precise hfc is obtained.

Muonium was observed at 100, 130 and 230 K in acetone-d6 hydrate. At 180 K, both radical signals and muonium were observed but as the temperature is raised the

muonium signal amplitude decreases while the radical signal increases. This is shown in Figures 6.4 and 6.5 and the relevant data are in Table 6.3.

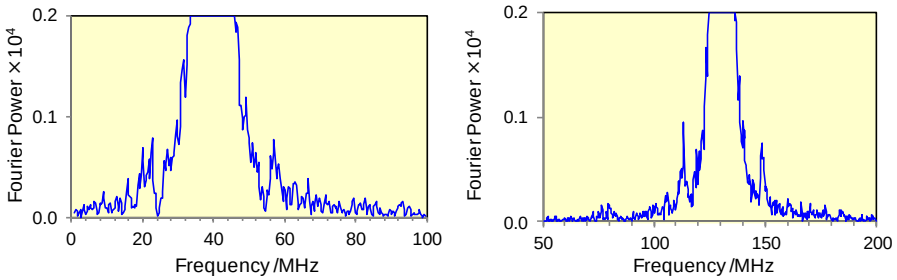

Figure 6.2: Fourier power TF-μSR spectra obtained from $(CH_3)_2COMu$ radical at 220 K(left) and 250 K (right) with the muon hfcs of 32.9 and 34.5 MHz respectively.

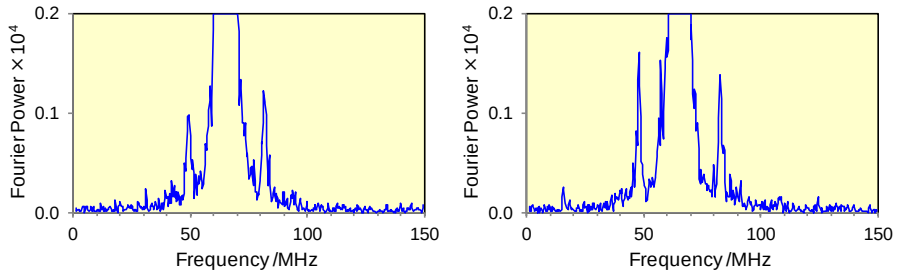

Figure 6.3: Fourier power TF-μSR spectra obtained from $(CD_3)_2COMu$ radical at 220 K(left) and 250 K (right) with the muon hfcs of 32.4 and 34.7 MHz respectively.

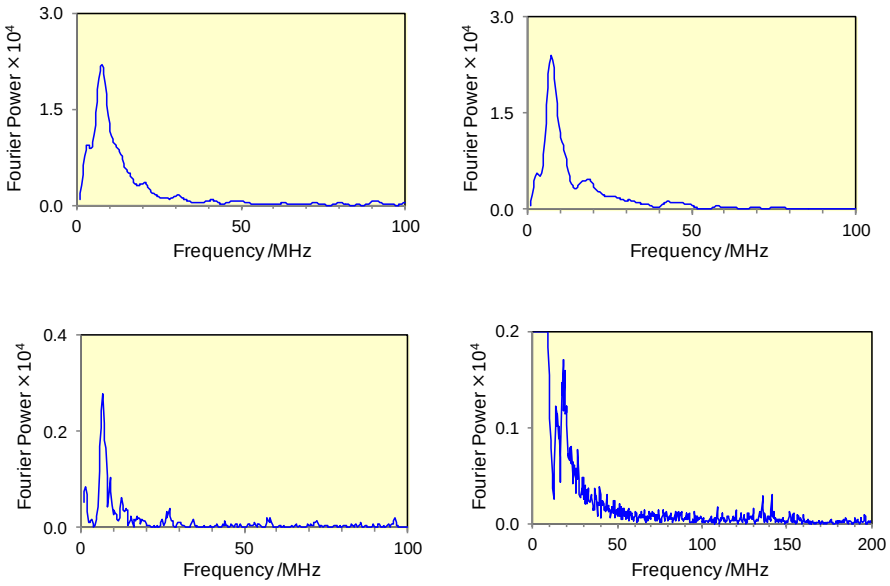

Figure 6.4: **Fourier power TF-μSR spectra obtained from muonium (upper left) at 100 K, 130 K (upper right) and 230 K (lower left) in acetone-d6 hydrate. Both muonium and the radical signals were seen at 180 K (lower right). The radical signals appear at 12 and 17.5 MHz. The muonium signals are at 135 and 140.8 MHz at the field of 104.8 G.**

Table 6.3: **Muonium and radical amplitudes (v_{R1}) at various fields and temperatures in acetone-d6 hydrate from TF-μSR**

T /K	Field /G	Mu frequency /MHz	Mu amplitude	Radical amplitude (v_{R1})
100	5.3(4)	7.4(5)	0.077(6)	
130	4.9(2)	6.9(3)	0.051(4)	
160	104.5(1)			0.012(2)
180	104.8(1)			0.015(2)
200	104.9(1)			0.020(2)
220	104.9(1)			0.014(1)
230	4.9(1)	6.8(1)	0.042(3)	
230	104.9(1)			0.017(2)
250	105.2(1)			0.015(2)

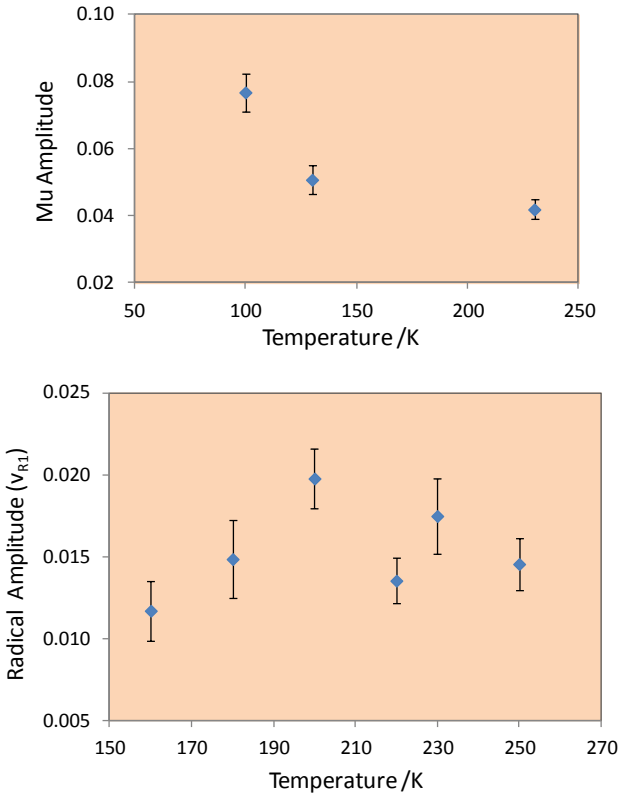

Figure 6.5: Temperature dependence of muonium and radical signal amplitudes of $(CD_3)_2COMu$ in the acetone-d6 hydrate.

μ-LCR spectra are shown in Figures 6.6 and 6.7. The Δ*M*=0 and the Δ*M*=1 resonances are seen both for $(CH_3)_2COMu$ and $(CD_3)_2COMu$ radicals. The relevant data are presented in Tables 6.4 and 6.5. The Δ*M*=1 resonances appear at almost the same place for both radicals but the Δ*M*=0 resonances become visible at quite different fields because the deuteron to proton magnetic moment ratio is 0.307.[172]

The fact that we see both Mu and the radical simultaneously is an interesting result. In order to see the radical in TF-μSR, Mu must react with the guest molecule fast enough (the reaction rate in excess of 10^9 s^{-1}) but we see Mu itself when the reaction is slow. When we see both Mu and radical it means they are kept separately. An example is the detection of Mu and the muoniated free radical in the C_{60} powder by Percival et al.[173,174] Endohedral Mu was characterized with a hfc of 4316 MHz, close to the vacuum value and the exohedral muonium adduct ($C_{60}Mu$) with the hfc of 324 MHz which is

typical for a carbon centered radical. In the hydrate both Mu and the radical were detected simultaneously as well with the difference that the cage walls (water molecules) are unreactive in hydrate so Mu either reacts with the guest molecule inside the cage or can be trapped as Mu inside an empty cage.

The relative signal amplitudes from μ-LCR spectra are shown in Figure 6.8 and the related data are in Table 6.6. The fact that the Mu signal amplitude is decreasing and the radical signal amplitude is increasing as the temperature is raised could mean that Mu is diffusing from the small cage to the large cage where it reacts to form a radical. If Mu stops in the large cage with the guest, it forms a radical immediately. The data look like an S shape curve. The probability of Mu decaying in the small cage (*P*) is $e^{-\lambda t}$ where $\lambda = Ae^{-Ea/RT}$. The probability of Mu reaching the large cage is 1-*P* which needs to be multiplied by $(1/\tau)\ e^{-t/\tau}$ to account for the muon lifetime. Integrating the function from 0 to infinity and substituting for λ leads to the following equation:

$$P(\mathrm{Mu} \rightarrow \mathrm{R}) = \frac{\tau A\, e^{-Ea/RT}}{\tau A\, e^{-Ea/RT} + 1} \qquad (6.1)$$

where τ is the muon lifetime (2.2 μs), *A* is the pre-exponential factor, *E*a is the activation energy of Mu diffusing from the small cage to the large cage and *R* is the gas constant. In order to solve for *E*a, the lower and upper bounds of *A* (1.5 and 3×10^{12} s^{-1}) were taken from a reference.[76] A correction was done for the rattling frequency of Mu by taking into account the mass ratio so that 4.5 and 9×10^{12} s^{-1} were used for *A* which leads to the activation energy of 26 and 27 kJ/mol respectively. This is slightly less than 34 kJ/mol which is the calculated value for H atom.[151]

According to Kobayashi et al., isobutyl radical in a large cage withdraws H atom from an isobutane molecule in the adjacent cage (through the hexagonal face) in the γ-ray irradiated isobutane/ D_2O hydrate.[126] Depending on whether the H atom is transferred from the C1 or C2 atom of isobutane molecule, isobutyl radical or t-butyl radical is formed. Annealing experiments at 245 K and 260 K showed that the amount of isobutyl radicals decreased while the t-butyl radicals increased but the total amount of radicals remained constant. Sugahara et al. reported a similar experiment with the methane+propane mixed structure II hydrate where methyl radical in the small cage

withdraws an H atom from the propane molecule in the adjacent cage.[72] In this case the hydrogen picking phenomenon is happening through the pentagonal face between the small and large cages. H transfer between the propyl radical and the adjacent propane molecule through the hexagonal face of large cages has been observed in the γ-ray irradiated propane hydrate by Ohgaki et al.[71] One dimensional energy barriers for H atom migration through the pentagonal and hexagonal faces of small and large cages in the structure II hydrate were calculated by Alavi et al. to be 62 and 17 kJ/mol respectively at the MP2 level.[76] The barrier for the diffusion of the H radical from the small cage was estimated to be 34 kJ/mol by DFT calculations with D3 empirical dispersion correction according to Liu et al.[151] It makes sense for Mu to have smaller energy barrier compared to H radical because the rattling frequency is higher for Mu (Mu has a lighter mass compared to H). In our experiments using 5.88 mol % of organic liquid in water, one assumes that all the organic molecules are incorporated in the large cages of the structure II hydrate with the small cages being empty. If Mu is formed in the small cage, it can diffuse from the small cage to the large cage through the pentagonal face and form the radical. Figure 6.9 shows this qualitatively.

Table 6.4: Muon and proton hfcs determined from the μ-LCR spectra of $(CH_3)_2COMu$ radical

T /K	B_{LCR} /kG	ΔM	hfc /MHz	assignment
180	1.101(3)	1	30.0(1)	muon
200	1.140(4)	1	31.0(1)	muon
220	1.182(3)	1	32.2(1)	muon
180	1.387(7)	0	55.4(2)	β-CH_3
200	1.343(10)	0	55.9(3)	β-CH_3
220	1.339(7)	0	57.5(4)	β-CH_3

Table 6.5: Muon and deuterium hfcs determined from the μ-LCR spectra of $(CD_3)_2COMu$ radical

T /K	B_{LCR} /kG	Δ*M*	hfc /MHz	assignment
120	0.952(7)	1	25.9(2)	muon
160	1.054(3)	1	28.7(1)	muon
180	1.090(2)	1	29.7(1)	muon
200	1.129(2)	1	30.8(1)	muon
220	1.179(2)	1	32.1(1)	muon
250	1.258(2)	1	34.3(1)	muon
120	0.709(41)	0	7.5(8)	β-C**D**$_3$
160	0.813(20)	0	7.2(4)	β-C**D**$_3$
180	0.842(16)	0	7.7(4)	β-C**D**$_3$
200	0.843(12)	0	9.0(3)	β-C**D**$_3$
220	0.914(16)	0	8.9(3)	β-C**D**$_3$
250	1.026(17)	0	7.8(3)	β-C**D**$_3$

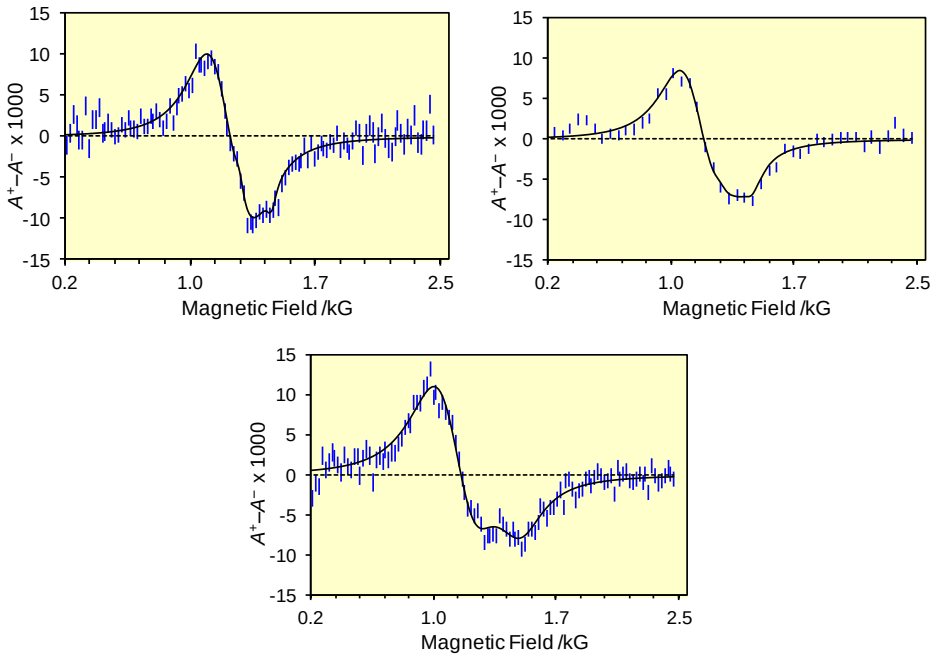

Figure 6.6: μ-LCR spectra of $(CH_3)_2COMu$ radical at 220 K(top left), 200 K (top right) and 180 K at the bottom.

Table 6.6: Relative μ-LCR amplitudes at various temperatures

T /K	Relative amplitude	Relative error	fit
120	0.76	0.02	0.76
160	0.77	0.02	0.77
180	0.79	0.02	0.82
200	0.94	0.02	0.91
220	0.98	0.02	0.97
250	1	0.01	0.99

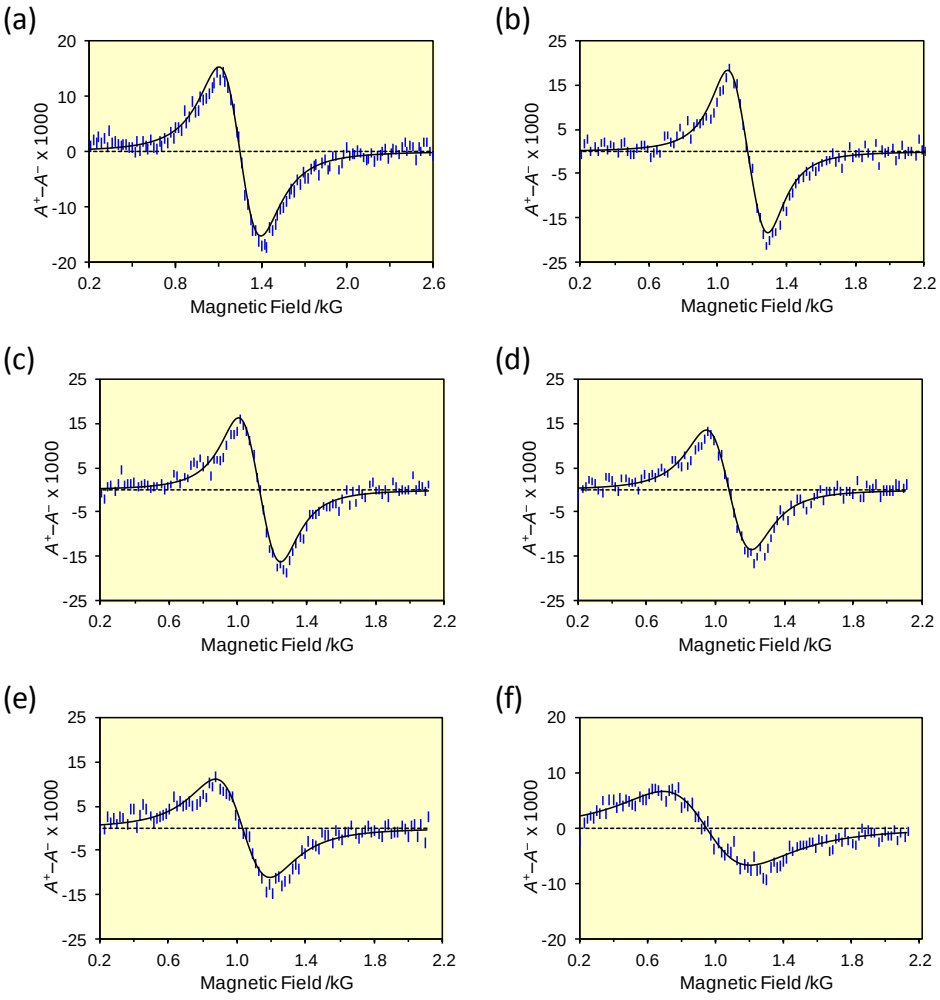

Figure 6.7: μ-LCR spectra of $(CD_3)_2COMu$ radical at a) 250 K, b) 220 K, c) 200 K, d) 180 K, e) 160 K and f) 120 K.

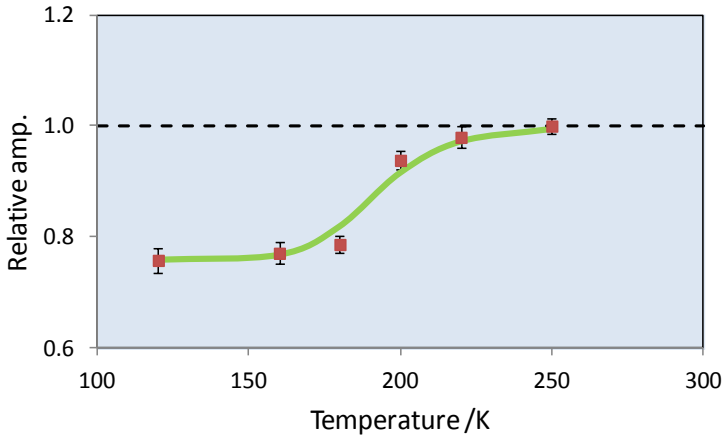

Figure 6.8: **Relative μ-LCR amplitude vs temperature. The curve through the points is a best fit to the model described by equation 6.1.**

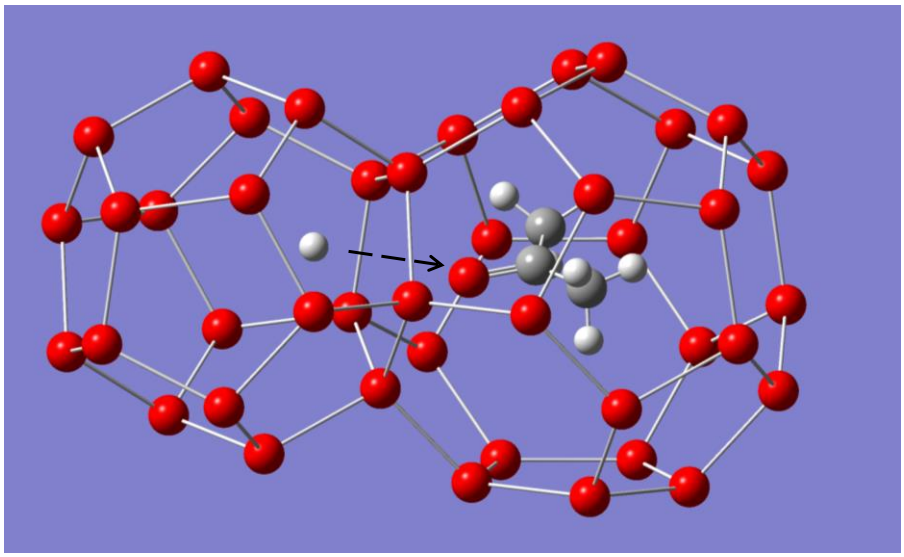

Figure 6.9: **Schematic representation of Mu transport from the small cage to the large cage in the acetone-d6 hydrate.**

6.2.2. Observation of muoniated cyclohexadienyl radical

Mu adds to the benzene ring to produce the muoniated cyclohexadienyl radical as shown in Scheme 6.2. Muon hfcs of the radical were obtained from TF-μSR at different temperatures in the benzene-xenon hydrate and the data is presented in Table 6.7. The data were obtained in different beam periods and the weighted least squares linear fit was done to the combined data set to extrapolate the muon hfcs at lower temperatures. Figure 6.10 shows the data. The muon hfcs decrease as the temperature increases. The slope, $dA_{\mu'}/dT$ is -0.021 MHz in the hydrate where $A_{\mu'}=A_{\mu}/3.1833$ which corrects for the ratio of muon and proton magnetic moments. Similarly the slope in the bulk benzene studied by Yu et al is -0.025 MHz/ °C.[175] An example of a TF-μSR spectrum displaying signals of the C_6H_6Mu radical with muon hfc of 527.5 MHz at 235 K is shown in Figure 6.11.

Scheme 6.2: Muonium addition to benzene

Table 6.7: A_μ for C_6H_6Mu from TF-μSR

Temperature /K	A_μ /MHz from TF-μSR	A_μ /MHz from the fit
110		535.4
120		534.7
140		533.3
160	532.1(7)	532.0
180	531.3(6)	530.7
200	529.5(4)	529.3
220	527.8(3)	528.0
235	527.5(2)	527.0
245	526.1(6)	526.3
255	526.8(5)	525.7
260	526.1(5)	525.3

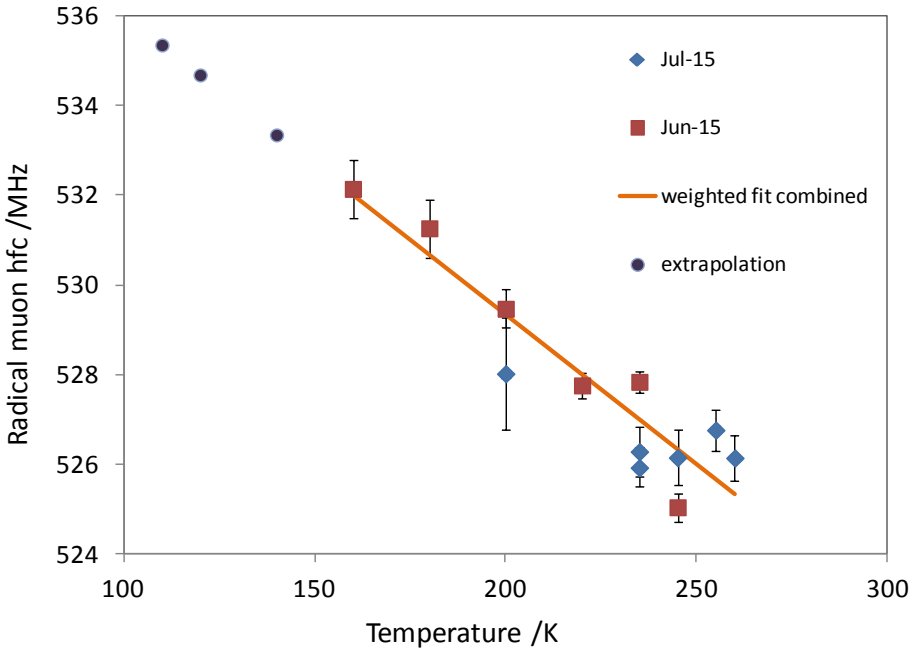

Figure 6.10: **The temperature dependence of the muon hfcs for C_6H_6Mu radical in hydrate. The red and blue points are from two different beam periods. The line going through the points is the combined weighted least squares linear fit. The three points at 110, 120 and 140 K are extrapolated from the fit.**

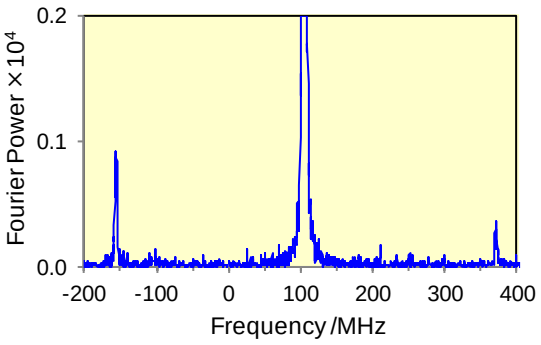

Figure 6.11: **Fourier power TF-μSR spectrum obtained from C_6H_6Mu radical with the muon hfc of 527.5 MHz at 235 K. The peak at 105 MHz is the diamagnetic signal. The radical peaks are at -155.7 and 371.8 MHz.**

Mu was also detected at various temperatures by TF-μSR and the Mu hfcs were extracted by means of equations 1.11 and 1.12. Figure 6.12 and Table 6.8 include the data. It is seen that Mu hfc is almost constant as the temperature increases from 150 to 235 K with the average value close to the vacuum value (4463 MHz).

Table 6.8: Mu hfc from TF-μSR

Temperature /K	A_{Mu} /MHz from TF-μSR
150	4555(182)
180	4431(124)
200	4515(45)
235	4483(32)

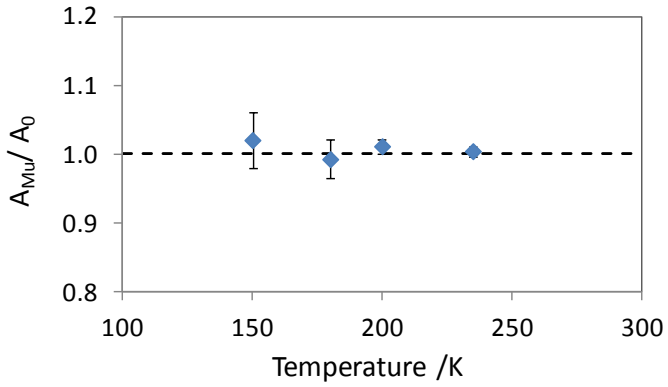

Figure 6.12: Temperature dependence of Mu hfc divided by the vacuum value (4463 MHz) in the benzene-xenon hydrate.

The amplitude of Mu (v_{12}) is plotted in Figure 6.13. The amplitude decreases as temperature increases, unlike the radical amplitude (v_{R1}), which increases as the temperature increases (Figure 6.14). The relevant data is in Table 6.9.

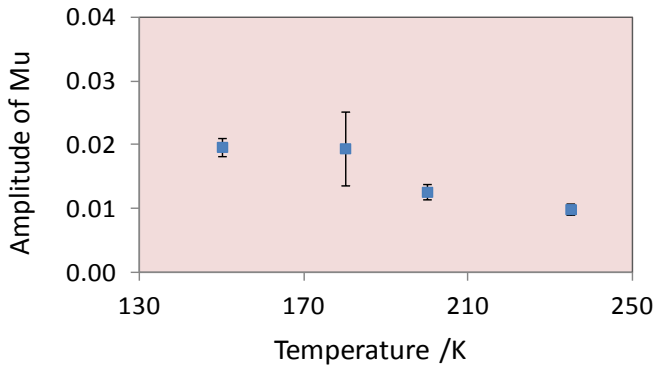

Figure 6.13: Mu amplitude (v_{12}) in the benzene-xenon hydrate vs temperature.

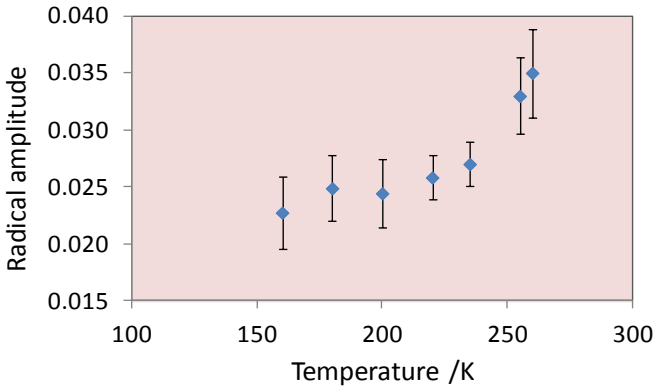

Figure 6.14: Radical amplitude (v_{R1}) in the benzene-xenon hydrate vs temperature from TF-μSR.

Table 6.9: Mu and radical amplitude vs temperature

T /K	Mu amplitude (v_{12})	Radical amplitude (v_{R1})
150	0.020(1)	
160		0.023(3)
180	0.019(6)	0.025(3)
200	0.013(1)	0.024(3)
220		0.026(2)
235	0.010(1)	0.027(2)
255		0.033(3)
260		0.035(4)

The radical amplitude increases slowly from 160 to 235 K and suddenly rises from 235 to 260 K. On the other hand, the Mu amplitude decreases from 150 to 235 K. This could mean that Mu at 235 K transfers from the small cage to the large cage and forms the radical in the large cage. Unlike the case of acetone hydrate, where the guest has an O atom capable of H-bonding with the cage water, in benzene-xenon hydrate the large cages are filled with benzene molecules which are non-polar. It is known from literature that oxygen containing guest molecules form hydrogen bonds with the water framework of the cage which leads to the formation of Bjerrum L-defects in the cage.[160,154] These defects are known to open the face of the cages temporarily and facilitate the diffusion of the small guests.[176] Also, in acetone hydrate, the water reorientational correlation time at 233 K is 0.57 μs while for SF_6 hydrate (a non-polar guest) is 780 μs. The activation energy for water reorientation is 27 and 51 kJ/mole in acetone and SF_6 hydrates respectively.[177] So, the reorientation of water molecules in acetone hydrate is more than a thousand times faster than in SF_6 hydrate and the activation energy for water molecule reorientation in SF_6 hydrate is almost double that in acetone hydrate. This may be why Mu diffuses at a higher temperature, 235 K in benzene-xenon hydrate compared to the acetone hydrate where Mu diffuses at 180 K.

μ-LCR spectra of benzene-xenon hydrate at various temperatures gave powder pattern shape ΔM=1 resonances. An example is shown in Figure 6.15. In order to fit this type of signal it would be necessary to have a specific program with a powder line shape function such as described by Roduner et al.[178] Not having access to this program, I qualitatively compared the shape of the ΔM=1 resonances with the top spectrum of Figure 1 in Roduner's paper where various powder pattern line shapes were simulated in the paper.[179] The shape of the signal (Figure 6.15) is like Roduner's static case. However, the ΔM=0 resonances for the C**H**Mu signal as in Figure 6.16 have a symmetrical Lorentzian shape. The muon hfcs from TF-μSR were used to extract the proton hfcs (A_H) in the methylene group of C_6H_6Mu radical using equation 1.23. The results are summarized in Table 6.10.

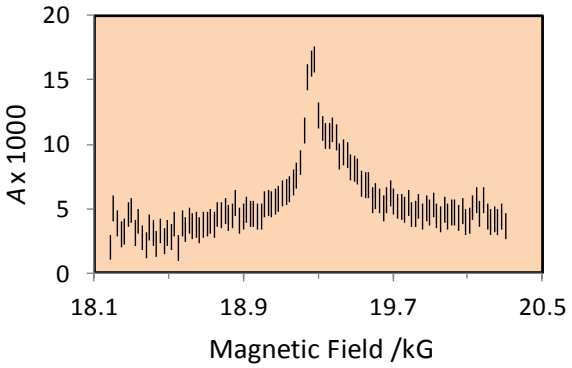

Figure 6.15: μ-LCR spectrum for Δ*M*=1 resonance of C_6H_6Mu radical at 235 K.

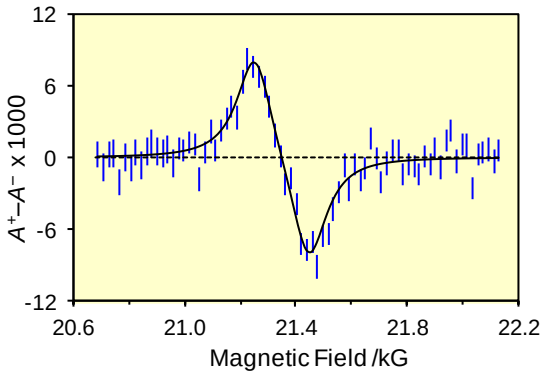

Figure 6.16: μ-LCR spectrum for β-CHMu resonance of C_6H_6Mu radical at 235 K.

Table 6.10: Proton hfcs determined from Δ*M*=0 resonance of β-CHMu

T /K	B_{LCR} /kG	hfc /MHz
110	21.659(5)	130.5[a]
120	21.648(6)	130.0[a]
140	21.609(4)	129.4[a]
160	21.570(3)	128.8(7)
200	21.470(3)	128.0(4)
235	21.348(3)	127.9(3)

[a] A_μ came from extrapolating TF-μSR data

A plot of A_H versus temperature is shown in Figure 6.17. The Proton hfcs decrease as temperature increases, which is similar to the trend in pure benzene. The muoniated cyclohexadienyl radical is known to have a planar structure in the pure phase, where the wagging motion of the C-H and C-Mu bonds in the methylene group are responsible for the variation of hfcs.[175] This is in contrast to the C_6H_6Mu radical in NaY zeolite environment, where the radical binds strongly to the cation and distorts from the planar geometry.[180,4] Various ΔM=1 resonances were seen in its μ-LCR spectra over a wide temperature range, which were related to two different orientations of C-Mu exo and endo with respect to the cation, leading to large shifts in hfcs.[180] In the hydrate, the temperature dependencies of A_μ (from TF-μSR) and A_p (from μ-LCR) of the methylene group show that the C_6H_6Mu radical behaves as in pure benzene. The ΔM=1 resonances from the μ-LCR spectra qualitatively look like the static case in a polycrystalline environment. Roduner et al. simulated a static powder-pattern shape ΔM=1 signal with an isotropic muon hfc value which is typical for the radical in the bulk benzene or unperturbed environment. [179,181] So similar behavior may be expected in the hydrate, but further investigation such as fitting the powder-pattern shape ΔM=1 resonances would be necessary to confirm that.

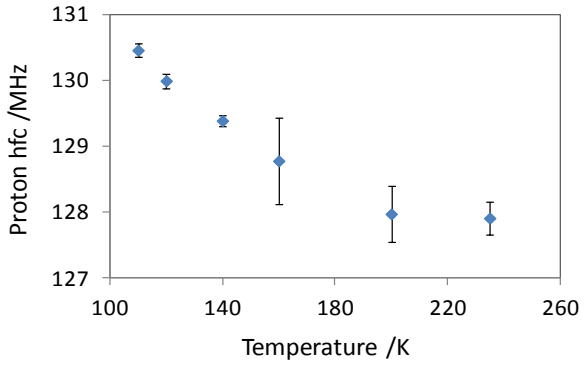

Figure 6.17: Proton hfcs of β-CHMu vs temperature in C_6H_6Mu radical. The error bars on the first 3 data points come from the errors in the μ-LCR fields only. The error depends on the error of A_μ as well but A_μ is extrapolated from the TF-μSR data in these cases.

6.3. Conclusions

Muonium and muoniated free radicals were observed simultaneously in the hydrates of acetone, acetone-d6/ D_2O and benzene-xenon. $(CH_3)_2COMu$, $(CD_3)_2COMu$ and C_6H_6Mu radicals were formed. In $(CH_3)_2COMu$ and $(CD_3)_2COMu$ radicals, muon adds to the C=O bond while in C_6H_6Mu radical, adds to the C=C bond. The muon hfcs of the muoniated acetone radical in the hydrate are much higher than in aqueous solutions and neat liquid but has the same trend: A_μ increases as temperature increases. The DFT calculation of the radical inside the cage is also consistent with the trend. The reason for larger muon hfcs in the hydrate compared to the aqueous solutions and liquid is related to less interaction of the radical with the cage wall and the H-bonding between the radical and the cage water molecules which slightly weakens the O-Mu bond, resulting in an increased length and consequent higher spin density on Mu. The situation in the hydrate is intermediate between vacuum and solution. The temperature dependence of the muon and proton hfcs in the methylene group of C_6H_6Mu radical in the hydrate behaves as in pure benzene. ΔM=1 resonances have a powder-pattern shape and fitting those signals will be left for future studies.

The Mu amplitude decreases and the radical amplitude increases with temperature in both acetone and benzene hydrates. This is an indication of Mu diffusing from the small cage to the large cage with the critical temperatures being 180 K and 235 K in the acetone and benzene hydrates respectively. Defects in the cage wall may play a role in Mu diffusion at a lower temperature in the acetone hydrate.

Chapter 7.

Summary and future suggestions

This thesis work was to use the muon spin resonance spectroscopy technique to characterize various organic free radicals in clathrate hydrates for the first time. Hydrates of cyclopentene, furan, 2,5- and 2,3-dihydrofuran, pyrrole, thiophene, isoxazole, benzene, acetone and isobutene were prepared. Hydrate formation was confirmed by either powder X-ray diffraction or solid state NMR.

Radicals were formed by Mu addition to the organic guests in the hydrates. Muon and other nuclei hfcs were determined from TF-μSR and μ-LCR in the hydrates and pure liquid. DFT calculations were used to guide the spectral assignments and distinguish between competing radical products where applicable as in the hydrates of furan, 2,3-dihydrofuran, pyrrole, thiophene and isoxazole. It was shown that an extra resonance, ΔM=1 is present in the hydrate which doesn't exist in the liquid. This resonance is an indication of anisotropy in the environment where the molecules do not tumble freely. From the ratio of signal amplitudes as well as DFT calculations, one can deduce which radical is the abundant radical product and so the reactivities of the addition sites will be determined. In the case of cyclopentene and 2,5-dihydrofuran, benzene and acetone where the molecules are symmetric, only one radical is formed. However, the radical structure is different in these hydrates. In cyclopentene and 2,5-dihydrofuran hydrate, the radicals have non-planar conformations while the radical in the benzene hydrate has a planar ring. Acetone is a different guest from other compounds. It is not cyclic and it has a carbonyl group where Mu adds to the O atom in the C=O bond to form the radical. The temperature dependence of muon hfcs shows that the radical behaves differently in aqueous solution and the hydrate. The muon hfcs are much larger in the hydrate than in the aqueous solutions and pure liquid showing that there is a more efficient overlap between Mu and the carbon having the unpaired

electron in the hydrate. This is because there is less interaction between the radical and the cage wall in the hydrate compared to the liquid and also because of the large vibrational fluctuations of the Mu-O stretching coordinate.

Mu was also detected in the hydrates simultaneously with the radical and it was shown that the Mu amplitude decreases while the radical amplitude increases as the temperature rises in the acetone and benzene hydrates. Mu diffuses from the small cage to the large cage, adds to the guest in the large cage and forms a radical. The critical temperatures are 180 K and 235 K for the acetone and benzene hydrates respectively. Also since Mu hfc is the same in the small and large cages, we can conclude that Mu transport is reversible. Facile Mu or H atom diffusion may play an important role in the hydrogen storage and gas separation applications.

A few suggestions for future experiments are as follows:

In terms of handling the samples (hydrates), it is much easier to use the reactor where the sample was made directly for the μSR experiments. The hydrates have to be kept cold to be stable so usually the reactor is quenched in liquid nitrogen and then needs to be opened quickly for transferring the sample to the specific cells designed for μSR experiments, in a nitrogen bag (oxygen free environment). By doing an in situ experiment, not only one reduces the chance of losing the sample during the transfer step, but also prevents oxygen from the air to be contacted with the sample. Additionally, it will be possible to study the hydrates that need to be kept under pressure to be stable, such as ethene or propene hydrates, provided that the high energy beamline, M9b at TRIUMF will be operational.[182]

Optimizing the radical structure and frequency calculations could be done with a D4 model, an improved version of D3 model which will be available soon according to the authors.[183] Both models make use of dynamic polarizabilities obtained from first-principles time-dependent density functional theory calculations for atoms in different chemical environments employing fractional atomic coordination numbers for interpolation.[183] The D4 model allows for more efficient computation of molecular dipole-dipole dispersion coefficients with the errors significantly lower than the D3

method.[183] A thorough calculation could be done by averaging over various orientations of the radicals inside the cage.

Does C_{60} hydrate exist? The largest cage known so far belongs to structure H hydrate. It would be interesting to know whether a new type of hydrate exists which can accommodate C_{60} molecule. Calculation shows $(H_2O)_{60}$ can compete with other smaller water clusters energetically and it has a true minimum structure on the potential energy surface reported by Ludwig et al.[184] C_{60} being a hydrophobic guest keeps the water structure, $(H_2O)_{60}$, stable and there is no significant interaction between the water molecules and the guest.[184]

References

(1) McKenzie, I.; Roduner, E. *Naturwissenschaften* **2009**, *96* (8), 873.

(2) Cox, S. F. J. *J. Phys. C Solid State Phys.* **1987**, *20* (22), 3187.

(3) Blundell, S. J. *Chem. Rev.* **2004**, *104* (11), 5717.

(4) Fleming, D. G.; Arseneau, D. J.; Shelley, M. Y.; Beck, B.; Dilger, H.; Roduner, E. *J. Phys. Chem. C* **2011**, *115* (22), 11177.

(5) Fleming, D. G.; Arseneau, D. J.; Bridges, M. D.; Chen, Y. K.; Wang, Y. A. *J. Phys. Chem. C* **2013**, *117* (32), 16523.

(6) Percival, P. W.; Ghandi, K.; Brodovitch, J.-C.; Addison-Jones, B.; McKenzie, I. *Phys. Chem. Chem. Phys.* **2000**, *2* (20), 4717.

(7) Percival, P. W.; Brodovitch, J.-C.; Ghandi, K.; McCollum, B. M.; McKenzie, I. *J. Am. Chem. Soc.* **2005**, *127* (39), 13714.

(8) Roduner, E.; Strub, W.; Burkhard, P.; Hockmann, J.; Percival, P. W.; Fischer, H.; Ramos, M.; Webster, B. C. *Chem. Phys.* **1982**, *67* (3), 275.

(9) Lovett, B. W.; Stießberger, J. S.; Blundell, S. J.; Jestädt, T.; Ardavan, A.; Marshall, I. M.; Pratt, F. L.; Reid, I. D. *Phys. B Condens. Matter* **2000**, *289–290*, 612.

(10) Pratt, F. L. *J. Phys. Condens. Matter* **2004**, *16* (40), S4779.

(11) Neddermeyer, S. H.; Anderson, C. D. *Phys. Rev.* **1938**, *54* (1), 88.

(12) Roduner, E. *The Positive Muon as a Probe in Free Radical Chemistry*; Lecture Notes in Chemistry; Springer-Verlag: Berlin, 1988; Vol. 49.

(13) CODATA Value: muon-proton mass ratio https://physics.nist.gov/cgi-bin/cuu/Value?mmusmp|search_for=muon (accessed Dec 21, 2017).

(14) CODATA Value: muon-electron mass ratio https://physics.nist.gov/cgi-bin/cuu/Value?mmusme|search_for=muon (accessed Dec 21, 2017).

(15) Patrignani, C.; Group, P. D. *Chin. Phys. C* **2016**, *40* (10), 100001.

(16) CODATA Value: muon-proton magnetic moment ratio http://physics.nist.gov/cgi-bin/cuu/Value?mumumsmup|search_for=muon+magnetic+moment (accessed Apr 29, 2016).

(17) CODATA Value: proton gyromagnetic ratio over 2 pi https://physics.nist.gov/cgi-bin/cuu/Value?gammapbar|search_for=proton+gyromagnetic+rattio (accessed Dec 20, 2017).

(18) Schenck, A. *Muon spin rotation spectroscopy: principles and applications in solid state physics*; Hilger: Bristol, UK, 1985.

(19) Seeger, A. *Positive muons and pions in materials research: perspectives and future developments*; Chappert, J., Grynszpan, R. I., Eds.; Elsevier: Netherlands, 1984.

(20) Friedman, J. I.; Telegdi, V. L. *Phys. Rev.* **1957**, *106* (6), 1290.

(21) Walker, D. C. *J. Phys. Chem.* **1981**, *85* (26), 3960.

(22) Percival, P. W.; Mozafari, M.; Brodovitch, J.-C.; Chandrasena, L. *J. Phys. Chem. A* **2014**, *118* (7), 1162.

(23) Fessenden, R. W.; Schuler, R. H. *J. Chem. Phys.* **1965**, *43* (8), 2704.

(24) Fessenden, R. W. *J. Phys. Chem.* **1967**, *71* (1), 74.

(25) Roduner, E.; Percival, P. W.; Fleming, D. G.; Hochmann, J.; Fischer, H. *Chem. Phys. Lett.* **1978**, *57* (1), 37.

(26) McKenzie, I. *Annu. Rep. Sect. C Phys. Chem.* **2013**, *109* (0), 65.

(27) Mozafari, M.; Brodovitch, J.-C.; Chandrasena, L.; Percival, P. W. *J. Phys. Chem. A* **2016**.

(28) Abragam, A. *Comptes Rendus Acad. Sci. Ser. II Mec. Phys. Chim. Sci. Terre Univers* **1984**, *299* (3), 95.

(29) Heming, M.; Roduner, E.; Patterson, B. D.; Odermatt, W.; Schneider, J.; Baumeler, H.; Keller, H.; Savic, I. M. *Chem. Phys. Lett.* **1986**, *128* (1), 100.

(30) Kreitzman, S. R.; Roduner, E. *Chem. Phys.* **1995**, *192* (3), 189.

(31) Roduner, E. *Chem. Soc. Rev.* **1993**, *22* (5), 337.

(32) Davy, H. *Philos. Trans. R. Soc. Lond.* **1811**, *101*, 1.

(33) Faraday, M. *Q. J. Sci. Lit. Arts* **1823**, *15*, 71.

(34) *Water in Crystalline Hydrates Aqueous Solutions of Simple Nonelectrolytes*; Franks, F., Ed.; Springer US: Boston, MA, 1973.

(35) Hammerschmidt, E. G. *Ind. Eng. Chem.* **1934**, *26* (8), 851.

(36) Powell, H. M. *J. Chem. Soc.* **1948**, 61.

(37) Palin, D. E.; Powell, H. M. *J. Chem. Soc. Resumed* **1947**, 208.

(38) Claussen, W. F. *J. Chem. Phys.* **1951**, *19* (2), 259.

(39) von Stackelberg, M.; Müller, H. R. *J. Chem. Phys.* **1951**, *19* (10), 1319.

(40) Pauling, L.; Marsh, R. E. *Proc. Natl. Acad. Sci. U. S. A.* **1952**, *38* (2), 112.

(41) Jeffrey, G. A. *J. Incl. Phenom.* **1984**, *1* (3), 211.

(42) Ripmeester, J. A. *Ann. N. Y. Acad. Sci.* **2000**, *912* (1), 1.

(43) Chong, Z. R.; Yang, S. H. B.; Babu, P.; Linga, P.; Li, X.-S. *Appl. Energy* **2016**, *162*, 1633.

(44) Boswell, R.; Collett, T. S. *Energy Environ. Sci.* **2011**, *4* (4), 1206.

(45) Sloan, E. D. *Nature* **2003**, *426* (6964), 353.

(46) Kvenvolden, K. A. *Rev. Geophys.* **1993**, *31* (2), 173.

(47) Koh, C. A.; Sum, A. *Natural Gas Hydrates in Flow Assurance*; Gulf Professional Publishing, 2010.

(48) Englezos, P. *Ind. Eng. Chem. Res.* **1993**, *32* (7), 1251.

(49) Giavarini, C.; Hester, K. *Gas Hydrates: Immense Energy Potential and Environmental Challenges*; Springer-Verlag: London, 2011.

(50) Davidson, D. W. *Can. J. Chem.* **1971**, *49* (8), 1224.

(51) Sloan Jr, E. D.; Koh, C. A. *Clathrate hydrates of natural gases*, 3rd ed.; CRC press: Boca Raton, FL, 2008.

(52) Koh, C. A.; Sum, A. K.; Sloan, E. D. *J. Appl. Phys.* **2009**, *106* (6), 061101.

(53) Strobel, T. A.; Hester, K. C.; Koh, C. A.; Sum, A. K.; Sloan Jr., E. D. *Chem. Phys. Lett.* **2009**, *478* (4–6), 97.

(54) Moudrakovski, I. L.; Sanchez, A. A.; Ratcliffe, C. I.; Ripmeester, J. A. *J. Phys. Chem. B* **2001**, *105* (49), 12338.

(55) Englezos, P.; Lee, J. D. *Korean J. Chem. Eng.* **2005**, *22* (5), 671.

(56) Javanmardi, J.; Nasrifar, K.; Najibi, S. H.; Moshfeghian, M. *Appl. Therm. Eng.* **2005**, *25* (11–12), 1708.

(57) Duc, N. H.; Chauvy, F.; Herri, J.-M. *Energy Convers. Manag.* **2007**, *48* (4), 1313.

(58) Kamata, Y.; Yamakoshi, Y.; Ebinuma, T.; Oyama, H.; Shimada, W.; Narita, H. *Energy Fuels* **2005**, *19* (4), 1717.

(59) Shimada, W.; Ebinuma, T.; Oyama, H.; Kamata, Y.; Takeya, S.; Uchida, T.; Nagao, J.; Narita, H. *Jpn. J. Appl. Phys.* **2003**, *42* (2A), L129.

(60) Tajima, H.; Yamasaki, A.; Kiyono, F. *Energy* **2004**, *29* (11), 1713.

(61) Max, M. D.; Pellenbarg, R. E. Desalination through methane hydrate. US patent 5,873,262, February 23, 1999.

(62) Knox, W. G.; Hess, M.; Jones, G. E. J.; Smith, H. B. J. *Chem. Eng. Prog.* **1961**, *57* (2), 66.

(63) Barduhn, A. J. *Chem. Eng. Prog.* **1967**, *63* (1), 98.

(64) Koh, C. A.; Sloan, E. D.; Sum, A. K.; Wu, D. T. *Annu. Rev. Chem. Biomol. Eng.* **2011**, *2* (1), 237.

(65) Eslamimanesh, A.; Mohammadi, A. H.; Richon, D.; Naidoo, P.; Ramjugernath, D. *J. Chem. Thermodyn.* **2012**, *46*, 62.

(66) Aydoğan, Ö.; Bayraktar, E.; Parlaktuna, M.; Mehmetoğlu, T.; Mehmetoğlu, Ü. *Biocatal. Biotransformation* **2007**, *25* (5), 365.

(67) Koh, C. A. *Chem. Soc. Rev.* **2002**, *31* (3), 157.

(68) Goldberg, P. *Science* **1963**, *142* (3590), 378.

(69) Takeya, K.; Nango, K.; Sugahara, T.; Ohgaki, K.; Tani, A. *J. Phys. Chem. B* **2005**, *109* (44), 21086.

(70) Takeya, K.; Nango, K.; Sugahara, T.; Ohgaki, K.; Tani, A.; Ito, H.; Okada, M.; Kasai, T. *Jpn. J. Appl. Phys.* **2007**, *46* (5R), 3066.

(71) Ohgaki, K.; Nakatsuji, K.; Takeya, K.; Tani, A.; Sugahara, T. *Phys. Chem. Chem. Phys.* **2008**, *10* (1), 80.

(72) Sugahara, T.; Kobayashi, Y.; Tani, A.; Inoue, T.; Ohgaki, K. *J. Phys. Chem. A* **2012**, *116* (10), 2405.

(73) Oshima, M.; Tani, A.; Sugahara, T.; Kitano, K.; Ohgaki, K. *Phys. Chem. Chem. Phys.* **2014**, *16* (8), 3792.

(74) Oshima, M.; Kitamura, K.; Tani, A.; Sugahara, T.; Ohgaki, K. *J. Phys. Chem. B* **2014**, *118* (47), 13435.

(75) Koh, D.-Y.; Kang, H.; Lee, H. *Korean J. Chem. Eng.* **2015**, *32* (2), 350.

(76) Alavi, S.; Ripmeester, J. A. *Chem. Phys. Lett.* **2009**, *479* (4–6), 234.

(77) Ahn, Y.-H.; Lim, H.-K.; Kang, H.; Kim, H.; Cha, M.; Shin, K.; Lee, H. *J. Phys. Chem. C* **2016**, *120* (31), 17190.

(78) TRIUMF: Canada's National Laboratory for Particle and Nuclear Physics http://www.triumf.ca/home/about-triumf/history (accessed Nov 12, 2016).

(79) Main Cyclotron & Beam Lines,TRIUMF: Canada's National Laboratory for Particle and Nuclear Physics http://www.triumf.ca/research-program/research-facilities/main-cyclotron-beam-lines (accessed Nov 13, 2016).

(80) Pifer, A. E.; Bowen, T.; Kendall, K. R. *Nucl. Instrum. Methods* **1976**, *135* (1), 39.

(81) Beveridge, J. L.; Reid, I. D.; Doornbos, J.; Garner, D. M.; Arseneau, D. J.; Senba, M. *Nucl. Instrum. Methods Phys. Res.* **1985**, *240* (2), 316.

(82) Nagamine, K. *Introductory Muon Science*; Cambridge University Press, 2003.

(83) The μSR Spectrometers http://musr.ca/equip/spect.html (accessed Nov 14, 2016).

(84) Kreitzman, S. R.; Arseneau, D. J.; Hitti, B.; Brewer, J. H. μSR Facility Users Guide, 1999.

(85) Cryostats etc http://musr.ca/equip/ins.html (accessed Dec 17, 2016).

(86) Yaouanc, A.; Dalmas de Réotier, P. *Muon spin rotation, relaxation, and resonance: applications to condensed matter*; Oxford University Press: Oxford, 2011.

(87) Kiefl, R. F. *Hyperfine Interact.* **1986**, *32* (1–4), 707.

(88) Eaton, G. R.; Eaton, S. S.; Barr, D. P.; Weber, R. T. *Quantitative EPR: A Practitioners Guide*; Springer Vienna, 2010.

(89) Brodovitch, J.-C. LCR fit instructions, 2014.

(90) Senba, M.; Fleming, D. G.; Arseneau, D. J.; Garner, D. M.; Reid, I. D. *Phys. Rev. A* **1989**, *39* (8), 3871.

(91) SS-1210-1-12W | Swagelok http://www.swagelok.com/en/catalog/Product/Detail?part=SS-1210-1-12W# (accessed Nov 30, 2016).

(92) Machine Shop - Faculty of Science - Simon Fraser University https://www.sfu.ca/science/faculty-support/facilities-services/machine-shop.html (accessed Nov 30, 2016).

(93) MVE CryoShipper QWick & Vapor Series | Chart Industries http://www.chartindustries.com/Life-Sciences/Aluminum-Dewars/MVE-CryoShipper-QWick-Vapor-Series (accessed Nov 30, 2016).

(94) Ripmeester, J. A.; Ratcliffe, C. I. *J. Phys. Chem.* **1990**, *94* (25), 8773.

(95) Cha, M.; Baek, S.; Lee, H.; Lee, W. J. *RSC Adv.* **2014**, *4* (50), 26176.

(96) Cha, M.; Lee, H.; Lee, J. W. *J. Phys. Chem. C* **2013**, *117* (45), 23515.

(97) Bernstein, J. *Polymorphism in Molecular Crystals*; Clarendon Press, 2002.

(98) Bertie, J. E.; Jacobs, S. M. *J. Chem. Phys.* **1978**, *69* (9), 4105.

(99) Ripmeester, J. A. *J. Am. Chem. Soc.* **1982**, *104* (1), 289.

(100) Moudrakovski, I. L.; Ratcliffe, C. I.; Ripmeester, J. A. *J. Am. Chem. Soc.* **2001**, *123* (9), 2066.

(101) 5 mm Heavy Wall Precision Low Pressure/Vacuum NMR Sample Tube 7" L, 400MHz | Wilmad-LabGlass https://www.wilmad-labglass.com/Products/522-LPV-7/ (accessed Dec 8, 2016).

(102) Birchall, T.; Frampton, C. S.; Schrobilgen, G. J.; Valsdóttir, J. *Acta Crystallogr. C* **1989**, *45* (6), 944.

(103) Conde, M. M.; Torré, J. P.; Miqueu, C. *Phys. Chem. Chem. Phys.* **2016**, *18* (15), 10018.

(104) Ripmeester, J. A.; Ratcliffe, C. I.; Tse, J. S. *J. Chem. Soc. Faraday Trans. 1 Phys. Chem. Condens. Phases* **1988**, *84* (11), 3731.

(105) Lee, J.-W.; Lu, H.; Moudrakovski, I. L.; Ratcliffe, C. I.; Ohmura, R.; Alavi, S.; Ripmeester, J. A. *J. Phys. Chem. A* **2011**, *115* (9), 1650.

(106) Earl, W. L.; Vanderhart, D. L. *J. Magn. Reson. 1969* **1982**, *48* (1), 35.

(107) Ripmeester, J. A.; Ratcliffe, C. I. *J. Phys. Chem.* **1988**, *92* (2), 337.

(108) Shin, W.; Park, S.; Ro, H.; Koh, D.-Y.; Seol, J.; Lee, H. *J. Chem. Thermodyn.* **2012**, *44* (1), 20.

(109) Abraham, R. J.; Lapper, R. D.; Smith, K. M.; Unsworth, J. F. *J. Chem. Soc. Perkin Trans. 2* **1974**, No. 9, 1004.

(110) Corminboeuf, C.; Tran, F.; Weber, J. *J. Mol. Struct. THEOCHEM* **2006**, *762* (1–3), 1.

(111) Lewars, E. *Computational Chemistry-Introduction to the Theory and Applications of Molecular and Quantum Mechanics*; Kluwer Academic Publishers, 2003.

(112) Hohenberg, P.; Kohn, W. *Phys. Rev.* **1964**, *136* (3B), B864.

(113) Kohn, W.; Sham, L. J. *Phys. Rev.* **1965**, *140* (4A), A1133.

(114) Koch, W.; Holthausen, M. C. *A Chemist's Guide to Density Functional Theory*; John Wiley & Sons, 2015.

(115) Basis Sets http://www.gaussian.com/g_tech/g_ur/m_basis_sets.htm (accessed Dec 19, 2016).

(116) Frisch, A. E.; Foresman, J. B. *Exploring Chemistry with Electronic Structure Methods*; Gaussian Inc.: Pittsburgh, PA, 1996.

(117) Atkins, P.; Paula, J. de. *Physical Chemistry for the Life Sciences*; OUP Oxford, 2011.

(118) Roduner, E. In *Isotope effects in chemistry and biology*; Kohen, A., Limbach, H.-H., Eds.; CRC press: Boca Raton, FL, 2005; pp 433–450.

(119) CODATA Value: muon mass in u http://physics.nist.gov/cgi-bin/cuu/Value?mmuu|search_for=muon+mass (accessed Apr 29, 2016).

(120) CODATA Value: muon magnetic moment to nuclear magneton ratio http://physics.nist.gov/cgi-bin/cuu/Value?mumumsmun|search_for=muon+magnetic+moment (accessed May 5, 2016).

(121) G09 Keyword: Freq http://www.gaussian.com/g_tech/g_ur/k_freq.htm (accessed Dec 30, 2016).

(122) Frisch, M. J.; Trucks, G. W.; Schlegel, H. B.; Scuseria, G. E.; Robb, M. A.; Cheeseman, J. R.; Scalmani, G.; Barone, V.; Mennucci, B.; Petersson, G. A.; Nakatsuji, H.; Caricato, M.; Li, X.; Hratchian, H. P.; Izmaylov, A. F.; Bloino, J.; Zheng, G.; Sonnenberg, J. L.; Hada, M.; Ehara, M.; Toyota, K.; Kiefl, R. F.; Hasegawa, J.; Ishida, M.; Nakajima, T.; Honda, Y.; Kitao, O.; Nakai, H.; Vreven, T.; Montgomery, J.; Peralta, J. E.; Ogliaro, F.; Bearpark, M.; Heyd, J. J.; Brothers, E.; Kudin, K. N.; Staroverov, V. N.; Kobayashi, R.; Normand, J.; Raghavachari, K.; Rendell, A.; Burant, J. C.; Iyengar, S. S.; Tomasi, J.; Cossi, M.; Rega, N.; Millam, J. M.; Klene, M.; Knox, J. E.; Cross, J. B.; Bakken, V.; Adamo, C.; Jaramillo, J.; Gomperts, R.; Stratmann, R. E.; Yazyev, O.; Austin, A. J.; Cammi, R.; Pomelli, C.; Ochterski, J. W.; Martin, R. L.; Morokuma, K.; Zakrzewski, V. G.; Voth, G. A.; Salvador, P.; Dannenberg, J. J.; Dapprich, S.; Daniels, A. D.; Farkas, Ö.; Foresman, J. B.; Ortiz, J. V.; Cioslowski, J.; Fox, D. J. *Gaussian 09, Revision D.01*; Gaussian Inc.: Wallingford, CT, 2009.

(123) WestGrid | Western Canada Research Grid https://www.westgrid.ca/ (accessed Dec 19, 2016).

(124) Takeya, K.; Tani, A.; Yada, T.; Ikeya, M.; Ohgaki, K. *Jpn. J. Appl. Phys.* **2004**, *43* (1R), 353.

(125) Takeya, K.; Sugahara, T.; Ohgaki, K.; Tani, A. *Radiat. Meas.* **2007**, *42* (8), 1301.

(126) Kobayashi, N.; Minami, T.; Tani, A.; Nakagoshi, M.; Sugahara, T.; Takeya, K.; Ohgaki, K. *Energies* **2012**, *5* (6), 1705.

(127) Yeon, S.-H.; Seol, J.; Park, Y.; Koh, D.-Y.; Kang, Y. S.; Lee, H. *J. Am. Chem. Soc.* **2008**, *130* (29), 9208.

(128) Ceppatelli, M.; Bini, R.; Schettino, V. *J. Phys. Chem. B* **2009**, *113* (44), 14640.

(129) Ceppatelli, M.; Bini, R.; Schettino, V. *Phys. Chem. Chem. Phys.* **2011**, *13* (4), 1264.

(130) Roduner, E.; Percival, P. W.; Han, P.; Bartels, D. M. *J. Chem. Phys.* **1995**, *102* (15), 5989.

(131) Ghandi, K.; Brodovitch, J.-C.; Addison-Jones, B.; Percival, P. W.; Schüth, J. *Phys. B Condens. Matter* **2000**, *289*, 476.

(132) Percival, P. W.; Brodovitch, J.-C.; Newman, K. E.; Spencer, D. P. *Chem. Phys. Lett.* **1982**, *93* (4), 366.

(133) Percival, P. W.; Adamson-Sharpe, K. M.; Brodovitch, J.-C.; Leung, S.-K.; Newman, K. E. *Chem. Phys.* **1985**, *95* (2), 321.

(134) Roduner, E.; Reid, I. D. *Isr. J. Chem.* **1989**, *29* (1), 3.

(135) West, R.; Percival, P. W. *Dalton Trans.* **2010**, *39* (39), 9209.

(136) Cox, S. F. J. *Rep. Prog. Phys.* **2009**, *72* (11), 116501.

(137) Patterson, B. D. *Rev. Mod. Phys.* **1988**, *60* (1), 69.

(138) Buch, V.; Devlin, J. P.; Monreal, I. A.; Jagoda-Cwiklik, B.; Uras-Aytemiz, N.; Cwiklik, L. *Phys. Chem. Chem. Phys.* **2009**, *11* (44), 10245.

(139) Alavi, S.; Ripmeester, J. A. *J. Chem. Phys.* **2012**, *137* (5), 054712.

(140) Moudrakovski, I. L.; Udachin, K. A.; Alavi, S.; Ratcliffe, C. I.; Ripmeester, J. A. *J. Chem. Phys.* **2015**, *142* (7), 074705.

(141) Fleischer, E. B.; Janda, K. C. *J. Phys. Chem. A* **2013**, *117* (19), 4001.

(142) Grimme, S. *J. Comput. Chem.* **2006**, *27* (15), 1787.

(143) Gilbert, B. C.; Trenwith, M. *J. Chem. Soc. Perkin Trans. 2* **1975**, No. 10, 1083.

(144) Schuler, R. H.; Laroff, G. P.; Fessenden, R. W. *J. Phys. Chem.* **1973**, *77* (4), 456.

(145) Gilbert, B. C.; Norman, R. O. C.; Williams, P. S. *J. Chem. Soc. Perkin Trans. 2* **1980**, No. 4, 647.

(146) Lunazzi, L.; Placucci, G.; Grossi, L. *J. Chem. Soc. Perkin Trans. 2* **1982**, No. 7, 875.

(147) Geimer, J.; Bernhard, K.; Naumov, S.; Beckert, D. *Phys. Chem. Chem. Phys.* **2002**, *4* (10), 1738.

(148) Percival, P. W.; Kiefl, R. F.; Kreitzman, S. R.; Garner, D. M.; Cox, S. F. J.; Luke, G. M.; Brewer, J. H.; Nishiyama, K.; Venkateswaran, K. *Chem. Phys. Lett.* **1987**, *133* (6), 465.

(149) Woon, D. E.; Dunning, T. H. *J. Chem. Phys.* **1993**, *98* (2), 1358.

(150) Sun, N.; Li, Z.; Qiu, N.; Yu, X.; Zhang, X.; Li, Y.; Yang, L.; Luo, K.; Huang, Q.; Du, S. *J. Phys. Chem. A* **2017**, *121* (13), 2620.

(151) Liu, L.; Mao, S.; Li, Q.; Wang, X.; Yang, M.; Li, L. *RSC Adv.* **2017**, *7* (24), 14537.

(152) Samuni, A.; Neta, P. *J. Phys. Chem.* **1973**, *77* (13), 1629.

(153) Dogan, I.; Steenken, S.; Schulte-Frohlinde, D.; Icli, S. *J. Phys. Chem.* **1990**, *94* (5), 1887.

(154) Alavi, S.; Susilo, R.; Ripmeester, J. A. *J. Chem. Phys.* **2009**, *130* (17), 174501.

(155) Safarik, I.; Strausz, O. P. *Rev. Chem. Intermed.* **1985**, *6* (2), 143.

(156) Nagai, S.; Gillbro, T. *J. Phys. Chem.* **1979**, *83* (3), 402.

(157) Lloyd, R. V.; DiGregorio, S.; Wood, D. E. *J. Chem. Phys.* **1978**, *68* (4), 1813.

(158) Gamba, Z.; Klein, M. L. *J. Chem. Phys.* **1990**, *92* (11), 6973.

(159) Gontrani, L.; Ramondo, F.; Caminiti, R. *Chem. Phys. Lett.* **2006**, *417* (1–3), 200.

(160) Alavi, S.; Udachin, K.; Ripmeester, J. A. *Chem. Eur. J.* **2010**, *16* (3), 1017.

(161) Shin, K.; Kumar, R.; Udachin, K. A.; Alavi, S.; Ripmeester, J. A. *Proc. Natl. Acad. Sci.* **2012**, *109* (37), 14785.

(162) English, N. J.; Tse, J. S. *J. Phys. Chem. A* **2011**, *115* (23), 6226.

(163) Ripmeester, J. A.; Ratcliffe, C. I. *J. Struct. Chem.* **1999**, *40* (5), 654.

(164) Hill, A.; Symons, M. C. R.; Cox, S. F. J.; Renzi, R. de; Scott, C. A.; Bucci, C.; Vecli, A. *J. Chem. Soc. Faraday Trans. 1 Phys. Chem. Condens. Phases* **1985**, *81* (2), 433.

(165) Ghandi, K.; Addison-Jones, B.; Brodovitch, J.-C.; McCollum, B. M.; McKenzie, I.; Percival, P. W. *J. Am. Chem. Soc.* **2003**, *125* (32), 9594.

(166) Brodovitch, J.-C.; McCollum, B. M.; Percival, P. W. *Phys. B Condens. Matter* **2009**, *404* (5–7), 950.

(167) Buttar, D.; Macrae, R. M.; Webster, B. C.; Roduner, E. *Hyperfine Interact.* **1991**, *65* (1–4), 927.

(168) Takebayashi, Y.; Otake, K. *Rev. High Press. Sci. Technol.* **2002**, *12* (1), 22.

(169) Oba, Y.; Kawatsu, T.; Tachikawa, M. *J. Chem. Phys.* **2016**, *145* (6), 064301.

(170) Rhodes, C. J.; Webster, B. C. *J. Chem. Soc. Faraday Trans.* **1993**, *89* (8), 1283.

(171) Rhodes, C. J.; Symons, M. C. R. *Magn. Reson. Chem.* **1996**, *34* (8), 631.

(172) CODATA Value: deuteron-proton magnetic moment ratio https://physics.nist.gov/cgi-bin/cuu/Value?mudsmup|search_for=ratio (accessed Jul 29, 2017).

(173) Percival, P. W.; Addison-Jones, B.; Brodovitch, J.-C.; Sun-Mack, S. *Appl. Magn. Reson.* **1996**, *11* (2), 315.

(174) Percival, P. W.; Wlodek, S. *Chem. Phys. Lett.* **1992**, *196* (3), 317.

(175) Yu, D.; Percival, P. W.; Brodovitch, J.-C.; Leung, S.-K.; Kiefl, R. F.; Venkateswaran, K.; Cox, S. F. J. *Chem. Phys.* **1990**, *142* (2), 229.

(176) Gorman, P. D.; English, N. J.; MacElroy, J. M. D. *J. Chem. Phys.* **2012**, *136* (4), 044506.

(177) Davidson, D. W.; Ripmeester, J. A. *J. Glaciol.* **1978**, *21* (85), 33.

(178) Roduner, E.; Reid, I. D.; Riccò, M.; Renzi, R. D. *Berichte Bunsenges. Für Phys. Chem.* **1989**, *93* (11), 1194.

(179) Roduner, E.; Stolmár, M.; Dilger, H.; Reid, I. D. *J. Phys. Chem. A* **1998**, *102* (39), 7591.

(180) Fleming, D. G.; Shelley, M. Y.; Arseneau, D. J.; Senba, M.; Pan, J. J.; Roduner, E. *J. Phys. Chem. B* **2002**, *106* (25), 6395.

(181) Fleming, D. G.; Arseneau, D. J.; Pan, J. (Jun); Shelley, M. Y.; Senba, M.; Percival, P. W. *Appl. Magn. Reson.* **1997**, *13* (1–2), 181.

(182) M9B http://musr.ca/equip/mubeamlines/node5.html (accessed Sep 28, 2017).

(183) Caldeweyher, E.; Bannwarth, C.; Grimme, S. *J. Chem. Phys.* **2017**, *147* (3), 034112.

(184) Ludwig, R.; Appelhagen, A. *Angew. Chem. Int. Ed.* **2005**, *44* (5), 811.

Appendix A.

PXRD spectra

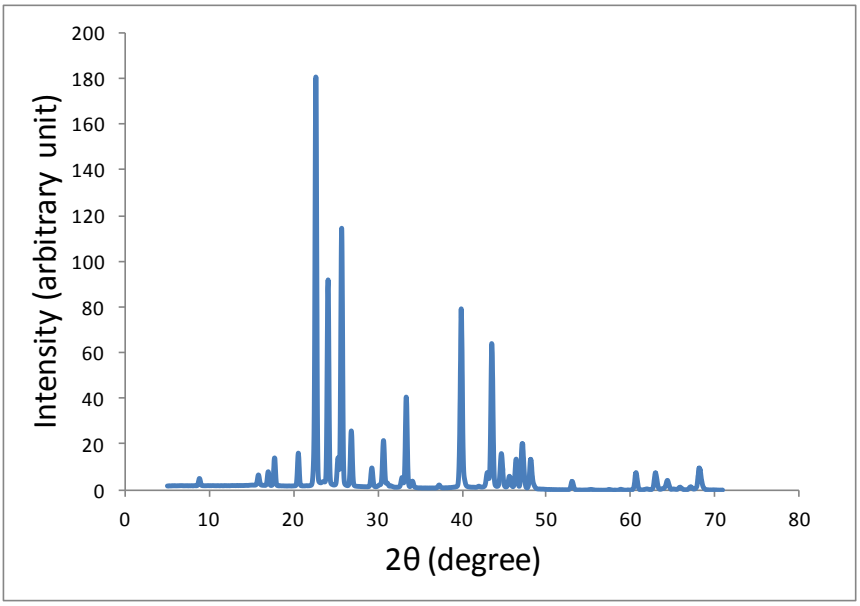

Figure A1: PXRD spectrum of acetone hydrate

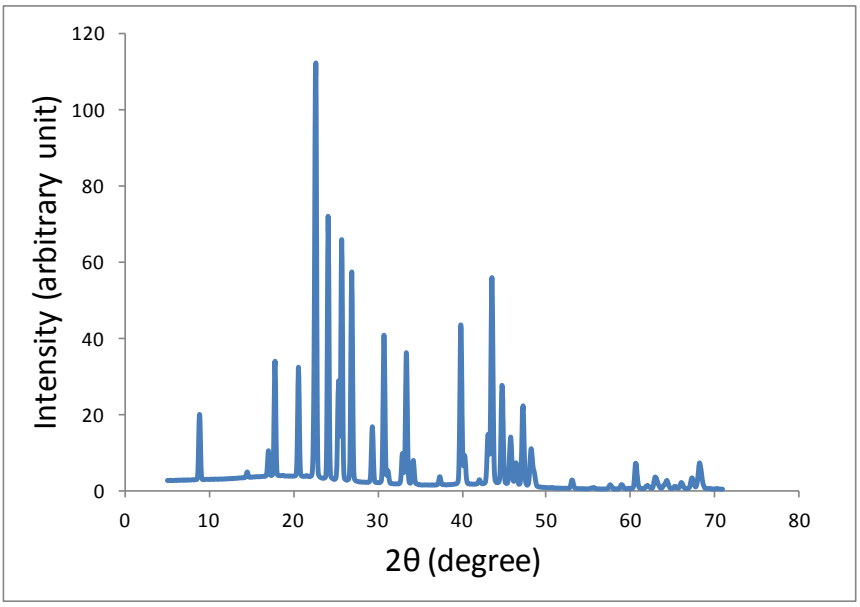

Figure A2: PXRD spectrum of isoxazole hydrate

Appendix B.

Optimized geometries of muoniated cyclopentyl and hydrofuranyl radicals

Muoniated cyclopentyl

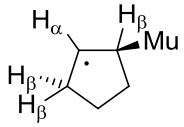

SCF Energy /Hartree -195.9077578

Zero-point Energy (Mu axial) /Hartree 0.1486060

Zero-point Energy (Mu eq.) /Hartree 0.1489422

Reference geometry and 0 K vibrationally averaged hyperfine constants

	Cartesian coordinates /Å			hfc /MHz
C(13)	0.481963	-1.071203	-0.343223	-29.2
C(13)	-0.891768	-0.826281	0.325649	4.7
C(13)	-1.169144	0.669674	0.077396	3.4
C(13)	0.221664	1.336689	0.200913	-28.2
C(13)	1.16817	0.257385	-0.232194	151.5
Mu	0.348914	-1.366905	-1.399425	459.8
H(β1)	1.042925	-1.892094	0.124539	74.2
H	-1.68124	-1.478053	-0.061169	-1.2
H	-0.811836	-1.013111	1.403613	-2.2
H	-1.552667	0.810151	-0.940679	-1.8
H	-1.909815	1.087822	0.766062	-1.0
H(β2)	0.307181	2.256283	-0.394382	74.5
H(β3)	0.411494	1.641064	1.245912	126.7
H(α)	2.220661	0.418079	-0.439812	-60.9

The isomeric structure with Mu more equatorial has the same coordinates except for Mu and H(β1), which are swapped.

Geometry optimization and frequency calculations were achieved with the keywords

UB3LYP/6-31G(d,p) Freq=(Noraman,Anharmonic,Readanharm) Opt=Tight Int =UltraFine

Muoniated hydrofuryl

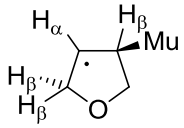

SCF Energy /Hartree -231.794007

Zero-point Energy (Mu axial) 0.124464

Zero-point Energy (Mu eq.) 0.124753

Reference geometry and 0 K vibrationally averaged hyperfine constants

	Cartesian coordinates /Å			**hfc /MHz**
O(17)	1.284813	-1.568563	0.513529	-0.4
C(13)	2.333036	-0.605222	0.615248	5.7
C(13)	1.652822	0.704376	1.061774	-28.8
C(13)	0.294401	0.536881	0.462058	155.5
C(13)	0.117064	-0.88833	0.04728	-29.0
H	2.826817	-0.463303	-0.360116	-1.9
H	3.070256	-0.991051	1.324352	-0.9
H(β1)	2.183926	1.598734	0.712443	69.1
Mu	1.609954	0.769273	2.161976	463.9
H(α)	-0.460731	1.307137	0.369268	-59.2
H(β2)	-0.761256	-1.379784	0.491388	93.1
H(β3)	0.016698	-0.989349	-1.051901	110.8

The isomeric structure with Mu more equatorial has the same coordinates except for Mu and H(β1), which are swapped.

Geometry optimization and frequency calculations were achieved with the keywords

UB3LYP/6-31G(d,p) Freq=(Noraman,Anharmonic,Readanharm) Opt=Tight Int =UltraFine

Calculations were performed with Gaussian 09:

Gaussian 09, Revision D.01, Frisch, M. J.; Trucks, G. W.; Schlegel, H. B.; Scuseria, G. E.; Robb, M. A.; Cheeseman, J. R.; Scalmani, G.; Barone, V.; Mennucci, B.; Petersson, G. A.; Nakatsuji, H.; Caricato, M.; Li, X.; Hratchian, H. P.; Izmaylov, A. F.; Bloino, J.; Zheng, G.; Sonnenberg, J. L.; Hada, M.; Ehara, M.; Toyota, K.; Fukuda, R.; Hasegawa, J.; Ishida, M.; Nakajima, T.; Honda, Y.; Kitao, O.; Nakai, H.; Vreven, T.; Montgomery, J. A., Jr.; Peralta, J. E.; Ogliaro, F.; Bearpark, M.; Heyd, J. J.; Brothers, E.; Kudin, K. N.; Staroverov, V. N.; Kobayashi, R.; Normand, J.; Raghavachari, K.; Rendell, A.; Burant, J. C.; Iyengar, S. S.; Tomasi, J.; Cossi, M.; Rega, N.; Millam, N. J.; Klene, M.; Knox, J. E.; Cross, J. B.; Bakken, V.; Adamo, C.; Jaramillo, J.; Gomperts, R.; Stratmann, R. E.; Yazyev, O.; Austin, A. J.; Cammi, R.; Pomelli, C.; Ochterski, J. W.; Martin, R. L.; Morokuma, K.; Zakrzewski, V. G.; Voth, G. A.; Salvador, P.; Dannenberg, J. J.; Dapprich, S.; Daniels, A. D.; Farkas, Ö.; Foresman, J. B.; Ortiz, J. V.; Cioslowski, J.; Fox, D. J. Gaussian, Inc., Wallingford CT, 2009.

Appendix C.

Internal coordinates of optimized geometries for radicals 1–5, computed with both B3LYP/6-31G(d) and B3LYP/EPR-II

Internal coordinates of optimized geometries for radical 1

Scheme C1. Atom numbering

C1	H6	H12
C2	H7	H10 (Mu)
C3	H8	
C4	H9	H11
O5		

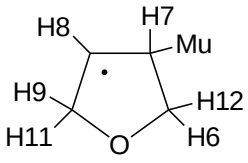

Table C1. Internal coordinates

		Optimized Parameters (Å and °)	
Name	**Definition**	**6-31G(d)**	**EPR-II**
R1	R(1,2)	1.5425	1.5464
R2	R(1,5)	1.4268	1.4319
R3	R(1,6)	1.1028	1.1014
R4	R(1,12)	1.0936	1.0928
R5	R(2,3)	1.4948	1.5034
R6	R(2,7)	1.0981	1.0964
R7	R(2,10)	1.1037	1.1013
R8	R(3,4)	1.4956	1.5033
R9	R(3,8)	1.0833	1.0835
R10	R(4,5)	1.4292	1.4337
R11	R(4,9)	1.1086	1.1066
R12	R(4,11)	1.1004	1.0984
A1	A(2,1,5)	105.6811	105.6507
A2	A(2,1,6)	110.2107	110.2399
A3	A(2,1,12)	114.2188	113.9387
A4	A(5,1,6)	110.5816	110.2884
A5	A(5,1,12)	107.5267	107.6264
A6	A(6,1,12)	108.5591	109.0042
A7	A(1,2,3)	100.8831	101.0084
A8	A(1,2,7)	112.7245	112.6267
A9	A(1,2,10)	110.8374	110.7248
A10	A(3,2,7)	113.8109	113.5574
A11	A(3,2,10)	111.8674	111.5246
A12	A(7,2,10)	106.7835	107.4033
A13	A(2,3,4)	109.0473	108.8274
A14	A(2,3,8)	126.0527	126.1316
A15	A(4,3,8)	124.8704	124.9898
A16	A(3,4,5)	105.4043	105.3272
A17	A(3,4,9)	111.9963	111.7882
A18	A(3,4,11)	114.2030	113.8467
A19	A(5,4,9)	110.6335	110.3195
A20	A(5,4,11)	107.7945	107.9950
A21	A(9,4,11)	106.7655	107.4975
A22	A(1,5,4)	107.6030	107.4723

		Optimized Parameters (Å and °)	
Name	**Definition**	**6-31G(d)**	**EPR-II**
D1	D(5,1,2,3)	29.4400	29.2275
D2	D(5,1,2,7)	151.1914	150.7070
D3	D(5,1,2,10)	-89.1803	-89.0175
D4	D(6,1,2,3)	-90.0609	-89.9224
D5	D(6,1,2,7)	31.6905	31.5572
D6	D(6,1,2,10)	151.3188	151.8327
D7	D(12,1,2,3)	147.4260	147.1606
D8	D(12,1,2,7)	-90.8226	-91.3599
D9	D(12,1,2,10)	28.8057	28.9156
D10	D(2,1,5,4)	-35.0962	-35.7563
D11	D(6,1,5,4)	84.1597	83.3614
D12	D(12,1,5,4)	-157.4728	-157.8397
D13	D(1,2,3,4)	-14.1534	-13.1812
D14	D(1,2,3,8)	167.7558	169.3261
D15	D(7,2,3,4)	-135.1385	-134.0042
D16	D(7,2,3,8)	46.7707	48.5031
D17	D(10,2,3,4)	103.7174	104.4814
D18	D(10,2,3,8)	-74.3734	-73.0112
D19	D(2,3,4,5)	-5.6849	-7.0840
D20	D(2,3,4,9)	114.6806	112.7388
D21	D(2,3,4,11)	-123.8091	-125.2077
D22	D(8,3,4,5)	172.4338	170.4441
D23	D(8,3,4,9)	-67.2007	-69.7330
D24	D(8,3,4,11)	54.3096	52.3204
D25	D(3,4,5,1)	25.3961	26.6324
D26	D(9,4,5,1)	-95.8610	-94.1578
D27	D(11,4,5,1)	147.7432	148.6236

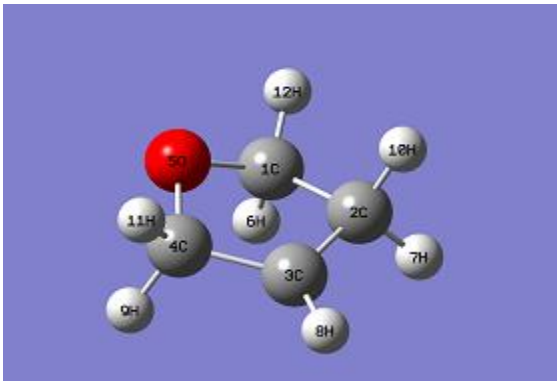

Figure C1. Optimized geometry of radical 1.

Internal coordinates of optimized geometries for radical 2

Scheme C2. Atom numbering

C1	H6	H7
C2	H8	H9
C3	H10	H11 (Mu)
C4	H12	
O5		

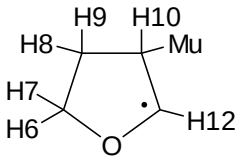

Table C2. Internal coordinates

		Optimized Parameters (Å and °)	
Name	**Definition**	**6-31G(d)**	**EPR-II**
R1	R(1,2)	1.5344	1.5394
R2	R(1,5)	1.4408	1.4460
R3	R(1,6)	1.0939	1.0931
R4	R(1,7)	1.0989	1.0977
R5	R(2,3)	1.5436	1.5481
R6	R(2,8)	1.0953	1.0938
R7	R(2,9)	1.0939	1.0928
R8	R(3,4)	1.4978	1.5060
R9	R(3,10)	1.0961	1.0940
R10	R(3,11)	1.1054	1.1032
R11	R(4,5)	1.3775	1.3799
R12	R(4,12)	1.0853	1.0856
A1	A(2,1,5)	105.9675	106.0793
A2	A(2,1,6)	114.0962	113.7626
A3	A(2,1,7)	111.6547	111.5786
A4	A(5,1,6)	108.1730	108.1567
A5	A(5,1,7)	108.1765	108.0080
A6	A(6,1,7)	108.5451	109.0160
A7	A(1,2,3)	102.0391	102.0695
A8	A(1,2,8)	110.2344	110.2674
A9	A(1,2,9)	112.4973	112.2810
A10	A(3,2,8)	110.0921	110.0041
A11	A(3,2,9)	113.5664	113.3389
A12	A(8,2,9)	108.3130	108.7496
A13	A(2,3,4)	100.8611	100.8915
A14	A(2,3,10)	112.9188	112.9257
A15	A(2,3,11)	110.4521	110.4931
A16	A(4,3,10)	113.1622	112.9256
A17	A(4,3,11)	112.6669	112.0366
A18	A(10,3,11)	106.8498	107.5661
A19	A(3,4,5)	111.1154	110.9677
A20	A(3,4,12)	126.2475	126.1630
A21	A(5,4,12)	113.8633	114.1925
A22	A(1,5,4)	109.0032	109.1312

		Optimized Parameters (Å and °)	
Name	**Definition**	**6-31G(d)**	**EPR-II**
D1	D(5,1,2,3)	29.3682	28.7902
D2	D(5,1,2,8)	-87.5664	-88.0733
D3	D(5,1,2,9)	151.4280	150.4872
D4	D(6,1,2,3)	148.2721	147.5573
D5	D(6,1,2,8)	31.3374	30.6939
D6	D(6,1,2,9)	-89.6682	-90.7457
D7	D(7,1,2,3)	-88.1936	-88.5959
D8	D(7,1,2,8)	154.8718	154.5406
D9	D(7,1,2,9)	33.8662	33.1011
D10	D(2,1,5,4)	-14.6413	-13.8000
D11	D(6,1,5,4)	-137.3845	-136.2021
D12	D(7,1,5,4)	105.2214	105.9467
D13	D(1,2,3,4)	-31.7441	-31.5936
D14	D(1,2,3,10)	-152.8057	-152.3962
D15	D(1,2,3,11)	87.6197	87.0794
D16	D(8,2,3,4)	85.2931	85.4597
D17	D(8,2,3,10)	-35.7684	-35.3429
D18	D(8,2,3,11)	-155.3430	-155.8673
D19	D(9,2,3,4)	-153.0678	-152.5597
D20	D(9,2,3,10)	85.8707	86.6377
D21	D(9,2,3,11)	-33.7039	-33.8868
D22	D(2,3,4,5)	25.2541	25.6244
D23	D(2,3,4,12)	170.4266	171.0796
D24	D(10,3,4,5)	146.1431	146.4271
D25	D(10,3,4,12)	-68.6844	-68.1176
D26	D(11,3,4,5)	-92.5020	-91.9241
D27	D(11,3,4,12)	52.6705	53.5311
D28	D(3,4,5,1)	-7.1417	-7.9035
D29	D(12,4,5,1)	-156.9009	-157.7790

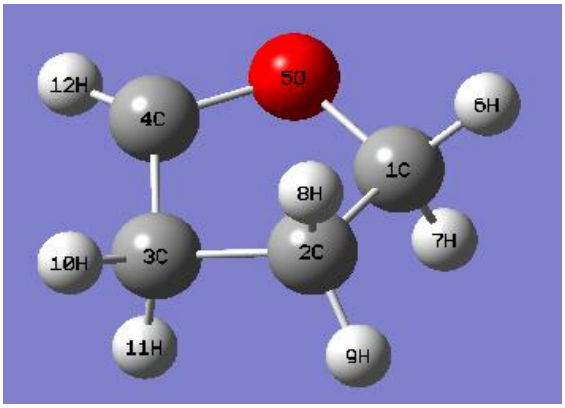

Figure C2. Optimized geometry of radical 2.

Internal coordinates of optimized geometries for radical 3

Scheme C3. Atom numbering

C1	H6	H7
C2	H8	H9
C3	H12	
C4	H10	H11 (Mu)
O5		

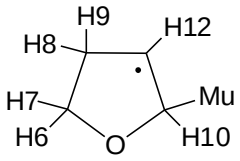

Table C3. Internal coordinates

		Optimized Parameters (Å and °)	
Name	**Definition**	**6-31G(d)**	**EPR-II**
R1	R(1,2)	1.5425	1.5465
R2	R(1,5)	1.4266	1.4318
R3	R(1,6)	1.1028	1.1014
R4	R(1,7)	1.0936	1.0928
R5	R(2,3)	1.4948	1.5035
R6	R(2,8)	1.0981	1.0964
R7	R(2,9)	1.1037	1.1013
R8	R(3,4)	1.4956	1.5033
R9	R(3,12)	1.0833	1.0835
R10	R(4,5)	1.4292	1.4337
R11	R(4,10)	1.1087	1.1066
R12	R(4,11)	1.1004	1.0984
A1	A(2,1,5)	105.6925	105.6432
A2	A(2,1,6)	110.1992	110.2228
A3	A(2,1,7)	114.2229	113.9350
A4	A(5,1,6)	110.5891	110.2968
A5	A(5,1,7)	107.5345	107.6325
A6	A(6,1,7)	108.5417	109.0183
A7	A(1,2,3)	100.8837	101.0001
A8	A(1,2,8)	112.7099	112.6437
A9	A(1,2,9)	110.8674	110.7104
A10	A(3,2,8)	113.8075	113.5698
A11	A(3,2,9)	111.8748	111.5177
A12	A(8,2,9)	106.7662	107.4024
A13	A(2,3,4)	109.0513	108.8237
A14	A(2,3,12)	126.0604	126.1471
A15	A(4,3,12)	124.8673	124.9803
A16	A(3,4,5)	105.3984	105.3211
A17	A(3,4,10)	111.9910	111.7769
A18	A(3,4,11)	114.2155	113.8598
A19	A(5,4,10)	110.6350	110.3192
A20	A(5,4,11)	107.7951	107.9975
A21	A(10,4,11)	106.7623	107.4997
A22	A(1,5,4)	107.5950	107.4628

		Optimized Parameters (Å and °)	
Name	**Definition**	**6-31G(d)**	**EPR-II**
D1	D(5,1,2,3)	-29.3837	-29.2509
D2	D(5,1,2,8)	-151.1244	-150.7484
D3	D(5,1,2,9)	89.2583	88.9757
D4	D(6,1,2,3)	90.1266	89.8956
D5	D(6,1,2,8)	-31.6141	-31.6019
D6	D(6,1,2,9)	-151.2314	-151.8778
D7	D(7,1,2,3)	-147.3891	-147.1846
D8	D(7,1,2,8)	90.8702	91.3179
D9	D(7,1,2,9)	-28.7471	-28.9580
D10	D(2,1,5,4)	35.1092	35.8118
D11	D(6,1,5,4)	-84.1436	-83.2856
D12	D(7,1,5,4)	157.5010	157.8901
D13	D(1,2,3,4)	14.0471	13.1663
D14	D(1,2,3,12)	-167.5575	-169.2850
D15	D(8,2,3,4)	135.0135	134.0105
D16	D(8,2,3,12)	-46.5911	-48.4407
D17	D(9,2,3,4)	-103.8620	-104.4723
D18	D(9,2,3,12)	74.5334	73.0764
D19	D(2,3,4,5)	5.8000	7.1298
D20	D(2,3,4,10)	-114.5607	-112.6827
D21	D(2,3,4,11)	123.9280	125.2598
D22	D(12,3,4,5)	-172.6190	-170.4544
D23	D(12,3,4,10)	67.0203	69.7330
D24	D(12,3,4,11)	-54.4910	-52.3244
D25	D(3,4,5,1)	-25.4733	-26.6956
D26	D(10,4,5,1)	95.7747	94.0772
D27	D(11,4,5,1)	-147.8322	-148.7002

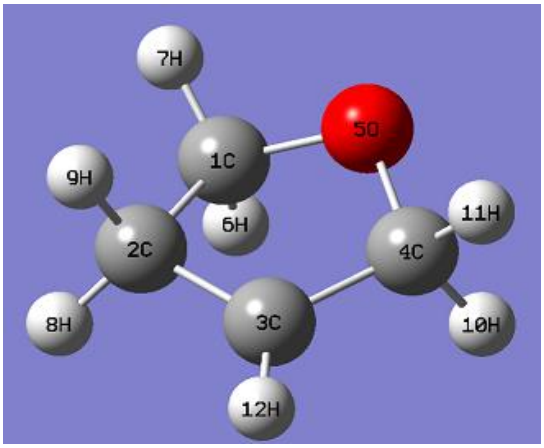

Figure C3. Optimized geometry of radical 3.

Internal coordinates of optimized geometries for radical 4

Scheme C4. Atom numbering

C1	H6	
C2	H7	
C3	H8	H10 (Mu)
C4	H9	
O5		

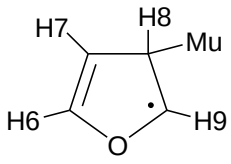

Table C4. Internal coordinates

		Optimized Parameters (Å and °)	
Name	**Definition**	**6-31G(d)**	**EPR-II**
R1	R(1,2)	1.3351	1.3445
R2	R(1,5)	1.3790	1.3809
R3	R(1,6)	1.0817	1.0821
R4	R(2,3)	1.5138	1.5203
R5	R(2,7)	1.0816	1.0814
R6	R(3,4)	1.5019	1.5103
R7	R(3,8)	1.1038	1.1003
R8	R(3,10)	1.1070	1.1041
R9	R(4,5)	1.3856	1.3890
R10	R(4,9)	1.0823	1.0831
A1	A(2,1,5)	113.7019	113.6254
A2	A(2,1,6)	131.8107	131.4487
A3	A(5,1,6)	114.4874	114.9257
A4	A(1,2,3)	108.4004	108.2921
A5	A(1,2,7)	126.0736	125.8232
A6	A(3,2,7)	125.5251	125.8830
A7	A(2,3,4)	100.3506	100.3345
A8	A(2,3,8)	112.8065	112.6545
A9	A(2,3,10)	112.3964	112.1815
A10	A(4,3,8)	112.8724	112.6224
A11	A(4,3,10)	113.2847	112.8689
A12	A(8,3,10)	105.3850	106.3325
A13	A(3,4,5)	110.5131	110.4009
A14	A(3,4,9)	128.0419	127.9467
A15	A(5,4,9)	114.2330	114.4363
A16	A(1,5,4)	106.6291	106.9029
D1	D(5,1,2,3)	0.2466	0.3647
D2	D(5,1,2,7)	179.9222	179.9052
D3	D(6,1,2,3)	-179.8489	-179.8140
D4	D(6,1,2,7)	-0.1733	-0.2734
D5	D(2,1,5,4)	3.8197	3.9235
D6	D(6,1,5,4)	-176.1021	-175.9289
D7	D(1,2,3,4)	-3.7928	-4.0419
D8	D(1,2,3,8)	-124.1521	-124.0286

		Optimized Parameters (Å and °)	
Name	**Definition**	**6-31G(d)**	**EPR-II**
D9	D(1,2,3,10)	116.8636	116.0212
D10	D(7,2,3,4)	176.5293	176.4179
D11	D(7,2,3,8)	56.1700	56.4312
D12	D(7,2,3,10)	-62.8143	-63.5190
D13	D(2,3,4,5)	6.1723	6.4818
D14	D(2,3,4,9)	154.2973	154.6618
D15	D(8,3,4,5)	126.4842	126.4917
D16	D(8,3,4,9)	-85.3908	-85.3283
D17	D(10,3,4,5)	-113.8448	-113.0838
D18	D(10,3,4,9)	34.2802	35.0962
D19	D(3,4,5,1)	-6.3352	-6.6101
D20	D(9,4,5,1)	-159.2012	-159.4362

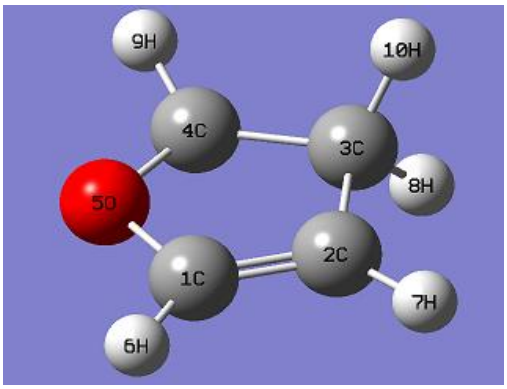

Figure C4. Optimized geometry of radical 4.

Internal coordinates of optimized geometries for radical 5

Scheme C5. Atom numbering

C1	H6	
C2	H7	
C3	H8	
C4	H9	H10 (Mu)
O5		

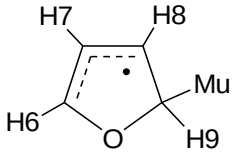

Table C5. Internal coordinates

		Optimized Parameters (Å and °)	
Name	**Definition**	**6-31G(d)**	**EPR-II**
R1	R(1,2)	1.3854	1.3954
R2	R(1,5)	1.3658	1.3680
R3	R(1,6)	1.0805	1.0812
R4	R(2,3)	1.3881	1.3967
R5	R(2,7)	1.0827	1.0826
R6	R(3,4)	1.4998	1.5071
R7	R(3,8)	1.0815	1.0815
R8	R(4,5)	1.4506	1.4540
R9	R(4,9)	1.1022	1.1003
R10	R(4,10)	1.1022	1.1003
A1	A(2,1,5)	112.3307	112.2387
A2	A(2,1,6)	131.9891	131.7258
A3	A(5,1,6)	115.6802	116.0355
A4	A(1,2,3)	108.1692	108.0791
A5	A(1,2,7)	124.9118	124.9030
A6	A(3,2,7)	126.9190	127.0179
A7	A(2,3,4)	107.3316	107.1923
A8	A(2,3,8)	128.0597	128.0957
A9	A(4,3,8)	124.6087	124.7120
A10	A(3,4,5)	104.8061	104.8734
A11	A(3,4,9)	114.3687	113.9385
A12	A(3,4,10)	114.3715	113.9454
A13	A(5,4,9)	107.8776	107.8724
A14	A(5,4,10)	107.8776	107.8704
A15	A(9,4,10)	107.1879	107.9919
A16	A(1,5,4)	107.3623	107.6164
D1	D(5,1,2,3)	-0.0091	0.0126
D2	D(5,1,2,7)	179.9978	180.0103
D3	D(6,1,2,3)	-179.9888	-179.9665
D4	D(6,1,2,7)	0.0181	0.0313
D5	D(2,1,5,4)	0.0081	-0.0025
D6	D(6,1,5,4)	180.0087	179.9801
D7	D(1,2,3,4)	0.0061	-0.0168
D8	D(1,2,3,8)	-179.9857	180.0118

		Optimized Parameters (Å and °)	
Name	**Definition**	**6-31G(d)**	**EPR-II**
D9	D(7,2,3,4)	179.9991	-180.0145
D10	D(7,2,3,8)	0.0073	0.0141
D11	D(2,3,4,5)	-0.0014	0.0151
D12	D(2,3,4,9)	-117.9262	-117.7161
D13	D(2,3,4,10)	117.9249	117.7476
D14	D(8,3,4,5)	-180.0093	-180.0122
D15	D(8,3,4,9)	62.0659	62.2565
D16	D(8,3,4,10)	-62.0830	-62.2797
D17	D(3,4,5,1)	-0.0039	-0.0077
D18	D(9,4,5,1)	122.2513	121.7783
D19	D(10,4,5,1)	-122.2624	-121.8007

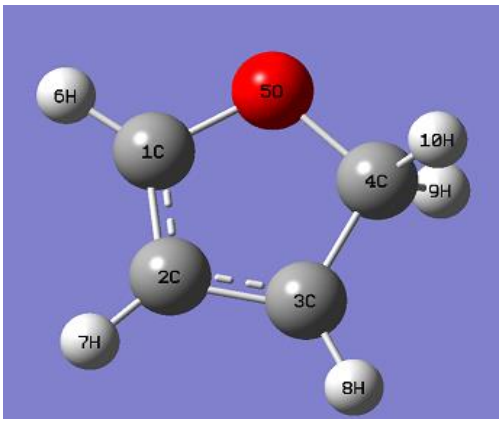

Figure C5. Optimized geometry of radical 5.

Hyperfine constants calculated using the EPR-II basis set

Table C6. computed[a] hyperfine constants for radicals **2** and **3** Compared with those determined by μ-LCR spectroscopy on liquid and clathrate hydrate samples of 2,3-dihydrofuran at −10°C

Nucleus	***A*(Mu-ax)**	***A*(Mu-eq)**	$A_{calc.}$[b]	A_{exp}**(liq)**	A_{exp}**(hydr.)**
radical **2**					
muon	405.4	167.1	314.6	(299.9)[c]	301.5
β-C**H**Mu	49.1	114.2	73.9	74.9	72.5
α-C**H**	-32.4	-33.2	-32.7	-36.7	-36.4[a]
radical **3**					
muon	409.7	337.5	381.6	(371.2)[c]	374.1
β-C**H**Mu	93.1	114.2	101.3	101.8	101.9
α-C**H**	-50.1	-49.6	-49.9	-58.8	-60.1[a]
β-**H** axial	126.0	66.9	103.0	97.8	96.0
β-**H** equatorial	70.0	127.2	92.3	93.8	91.1

[a] UBLYP/EPR-II. [b] Weighted average of two conformations. [c] Value obtained by TF-μSR.

Table C7. computed[a] hyperfine constants for radicals 4 and 5 compared with those determined by μ-LCR spectroscopy on a clathrate hydrate sample of furan at −13°C

Nucleus	***A*(Mu-ax)**	***A*(Mu-eq)**	$A_{calc.}$[b]	A_{exp}**(liq)**[c]	A_{exp}**(hydr.)**[d]
radical **4**					
muon	549.7	505.9	531.4	(497) [e]	500.1
β-C**H**Mu	139.7	150.9	144.3	130	129.5
α-C**H**	-45.5	-47.9	-46.5		-40.8
radical **5**					
muon	–	–	411.5	(378.8) [e]	382.2
β-C**H**Mu	–	–	109.2	100.2	100.1
C(3)**H**	–	–	10.0		14.3
C(2)**H**	–	–	-37.9	-37.2	-37.7
C(4)**H**	–	–	-36.5	-36.4	-36.6

[a] UBLYP/EPR-II. [b] Weighted average of two conformations. [c] Ref.[148], 25°C. [d] This work. [e] Value obtained by TF-μSR.

Gaussian 09

Gaussian 09, Revisions C.01, D.01, E.01, Frisch, M. J.; Trucks, G. W.; Schlegel, H. B.; Scuseria, G. E.; Robb, M. A.; Cheeseman, J. R.; Scalmani, G.; Barone, V.; Mennucci, B.; Petersson, G. A.; Nakatsuji, H.; Caricato, M.; Li, X.; Hratchian, H. P.; Izmaylov, A. F.; Bloino, J.; Zheng, G.; Sonnenberg, J. L.; Hada, M.; Ehara, M.; Toyota, K.; Fukuda, R.; Hasegawa, J.; Ishida, M.; Nakajima, T.; Honda, Y.; Kitao, O.; Nakai, H.; Vreven, T.; Montgomery, J. A., Jr.; Peralta, J. E.; Ogliaro, F.; Bearpark, M.; Heyd, J. J.; Brothers, E.; Kudin, K. N.; Staroverov, V. N.; Kobayashi, R.; Normand, J.; Raghavachari, K.; Rendell, A.; Burant, J. C.; Iyengar, S. S.; Tomasi, J.; Cossi, M.; Rega, N.; Millam, N. J.; Klene, M.; Knox, J. E.; Cross, J. B.; Bakken, V.; Adamo, C.; Jaramillo, J.; Gomperts, R.; Stratmann, R. E.; Yazyev, O.; Austin, A. J.; Cammi, R.; Pomelli, C.; Ochterski, J. W.; Martin, R. L.; Morokuma, K.; Zakrzewski, V. G.; Voth, G. A.; Salvador, P.; Dannenberg, J. J.; Dapprich, S.; Daniels, A. D.; Farkas, Ö.; Foresman, J. B.; Ortiz, J. V.; Cioslowski, J.; Fox, D. J. Gaussian, Inc., Wallingford CT, 2013-2016.